

Washington University in St. Louis

Washington University Open Scholarship

Arts & Sciences Electronic Theses and
Dissertations

Arts & Sciences

12-2023

Thermodynamics and Kinetics Analyses of CLC-ec1 Dimerization Reaction in Lipid Bilayers

Taeho Lee

Washington University in St. Louis

Follow this and additional works at: https://openscholarship.wustl.edu/art_sci_etds



Part of the [Biophysics Commons](#)

Recommended Citation

Lee, Taeho, "Thermodynamics and Kinetics Analyses of CLC-ec1 Dimerization Reaction in Lipid Bilayers" (2023). *Arts & Sciences Electronic Theses and Dissertations*. 3110.

https://openscholarship.wustl.edu/art_sci_etds/3110

This Dissertation is brought to you for free and open access by the Arts & Sciences at Washington University Open Scholarship. It has been accepted for inclusion in Arts & Sciences Electronic Theses and Dissertations by an authorized administrator of Washington University Open Scholarship. For more information, please contact digital@wumail.wustl.edu.

WASHINGTON UNIVERSITY IN ST. LOUIS
DEPARTMENT OF PHYSICS

Dissertation Examination Committee:
Anders E. Carlsson, Chair
Baron Chanda
Shankar Mukherji
Janice L. Robertson
Ralf Wessel

Thermodynamics and Kinetics Analyses of CLC-ec1 Dimerization Reaction in Lipid Bilayers
by
Taeho Lee

A dissertation presented to
Washington University in St. Louis
in partial fulfillment of the
requirements for the degree
of Doctor of Philosophy

December 2023
St. Louis, Missouri

© 2023, Taeho Lee

Table of Contents

List of Figures	vii
List of Tables	ix
Acknowledgments	x
Abstract	xiii
<u>1. Introduction</u>	1
1.1 Preface to the Chapter	1
1.2 Background Literature on the Study of Membrane Protein Stability in Membranes	2
1.3 Overview of Techniques to Study Thermodynamic Stability of Membrane Proteins in Membranes	3
1.4 The CLC Family of Membrane Proteins as Model Systems for Studying in Membrane Binding Thermodynamics	6
1.4.1 The CLC Superfamily	6
1.4.2 Functional and Structural Characteristics of CLC-ec1	8
1.5 Measurements of CLC-ec1 Dimerization Equilibrium in Membranes	12
1.6 van 't Hoff Analysis for Dissecting Thermodynamic Changes in Protein Stability Equilibrium	15
1.7 Subunit-Exchange Kinetics to Measure Kinetics of Binding Complexes	17
1.8 Summary	19
1.9 Description of Thesis Content	20
References	23
<u>2. Materials and Methods</u>	27
2.1 Preface to the Chapter	27
2.2 Buffers	27
2.3 Protein Purification	27
2.4 Site Specific Labeling of CLC-ec1 using Cy3-Maleimide and Cy5-Maleimide.....	29
2.5 Lipid Preparation	31

2.6 Reconstitution of CLC-ec1 into Liposome	32
2.7 Bulk FRET Method of CLC-ec1 Subunit-Exchange	32
2.8 Subunit Capture Single Molecule Photobleaching Measurement of CLC-ec1	33
2.9 Calculation of F_{Dimer} and ΔG°	34
2.10 Measurement of CLC-ec1 Function	36
2.11 Preparing CLC-ec1 and Lipid Bilayer for Coarse-Grained Molecular Dynamics Simulations	37
References	40

3. The Lambda III, Total Internal Reflection Fluorescent (TIRF) Microscope Alignment

<u>Tutorial</u>	42
3.1 Preface to the Chapter	42
3.2 Abstract	43
3.3 Introduction	43
3.4 Procedure	45
3.4.1 Alignment of the excitation pathway	45
3.4.2 Alignment of the excitation beam onto a platform	46
3.4.3 Alignment of the excitation micromirror	49
3.4.4 Adjusting the exiting micromirrors	53
3.4.5 Positioning of L_1 & L_2 lenses in emission path	57
3.4.6 Alignment for emission path	59
3.4.7 Alignment for multi-color imaging	62
3.4.8 Adjustment of the laser power	65
3.4.9 Micrometer slide ruler for scale bar	65
References	68

4. A Thermodynamic Analysis of CLC Transporter Dimerization in Lipid Bilayers 69 |

4.1 Preface to the Chapter	69
4.2 Abstract	69
4.3 Introduction	70
4.4 Materials and Methods	75

4.4.1 Protein purification	75
4.4.2 Preparation of lipids	75
4.4.3 Protein labeling and reconstitution	76
4.4.4 Bulk FRET measurement in PLVs	78
4.4.5 Single-molecule subunit capture photobleaching analysis	80
4.4.6 K_{eq} and van 't Hoff parameter estimation	81
4.4.7 Functional measurements	82
4.5 Results	83
4.5.1 CLC-ec1 dimers exhibit dynamic subunit exchange in lipid bilayers	83
4.5.2 CLC-ec1 undergoes subunit-exchange across many temperatures while remaining functionally folded	87
4.5.3 The temperature dependency of CLC-ec1 dimerization equilibrium in EPL membranes	92
4.5.4 CLC-ec1 dimerization exhibits a non-linear temperature dependency in 2:1 POPE/POPG	95
4.6 Discussion	99
4.6.1 CLC dimerization is in a dynamic equilibrium in lipid membranes	99
4.6.2 Dimerization of CLC involves the observation of a large change in heat capacity ..	101
4.7 Conclusion	107
4.8 Acknowledgments	108
References	109
<u>S4. Supporting Information</u>	112
S4.1 Appendix	112
S4.1.1 Quantification of protein/fluorophore labeling yields	112
S4.1.2 Differential Scanning Calorimetry (DSC)	114
S4.1.3 Bulk FRET measurements in PLVs – membrane fusion	114
S4.1.4 Small angle x-ray scattering (SAXS)	114
S4.1.5 Calculation of waters in the membrane	117
SI References	129

<u>5. The Calculation of Cavity Volume in the Coarse-grained MD Simulation Depending on Solvent Volume</u>	130
5.1 Preface to the Chapter	130
5.2 Abstract	130
5.3 Introduction	131
5.4 Materials and Methods	135
5.4.1 Building the coarse-grained structural model of CLC-ec1 protomer	135
5.4.2 Equilibration of the POPC bilayer on a coarse-grained system	135
5.4.3 Applying restraints for the coarse-grained CLC-ec1-membrane simulation systems	136
5.4.4 Analysis of dynamic behavior of solvent exchange	137
5.4.5 Angle analysis between subunits with different restraints	137
5.4.6 Analysis of solvent inaccessible cavity volume between the dimerization interface	137
5.5 Results	138
5.5.1 Positional analysis of CLC-ec1 subunit during the simulation	140
5.5.2 Evidence of dynamic lipid exchange between CLC subunits	144
5.5.3 Density analysis of CLC-ec1 subunit in mixed lipid bilayers containing small molecules	147
5.5.4 Analysis of subunit exchange kinetics on the CLC-ec1 with small molecule β -OG using bulk FRET measurement	150
5.6 Discussion	152
5.7 Conclusion	153
References	154
<u>6. Connecting CLC-ec1 Dimerization with Functional Activity</u>	156
6.1 Preface to the Chapter	156
6.2 Abstract	156
6.3 Introduction	157
6.4 Materials and Methods	161
6.4.1 Protein purification	161

6.4.2 Preparation of lipids	162
6.4.3 Protein labeling and reconstitution	162
6.4.4 pH titrations	166
6.4.5 Bulk-FRET measurements in pauci-lamellar vesicles	167
6.4.6 Single-molecule subunit capture photobleaching experiment	168
6.5 Results	169
6.5.1 CLC-ec1 dimerization is linked to pH	169
6.5.2 CLC-ec1 dimerization is independent of channel-like activity	171
6.6 Discussion	175
6.7 Conclusion	176
References	177
<u>7. Impact of this Work on Understanding Membrane Protein Folding in Membranes and Future Directions for the Field</u>	179
7.1 Broad Impact of Dynamic CLC-ec1 Dimerization in Membranes	179
7.2 Thermodynamic Dissection of CLC-ec1 Dimerization in Membranes Uncovers a Generalizable Driving Force for Assembly in Membranes	180
7.3 Dependency of CLC-ec1 Dimer Stability on Lipid Composition	182
7.4 Implications and Possible Mechanisms of Slow Kinetics of CLC-ec1 Assembly in Membranes	183
7.5 Functional Consequences of CLC-ec1 Dimerization	185
7.6 Future Directions for the Study of Membrane Protein Assembly Thermodynamics and Kinetics in Membranes	186
References	188

List of Figures

Chapter 1

Figure 1 Various techniques to study thermodynamic stability of membrane proteins	5
Figure 2 Structure characteristics of the CLC-ec1 homodimer	11
Figure 3 Structure for the CLC-ec1 function	12
Figure 4 Subunit capture single molecule photobleaching method to measure the thermodynamic stability of CLC-ec1	14

Chapter 3

Figure 1 Schematic view of the optical setup for excitation path of micromirror TIRF microscope	48
Figure 2 Schematic view of an excitation micro-mirror positioner	52
Figure 3 Schematic view of objective lens site	56
Figure 4 Schematic view of the optical setup for emission path of mmTIRF microscope	58
Figure 5 Schematic view for the initial alignment of the emission path	61
Figure 6 Images created on the CCD	64
Figure 7 Micrometer slide ruler for scale bar	67

Chapter 4

Figure 1 Dynamic exchange CLC-ec1 subunits in membranes observed by bulk FRET.....	84
Figure 2 Temperature dependency and reversibility of CLC-ec1 subunit exchange in membranes	90
Figure 3 Temperature dependency of CLC-ec1 dimerization equilibrium in EPL membranes	93
Figure 4 Temperature dependency of CLC-ec1 dimerization in 2:1 POPE/POPG lipid bilayers	97
Figure S1 Membrane properties of EPL and 2:1 POPE/POPG PLVs	119
Figure S2 Two-component FRET kinetics in CLC subunit-exchange	120
Figure S3 CLC-ec1 chloride transport after incubation at different temperatures	121

Figure S4 Lack of evidence of CLC-ec1 dimerization equilibration in EPL at temperatures below room temperature	122
Figure S5 Analysis of temperature dependency van 't Hoff data	123
Figure S6 The number of water molecules associated with the membrane in the monomeric state of CLC-ec1	124

Chapter 5

Figure 1 Hypothetical energy landscape of CLC-ec1 dimerization	134
Figure 2 Martini topologies used for coarse-grained MD simulation	139
Figure 3 Angle analysis between subunits in different simulations	141
Figure 4 Box definition between the dimerization interface	143
Figure 5 Analysis of dynamic behavior of solvent exchange in CAHC 100% POPC, 10% PPC & 90% POPC, 10% benzene & 90% POPC in 16 Å separation system	146
Figure 6 Number of beads between the dimerization interface	148
Figure 7 Density between the dimerization interface	149
Figure 8 Subunit exchange FRET experiment with titration of β -OG	151

Chapter 6

Figure 1 Hypothetical cartoon of dimerization reaction	160
Figure 2 CLC dimerization is strongly linked to environmental pH	171
Figure 3 A stability of channel version of CLC-ec1 is independent of activating condition	174

List of Tables

Chapter 3

Table 1 Summary of the beam movement based on the alignment on the excitation micro-mirror	53
---	----

Chapter 4

Table S1 Structural properties of lipid bilayers measured by SAXS	125
Table S2 Observed K_D , K_{eq} and ΔG° values for temperature dependent CLC-ec1 dimerization equilibrium in lipid bilayers	126
Table S3 Thermodynamic parameters from non-linear and linear van 't Hoff fits	127
Table S4 Analysis of number and distribution of coarse-grained water beads in the membrane defect around the CLC-ec1 dimerization interface relative to the bulk lipid bilayer ..	128

Acknowledgments

I thank my wife Min Kyung for her unwavering love, endless support, warm encouragement, advice, and sacrifice through my Ph.D. journey and dissertation writing. As someone who has already gone through the Ph.D. program with a similar background, her advice and encouragement meant a lot to me when I faced challenges during graduate school. Without her love and support, I would not have made this far. I thank my parents and my brother in Korea for their infinite love, sacrifice, endless support, and encouragement so that I can pursue a Ph.D. degree in a different country. I also want to thank my in-laws for their kindness, support, and amazing Korean food every time I visit them. The love and support that I received from all of my family have truly been a tremendous source of strength and confidence in me.

I would also like to extend my gratitude to former Robertson lab members who have answered all my questions and who filled the gaps in my knowledge in biophysics and biochemistry. Specifically, I thank Dr. Rahul Chadda for his help and invaluable advice. I also learned efficient and creative ways of performing experiments and analyses from him. I thank Dr. Kacey Mersch for his advice and fruitful discussions on experiments, papers, and analysis methods. I thank Dr. Tugba Ozturk for teaching me how to perform MD simulations and engaging in scientific discussions and daily conversations with me.

I would also like to thank my current labmates Robyn Mahoney-Kruszka for teaching me various experiment techniques and always perfectly taking care of everything around the lab and having conversations about baseball with me. I thank Melanie Ernst for engaging in scientific discussions and casual everyday conversations about our graduate school life. I also thank Nathan Zelt for offering me delicious homemade salsa and tacos, and for being a good friend. I thank Dr.

Gladys Díaz Vázquez for fruitful scientific discussions about experiments and MD simulations. The coffee times that I had with my labmates in the mornings have been the great moments in my graduate school life. I cherish the friendships that I have built with my labmates.

I would like to thank the Department of Physics for giving me an opportunity to conduct interdisciplinary research across the department, and I especially want to thank Sarah Akin who gave warm support during my Ph.D. and answered a ton of questions I have had. I would also like to thank the Department of Biochemistry and Molecular Biophysics at the Washington University School of Medicine for having me and for including me in the departmental activities.

Lastly, I want to express my gratitude towards my thesis advisor, Professor Janice Robertson, for her guidance and unlimited support during my Ph.D. studies. I sincerely want to thank her for giving me an opportunity to conduct research in her lab. Even though I came with a different background than biophysics, she was always open-minded and willing to teach me anything I would like to learn. Her warm support and her confidence in me have been a great encouragement in my academic growth as an independent and logical thinker and a great communicator. Janice truly represents the model of an exceptional mentor. She is my role model, whom I aspire to resemble not only as a scientist but also as a person.

Taeho Lee

Washington University in St. Louis

December 2023

Dedicated to my family

ABSTRACT OF THE DISSERTATION

Thermodynamics and Kinetics Analyses of CLC-ec1 Dimerization in Lipid Bilayers

by

Taeho Lee

Doctor of Philosophy in Physics

Washington University in St. Louis, 2023

Professor Janice L. Robertson, Dissertation Advisor

Professor Anders E. Carlsson, Chair

The efforts of this thesis are directed towards understanding the thermodynamics and kinetics underlying the dimerization reaction of a chloride/proton antiporter membrane protein, CLC-ec1, in lipid membranes. Due to the inherent challenges of working with membrane proteins, thermodynamic and kinetic information for the protein association reactions in membranes has been historically limited. The research presented in this thesis demonstrates the technological advancements for these measurements in a model membrane protein system, thereby setting an important milestone for the field. Since CLC-ec1 dimerizes via a greasy, membrane embedded binding interface, the physical driving forces involved in this reaction were unknown. It further presents a thermodynamic dissection of CLC-ec1 dimerization in lipid bilayers by carrying out a temperature-dependent van 't Hoff analysis using the single-molecule photobleaching subunit-capture approach. This revealed a large negative change in the heat capacity, ΔC_P , in CLC-ec1 dimerization, representing the same thermodynamic signature as the hydrophobic effect. This investigation also led to the development of a method for measuring protein subunit-exchange in membranes by bulk Förster resonance energy transfer (FRET), showing slow dissociation kinetics at ambient temperatures. We found that the subunit-exchange speeds up with temperature,

following an Arrhenius relationship and suggesting that there is a high transition state energy barrier to dissociation. This work led to the hypothesis that the energy barrier is formed by states along the dissociation pathway where the subunits separate but are incompletely solvated, introducing cavity volumes. To investigate this hypothesis, coarse grained molecular dynamics simulations were set up for CLC-ec1 subunits of different separations using MARTINI force field to characterize cavity formation. The simulations were repeated with mixed lipid bilayers containing smaller molecules, such as lysolipids and benzene to see if these solvents can reduce the cavity volumes, with results showing that smaller size molecules at higher concentrations increase the overall packing density in the cavity between the CLC-ec1 subunits. Finally, since it is unclear as to the reason why CLC-ec1 evolved as a stable homodimer, an investigation was carried out into whether the dimerization reaction was linked to transport mechanism. Subunit-exchange experiments were carried out as a function of pH, a known environmental regulator of CLC-ec1 transport function, showing that at $\text{pH} > 6.5$, dissociation no longer occurs corresponding to conditions where CLC-ec1 transport function is reduced. In addition, the connection between transport mechanism and dimerization was examined by studying a channelized version of CLC-ec1 with binding site mutations E148A/Y445S. Our findings demonstrate that CLC dimerization is strongly linked to pH, but the dimerization is not closely linked to the transport mechanism. Altogether, the results of this research present an in-depth thermodynamic analysis of membrane protein dimerization in membranes and establish a foundation for future studies to understand membrane protein complex stability, kinetics, and regulation.

Chapter 1 of this thesis presents an overview of previous research on CLC-ec1 as well as the study of membrane protein association equilibrium in membranes.

Chapter 2 describes the main methodologies applied or developed in this thesis research, including the single-molecule photobleaching subunit capture approach, bulk FRET measurements, and chloride transport efflux assays.

Chapter 3 presents a tutorial protocol of the *Lambda III* single-molecule total internal reflection fluorescence (TIRF) microscope, a pivotal piece of equipment used in investigating the thermodynamic stability of CLC-ec1 in membranes. It provides a step-by-step guide on alignment of the microscope, starting from the excitation pathway, emission pathway, and finally the alignment of the micromirrors for total internal reflection. The protocol also describes the basic physical principles of this TIRF microscope.

Chapter 4 describes the thermodynamic dissection of CLC-ec1 dimerization equilibrium in lipid bilayers by performing a temperature dependent van 't Hoff of the free energy of CLC-ec1 dimerization in two different lipid compositions. In addition, it presents a new methodology for measuring dynamic subunit-exchange in membranes by bulk FRET, revealing the remarkably slow kinetic behavior of this dynamic equilibrium reaction at ambient temperatures.

Chapter 5 presents a computational modeling investigation of potential dissociation states of CLC-ec1 and whether there are cavities formed that are inaccessible to phospholipid solvent molecules between the CLC-ec1 subunits. The analysis then extends to the study of mixed membranes containing lysolipids and benzene to investigate whether these small molecules increase lipid solvation to provide rationale for lipid dependency of subunit dissociation kinetics. This analysis serves as the initial steps towards identifying a relationship between lipid solvation and the dimerization kinetics.

Chapter 6 reports on an investigation into whether dimerization is linked to the regulation of functional mechanisms of CLC-ec1. To test this, we investigate the dimerization of wild type

(WT) CLC-ec1 at different pH, which is known to regulate transport function, and examine the thermodynamic and kinetic stability of transporter vs. channelized versions of the protein.

Finally, Chapter 7 provides a discussion of the impact of this research on understanding the kinetics and thermodynamics of membrane protein oligomerization in general with a focus on future directions that will expand on this foundational research.

Chapter 1: Introduction

1.1 Preface to the Chapter

Membrane proteins account for 25% of protein genes in *Escherichia coli*. This shows that membrane proteins play a significant role in physiology, including transducing external information such as ligands, ion gradients, and physical stimuli into energy for cells to carry out biological works. To carry out these tasks, they must fold and self-assemble in cell membranes. Therefore, understanding both the “intramolecular” driving forces that direct membrane protein folding and the “intermolecular” driving forces that make membrane proteins assemble as higher order complexes in cell membranes is crucial to discover unknown mechanisms related to biological diseases. However, progress in research on membrane proteins has been slow since handling membrane proteins can be laborious, and lipid bilayers are hard to control. A lack of fundamental understanding of membrane protein systems on how membrane proteins fold and mediate membrane protein self-assembly in membrane led to challenges in describing the thermodynamic parameters of driving forces that influence the free energy of protein dimerization in actual lipid bilayer, and how they assemble and disassemble. There have been advances in the field of membrane proteins over the past 20 years such as a development in Cryogenic Electron Microscopy (Cryo-EM). This allowed for the determination of biomolecular structures at near-atomic resolution, and many breakthroughs have been discovered to pave the way for understanding the thermodynamic free energy of the assembled state of proteins in membranes. To narrow the gap of knowledge in membrane protein dimerization, the works within this thesis try to answer the following questions: 1. Why do hydrophobic membrane proteins in the membrane,

form stable complexes with other hydrophobic proteins instead of interacting with the similarly hydrophobic solvent? 2. Why do membrane proteins exhibit slower dimerization kinetics? 3. Does the dimerization present a mechanism for regulating the functional behavior of each subunit?

1.2 Background on the Study of Membrane Protein Stability

Understanding membrane protein folding and stability in terms of thermodynamics is important because it helps us understand the physical mechanisms that biology needs to go through. Jacobs et al. (1) first suggested a three-step protein folding thermodynamic model (interfacial partitioning, interfacial folding, and insertion) with the structural and thermodynamic measurements about the partitioning of small hydrophobic peptides. Their results were supported by the following theoretical research from Milik et al. (2) revealing that the bilayer interface offers hydrophobic peptides folding and a free energy well for initial binding. Around that time, Popot & Engelman (3, 4) suggested a two-stage model. The model they suggested is about the assembly of α -helical proteins across the membrane, and then the functional structure is assembled at the final stage. The idea for this model originated from a set of experiments that demonstrated how individual segments of bacteriorhodopsin in lipid bilayers can naturally come together to reassemble into a fully functional structure (4). With all of these combined, White et al. (5) suggested four steps: partitioning, folding, insertion, and association of α -helix to determine the free energies (ΔG) every step along the pathway. Calculation of the free energy (ΔG) at each stage of the process allowed the computation of thermodynamic stabilities.

With this background, researchers have been able to analyze the intrinsic interactions involved by comprehensive investigations of the dimerization process of the single-helix TM protein glycoporphin A (GpA). Fleming et al. (6) carried out analytical ultracentrifugation studies

to investigate the energetics of GpA dimerization in detergent micelles. The research found that the mutation of Leucine at 75 to Alanine, and Isoleucine at 76 to Alanine destabilized the dimer stability of GpA in pentaerythritol octyl ether (C₈E₅) detergent micelle conditions by 1.1 kcal mol⁻¹ and 1.7 kcal mol⁻¹ respectively (6). After that, MacKenzie et al. (7) developed a way to analyze and predict the energetics of GpA dimerization. They used structure-based empirical parameters including steric clashes, favorable van der Waals interactions, and side-chain rotamer freedom restriction to explain the dimerization from the 105 hydrophobic single-point mutations on the GpA (7). These studies set an important foundation in the field that thermodynamic analyses of membrane protein association reactions were possible in membrane mimetic environments.

1.3 Overview of Techniques to Study Thermodynamic Stability of Membrane Proteins in Membranes

Since this work, researchers have worked hard to characterize of thermodynamic stability of membrane proteins in membranes also. In this section, I introduce several of the major techniques used to study the stability of membrane proteins in lipid bilayer environments. The first method is referred to as the “steric trapping” method (**Fig. 1A**). Steric trapping is a useful tool to study membrane protein folding and the thermodynamic stability under native conditions. The approach involves the simultaneous unfolding of a specific protein, which is marked with two biotin tags, and this is linked to the binding of large monovalent streptavidin molecules. Thermodynamic stability of intramembrane protease GlpG of *E. coli* has been revealed by this method (8). Steric trapping method was also used to reveal dissociation constants (K_D) of transmembrane helix dimers by modifying the binding affinity of mSA from mutation (9). The second method introduced is the “magnetic tweezer” method, that has been applied in bicelles or liposomes (**Fig. 1B**). Choi et al. (10) applied this technique to illustrate the energy landscape and

the thermodynamic stability by investigating the second stage folding of the single membrane protein *E. coli* rhomboid protease GlpG. In the magnetic tweezer method, the force on the membrane protein is applied perpendicular to the membrane surface (**Fig. 1B**) using single-molecule force microscopy. They determined energy landscape in one dimension to describe the reversible folding-unfolding of individual GlpG proteins, using Bell (11) and Dudko-Hummer-Szabo models (12). Both models calculated a free-energy gap (ΔG_0) of $15.2 k_B T$ between the native (N) state and unfolded zigzag (U_z) state. This technique made it possible to study thermodynamic stability of membrane proteins by mapping out the free energy landscape of the folding. Lastly, Förster resonance energy transfer (FRET) (**Fig. 1C**) was used to estimate the thermodynamic parameters for the formation of dimer complexes in the lipid environment using transmembrane helix NBD-(AALALAA)₃-NH₂ (**I**) and Ac-(AALALAA)₃-NHCH₂CH₂-S-DABMI (**II**) by Yano et al. (13). (**I**) and (**II**) are used as FRET donor and FRET acceptor respectively. FRET efficiency was measured by the NBD (donor) fluorescence quenching, and the dimer fraction is calculated to estimate the free energy. With the FRET data, they calculated the association free energy (ΔG_a) of monomer-antiparallel dimer equilibrium in PC membrane (diC (X:1) PC) with different lipid chain lengths ($X = 14-22$) across a wide range of temperatures, 5-55 °C, allowing for further thermodynamic decomposition. Finally, the subunit capture method approach using total internal reflection fluorescence (TIRF) microscope provides an alternate method of studying thermodynamics of oligomeric stability of membrane proteins in membranes. This approach has been widely used to study the thermodynamics associated with CLC-ec1 dimerization in various lipid bilayers, and has also been applied to an inverted topology ion channel dimer, Fluc (14-16) (**Fig. 1D**). The detailed technique about the subunit capture method is explained later in Chapter 2.

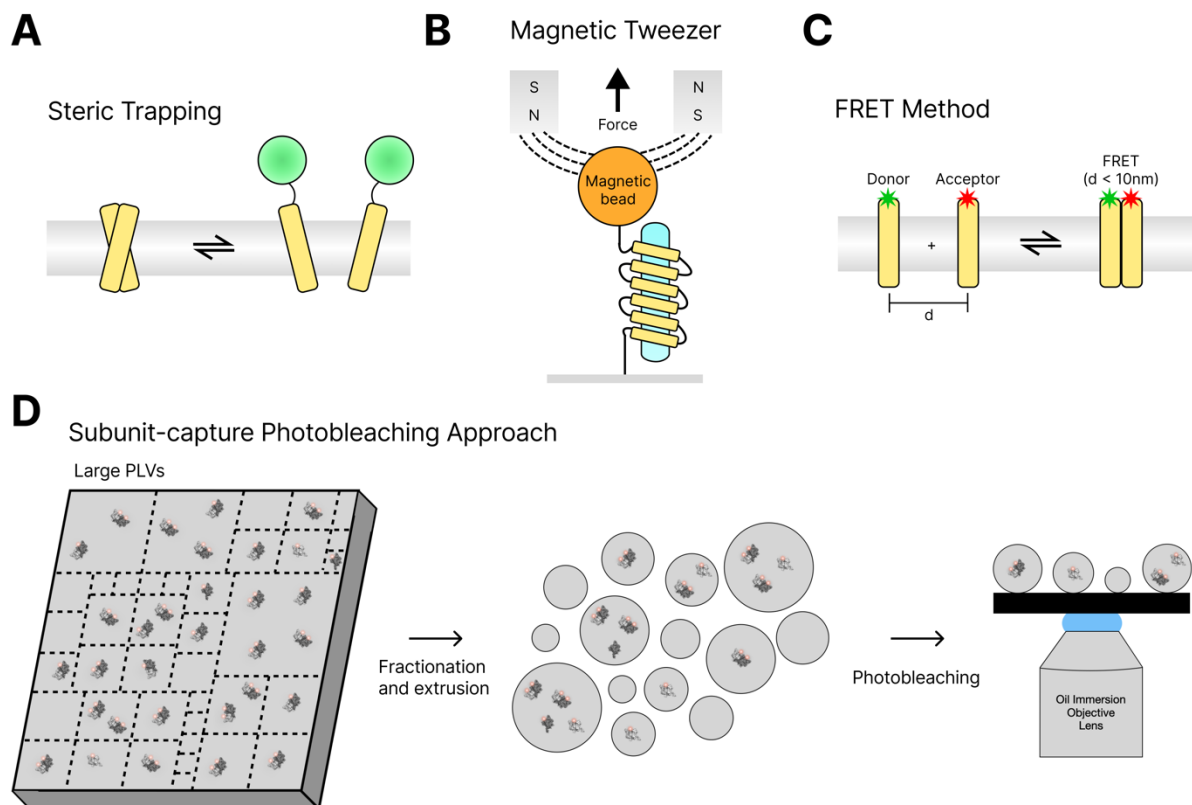


Figure 1. Various techniques to study thermodynamic stability of membrane proteins. (A) Steric trapping method is used to measure the thermodynamic protein (yellow) folding energies in membranes (grey) using the mSA (green) coupling to proteins (9). The figure is reconstructed and adapted from Mersch (2021) (17) and Hong et al. (2010) (18) (B) Magnetic tweezer technique is used to study the thermodynamic stability by investigating energy landscape of the second phase of membrane protein folding. Protein (yellow) within the bicelle (light blue) is linked to the glass slide (grey). Magnetic bead (orange) is being pulled by a magnetic force from the magnet (19). The figure is reconstructed and adapted from Mersch (2021) (17) and Min et al. (2015) (19). (C) FRET method is used to quantitatively measure the free energy of transmembrane helices. Donor (green) or acceptor (red) is attached to the protein (yellow). When the distance is closer to each other ($d < 10$ nm), energy transfer between the donor and acceptor occurs. The FRET method reveals the thermodynamic parameters for the formation of the antiparallel dimer using transmembrane helix (13). (D) Subunit-capture photobleaching approach is used to measure the thermodynamic stability in CLC-ec1 (14). Proteins in large paucilamellar vesicle state is extruded and the proteins are captured into each liposome. Extruded liposomes are imaged by TIRF microscope. The figure is reconstructed and adapted from Chadda et al. (2016) (14).

1.4 The CLC Family of Membrane Proteins as Model Systems for Studying Membrane Embedded Binding Thermodynamics

To investigate the questions raised at the beginning of this chapter, the research in this thesis uses a model system based on the homodimeric CLC-ec1 chloride/proton antiporter from *E. coli*. This section provides a background of the CLC superfamily. Next, the section presents the functional and structural features of CLC-ec1 with the detailed mechanisms of CLCs from the structure perspectives of CLCs, showing the reasons why CLC-ec1 is a suitable system for our studies.

1.4.1 The CLC Superfamily

The CLC superfamily is biologically ubiquitous, found in a wide range of organisms including plants, yeast, animals, archaeobacteria, and eubacteria. CLC plays a significant role in exchanging different ions including chloride (Cl⁻) and proton (H⁺) both in and out of cells. All members in the CLC superfamily exhibit a conserved structural organization, characterized by a transmembrane catalytic domain and additional cytoplasmic regulatory domains (20).

In 1979, bilayer recording on an artificial planar bilayer was first conducted on a voltage gated CLC channels from the electric organ of *Torpedo californica* discovering the single channel behavior (21). About a decade later, the research successfully identified the sequence of the first member of CLC voltage-gated chloride channel called CLC-0 by utilizing expression cloning from the electric organ of fish *Torpedo marmorata* (22). Since then, several studies were carried out to identify the other members of CLC family and to investigate functions of them. Researchers have identified 9 human CLC channels including CLC-1 to CLC-7, CLC-Ka, and CLC-Kb with their major functions. These CLC channels are divided into three groups with less than 30% identity

shared between them. The first group has CLC-1, CLC-2, CLC-Ka, and CLC-Kb channels, and the second group includes CLC-3, CLC-4, and CLC-5, and the third group involves CLC-6 and CLC-7 (23). Each mammalian CLC has a fundamental role in human body. For example, CLC-2 regulates transepithelial transport mainly in brain and kidney, and CLC-6 has a major function in ion homeostasis of late endosomes, while CLC-7 acidifies the resorption lacuna in osteoclasts. All of these eukaryotic CLC proteins contain two cystathionine β -synthetase (CBS) domains in the carboxyterminal portion while only half of the prokaryotic CLC proteins possess the domain (20, 24). The eukaryotic CLC structure for cmCLC including CBS domains was resolved at a 3.5 Å resolution with x-ray crystallography (3ORG in PDB) (25). The study also reveals that numerous disease-causing mutations in human CLC proteins are found at the CBS-transmembrane interface. (25). They are crucial as the mutations within the CBS domains in CLC proteins directly affect to the human diseases such as osteopetrosis, Dent's disease, and retinal degeneration. This indicates that CLC proteins are crucial components in human body (26).

In previous years, astonishing results were found regarding the behavior of the CLC family. The result indicated that CLC chloride channel family of chloride transporting proteins is divided into two groups: Cl⁻ channels and Cl⁻/H⁺ exchange transporters (27-31). Some homologues of the CLC family do not function as ion channels, but act as Cl⁻/H⁺ exchangers instead. This finding contrasts with the previous belief that the CLC family is solely Cl⁻ channels, and came as a big surprise. This result led researchers to hypothesize that the mechanism of ion-transport of these two types of CLCs may be similar, and CLC channels are “degraded-transporters” suggesting CLC-0 as a “broken” Cl⁻/H⁺ exchanger as the proton transport and the channel gating activities are coupled (32, 33).

1.4.2 Functional and Structural Characteristics of CLC-ec1

The bacterial CLC protein CLC-ec1 is a Cl^-/H^+ secondary active transporter that is expressed in the inner membrane of *E. coli* (**Fig. 2A, B**). The process of coupled transport involves the exchange of two chloride ions for one proton, but in the opposite direction across the membrane. Also, CLC-ec1 does not possess CBS domains but does have inter-subunit contacts between N- and C- terminal tails of its subunits unlike the mammalian CLC family. X-ray crystallography studies have determined the structures of wild-type and mutant CLC-ec1 at a resolution 3.5 Å (1KPK in PDB) (34). The x-ray crystallography revealed the complex structure of CLC-ec1 subunits including dimerization interface. The authors also found that CLC-ec1 has a single independent transport pathway formed on each subunit away from the dimerization interface. They identified 18 individual α -transmembrane helices included in the CLC-ec1 protein by labeling them from A-R starting from N-terminus to C-terminus of the protein (**Fig. 2B**). A year after, a more detailed structure of CLC-ec1 was obtained using x-ray crystallography obtaining a higher resolution of 2.8 Å (1OTS in PDB) (35). This structure revealed three chloride binding sites on each subunit forming the transport pathway, and the external site containing a glutamate residue, E148 that acts as a gate. Another research introduces three binding sites in the transport path with S_{int} , S_{cen} , and S_{ext} based on their location in CLC-ec1 (36). They explain two sites (S_{int} , S_{cen}) are occupied by Cl^- ions, but the Cl^- binding site S_{ext} is only filled by Cl^- ions when the wild-type glutamate residue is absent. This glutamate residue (Glu_{ex} : E148) extends its side-chain into the pore, blocking the pathway for Cl^- ions due to the presence of this negatively charged side-chain (36) (**Fig. 3A**). This glutamate residue is found in all vertebrate CLC channels except CLC-K, and it is believed to function as the gate of the channel (34, 35). When the glutamate residue is altered through mutation to a noncharged amino acid, a Cl^- ion appears at the location where it is occupied

by the negatively charged side-chain of the original glutamate (37). The mutation of the E148Q allows the pathway opening to extracellular solution as it is not blocking the pathway for Cl⁻ ion, and Cl⁻ ions will occupy all three binding sites which reflecting the active conformation (**Fig. 3B**). This corresponds to the finding that charge-neutralized Glu_{ex} (E148) mutation in CLC-0, 1, and 2 are open channels (35, 38, 39).

S_{cen} is positioned at the center of the ion-permeation pathway where the Cl⁻ ion is bound. The chloride ion at S_{cen} site is coordinated by the hydroxyl side-chain of S107 in helix D and the hydroxyl side-chain of Y445 in helix R. It is also demonstrated that the bound chloride ion interacts with the main-chain nitrogen atoms of I356 and F357 in helix N (34). The Cl⁻ ion occupies S_{cen} and Glu_{ex} occupies S_{ext} occludes the pathway towards the outer membrane. The ion-permeation pathway is narrowed at its extracellular end due to the presence of the N termini of helix F and helix N. Another Cl⁻ ion binding site is S_{int} located ~6 Å internal to S_{cen}. Cl⁻ ion at S_{int} is coordinated by the G106 and S107 which are the backbone amino group. This site is located at the position where the intracellular aqueous solution and the pore come together. In this binding site, there is a space that water molecules can hydrate the bound Cl⁻. (36). Even though each CLC homologue has different properties as previously mentioned, the gating mechanisms of the CLC family shares common features with the transport cycle suggesting a close evolutionary connection between transport and channel opening (33). The ion conduction and selectivity mechanisms have been better understood through the crystal structures. These structures show the importance of Glu_{ex} in regulating CLC channel gating and transport. Researchers have found that a protonatable residue must occupy Glu_{ex} position to gate or facilitate coupled transport (25, 27, 35, 38). With this information lacking in the crystal structures, Glu_{ex} has been considered as the sole gate regulating ion flux through both transporters and channels in CLCs (35).

In recent years, two models have been suggested to explain CLC function. The first model proposes that ion movement is controlled at one end of the pathway by Glu_{ex}, and at the other by a static kinetic barrier, created by steric constriction formed by Ser_{cen}, Tyr_{cen} (25). The second model suggests that Tyr_{cen} has an important role in intracellular pore gate in addition to Glu_{ex} in CLC (40). In the suggested model, Tyr_{cen} functions as the pH-independent inner gate which is a structural component that enables CLCs to keep the consistent exchange stoichiometry independent of both pH and turnover rate.

There have been efforts to discover the different characteristics in the CLC family between channel and transporter. However, the question “what kind of structural features make CLC-ec1 transporter not channel?” has not been clearly answered yet. Answering these questions will lead to more discoveries in the field of CLC. In addition, there was a study conducted with a monomeric version of CLC-ec1 induced from substitutions using bulky tryptophan residues at the dimerization interface to investigate how oligomerization of CLC-ec1 affects the biochemical and biophysical properties (41). Progress in recent research has elucidated the processes involved in the formation of CLC-ec1 dimers, shedding light on the role of the membrane and protein sidechains at the dimerization interface in the dimerization process (14-16, 42). Even with these several years of structural and functional studies of CLC proteins, the question of why CLC proteins form dimers still remains unclear.

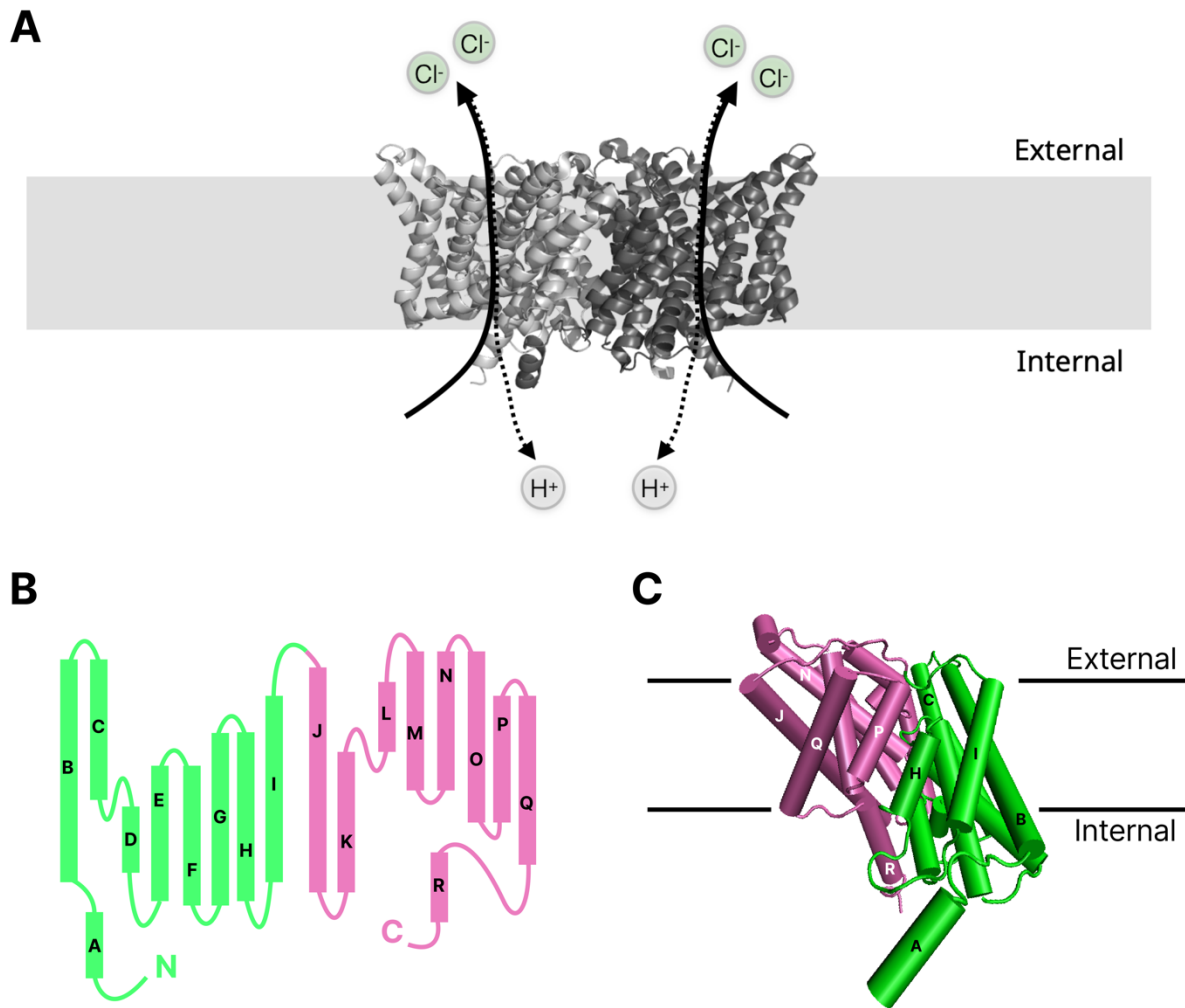


Figure 2. Structural characteristics of the CLC-ec1 homodimer (A) The bacterial CLC protein CLC-ec1 is a homo-dimeric Cl^-/H^+ antiporter native to *E. coli* inner membrane. Two subunits create a CLC-ec1 homodimer (light grey and dark grey). The cartoon was plotted from 1OTS in the PDB, obtained with a resolution 2.5 \AA (35). CLC-ec1 is illustrated within the membrane (grey). The arrow lines (solid, dotted) crossing the CLC-ec1 indicate transport pathways for chloride ions (green) and protons (white). The illustration shows that the stoichiometry of the transport is two chlorides out across the membrane for one proton in across the membrane in an opposite direction each other. (B) CLC-ec1 subunits contain 18 transmembrane helices. Dutzler et al. (2002) named each helix with a letter A-R (34). The figure represents that the first (N-Lobe, light green) half and the second (C-Lobe, mauve) half have a similar structure. (C) The structure of the N-Lobe of protein (light green) resembles with the structure of the C-Lobe (mauve) in CLC-ec1 subunit (1OTS in PDB) (pseudo-symmetry structure). The black solid line shows the external and internal membrane boundary. The protein is embedded in the lipid bilayer between the two black solid lines. The “internal” faces inward towards the cytoplasm, and the “external” side is oriented in the opposite direction. In the figure, CLC-ec1 is represented with cartoon cylinders. The figure is adapted from Dutzler et al. (2002) (34) and Mersch (2021) (17).

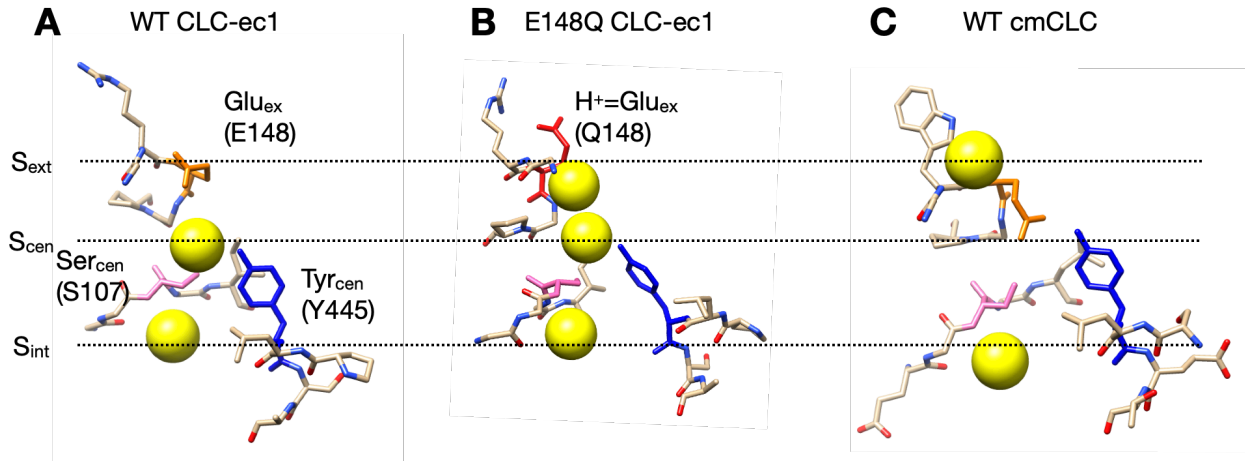


Figure 3. Structure for the CLC-ec1 function Detailed views of the three ion binding sites (S_{ext} , S_{cen} , S_{int}) of (A) WT CLC-ec1, (B) E148Q CLC-ec1, and (C) WT cmCLC. Glu_{ex} (E148) is shown in orange, Tyr_{cen} and Ser_{cen} are shown in blue and magenta, and Q148 is shown in red. The Cl^- ions are represented as spheres in yellow. PDB ID: WT CLC-ec1 (1OTS), CLC-ec1 E148Q (1OTU) and WT cmCLC (3ORG). The figure is adapted from Accardi et al. (2015) (43).

1.5 Measurements of CLC-ec1 Dimerization Equilibrium in Membranes

Because of the homodimeric, membrane embedded structure, CLC-ec1 has been a useful model system for studying in-membrane dimerization reactions. Previously, Robertson et al. (41) demonstrated that replacing tryptophan residues with I201W and I422W at the dimerization interface of CLC-ec1 resulted in a functionally folded, monomer form of the transporter in lipid membranes. To conduct fluorescence experiment, Chadda et al. (14) relocated a buried cysteine to the accessible position, C85A/H234C to increase the labeling efficiency with Cy5-maleimide without affecting the functionality on the protein. Single-exposed cysteine construct is referred as “WT”, and tryptophan mutated construct at I201W and I422W is referred as “IWIW”.

To quantify dimerization stability, the Robertson Laboratory developed a technique called “subunit capture method” (14, 15, 44). This technique is used to understand the thermodynamic

characteristics of CLC-ec1 dimerization by measuring the change in standard free energy $\Delta G^{\circ}_{Dimerization}$, (14-17, 44) and is used throughout this thesis. The basic idea of the subunit capture method is to locate the CLC-ec1 proteins into liposomes randomly, and the occupancy of the proteins will follow a Poisson distribution. However, there were some questions about studying equilibrium dimerization in membranes since the kinetics of membrane protein is extremely slow (45-47). To examine this, reversibility of the system was tested by carrying out a dilution study. They took a sample at high density where dimers would prevail and diluted it 1000 fold in the lipid bilayer to see if the system is shifted to the expected increased monomeric proportion. They observed that the probability distribution converges to the same end-point where the dimerization equilibrium was already reached in reconstituted sample at the identical concentration. This result represents that CLC-ec1 dimerization reaction is reversible and that they can study thermodynamics of CLC-ec1 dimerization using the subunit capture technique (44).

The Robertson Laboratory applied two experimental controls in 2:1 POPE/POPG liposomes to calculate the accurate value of $\Delta G^{\circ}_{Dimerization}$ using experimental photobleaching distributions. The monomer control they used is IWIW previously introduced earlier, and the dimer control they used is R230C/L249C, named “RCLC”, which is a constitutive dimer induced from disulfide bonds at the dimerization interface. These controls were known to have similar properties as the WT CLC-ec1 (41, 48). With these controls, Robertson Laboratory was able to obtain the accurate value of a free energy of dimerization, $\Delta G^{\circ}_{Dimerization}$ with -10.9 kcal/mol corresponding to a thermodynamically stable complex in 2:1 POPE/POPG lipid bilayers relative to 1 subunit/lipid standard state (14).

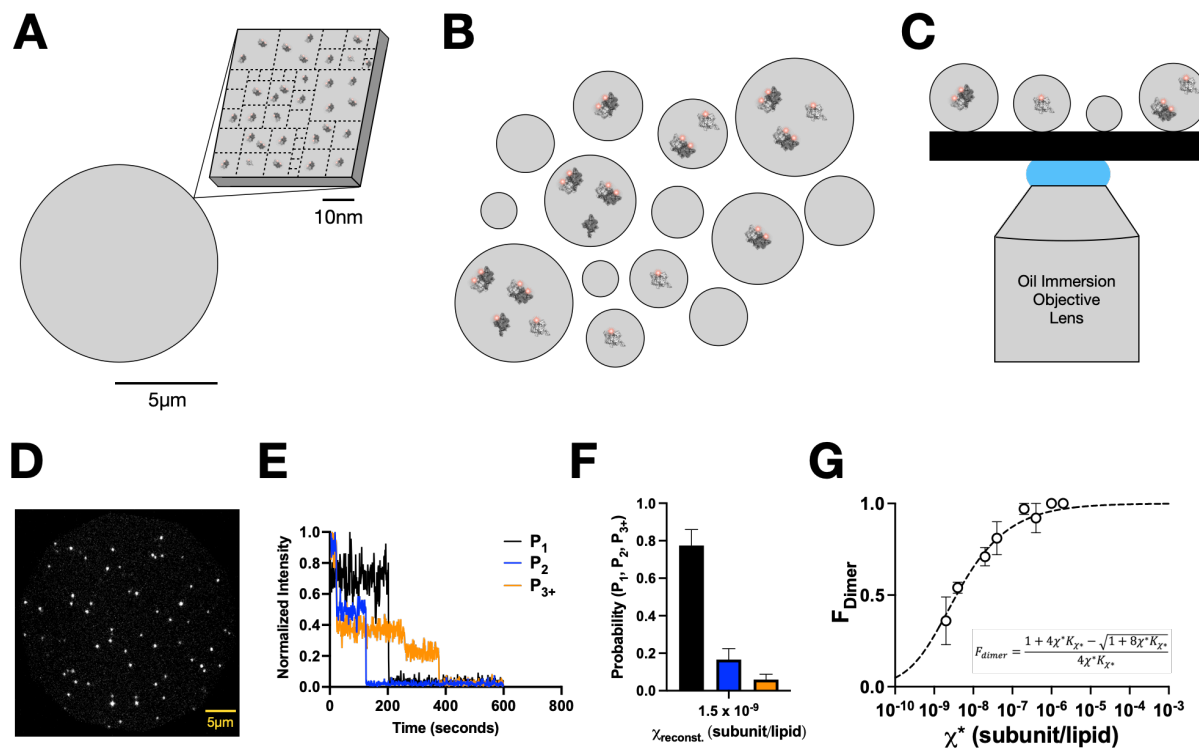


Figure 4. Subunit capture single molecule photobleaching method to measure the thermodynamic stability of CLC-ec1 (A) A cartoon of the proteoliposomes samples (grey sphere) with CLC-ec1 subunits labeled with Cy5 fluorophore. The radius of the liposome is indicated (5 μm scale bar in black). Magnified portion of the liposome represents CLC-ec1 subunits diffused in the large membrane (rectangle in grey). Dotted line shows the fractionation when the liposome is extruded through the 400 nm polycarbonate membrane. (10 nm scale bar in black) (B) Proteoliposomes (grey spheres) are filtered through a 400 nm polycarbonate membrane for 21 times using an extruder to create small unilamellar vesicles containing captured Cy5 labeled CLC-ec1 subunits. (C) The small unilamellar vesicles are placed onto the coverslip (black) and imaged with the oil immersion objective lens. A small amount of oil is applied between the objective lens and the coverslip. (D) A single molecule TIRF image. Each spot is emitted light of Cy5-fluorophores after excited by a laser with 637 nm wavelength. Normalized photobleaching traces as a function of time. Three datasets represent one step (P_1 : Black), two steps (P_2 : Blue), and three steps (P_{3+} : Orange). The drop in photobleaching intensity represents the photobleaching event happening during imaging. (E) Photobleaching probability histogram at $\chi_{reconst.} = 1.5 \times 10^{-9}$ subunit/lipid was plotted from (D) and I which correspond to the counting of 1, 2, 3+ steps from the image of (D). (F) The fraction of dimer was calculated from the least squared analysis of the residuals, R^2 , with the experimental monomer control “I201W/I422W” and the experimental dimer control “R230C/L249C”. Finally, the equilibrium constant (K_{χ^*}) was estimated by fitting the F_{Dimer} versus χ^* (the reactive mole fraction). The equation in the plot shows the dimerization isotherm. The Robertson Laboratory found that the equilibrium constant indicated that the protein had a dissociation constant (K_D) of 2×10^{-8} subunits/lipid, corresponding to a thermodynamically stable complex with a free energy -10.9 kcal/mol in 2:1 POPE/POPG lipid bilayers relative to the 1 subunit/lipid standard state (15). The figure is reconstructed and adapted from the previous literature Chadda et al. (2016) (14) and Mersch (2021) (17).

In addition, the Robertson Laboratory studied CLC-ec1 dimerization energetics with shorter chain DL lipids using this subunit capture method (42). They examined the dimerization equilibrium of CLC-ec1 depending on the DL/PO ratio by titrating DL in the membrane from 10⁸ to 80 %. The research found that increasing the amount of short-chain lipid decreases CLC dimer stability. The data showed that CLC-ec1 is destabilized by 0.8 ± 0.3 kcal/mole for every 10 % increase of DL in the membrane at $DL > 1$ %. On the other hand, $\Delta\Delta G$ represents a linear dependency on the logarithm plot of DL with a destabilization of 0.14 ± 0.07 kcal/mole for the change in % DL for every Log_{10} at $DL < 1$ %.

1.6 van 't Hoff Analysis for Dissecting Thermodynamic Changes in Protein Stability Equilibrium

Binding and complexation processes have been a great interest in various fields of research (49-51). However, there have been difficulties in quantitatively studying the thermodynamic parameters due to the experimental limitations on membrane proteins. Even with the difficulties, there was a study that has explored thermodynamic parameters of membrane proteins from oligomerization of transmembrane helices. Yano et al. (13) have measured the enthalpy and the entropy change with the free energy of the dimerization using transmembrane helix (AALALAA)₃ within the different types of membranes using van 't Hoff analysis combining with FRET method. The authors reported that the helix starts to show a non-linearity in free energy when the PC lipid length is 22 in the temperature range 5-55 °C which indicates the involvement of the negative change in heat capacity. Thermodynamic parameters could be extracted using the analysis method called van 't Hoff analysis of the temperature dependence of the dimerization equilibrium constant (K_{eq}). The standard state Gibbs free energy, ΔG° is represented as

$$\Delta G^\circ = -RT \ln(K_{eq} \cdot \chi^\circ) \quad (1)$$

where R is an ideal gas constant, T is a temperature in Kelvin, K_{eq} is a thermodynamic equilibrium constant, χ° is the standard-state in mole fraction units as 1 subunit/lipid. When proteins and surrounding solvents (e.g., lipids or water molecules) possess heat capacity as previously explained, the relationship will be non-linear. In this environment, the enthalpy and entropy changes will depend on the temperature:

$$\Delta H^\circ(T) = \Delta H_0^\circ + \Delta C_p(T - T_0) \quad (2)$$

$$\Delta S^\circ(T) = \Delta S_0^\circ + \Delta C_p \ln(T/T_0) \quad (3)$$

where ΔC_p is the change in molar heat capacity, T_0 is an arbitrary reference temperature, and ΔH_0° and ΔS_0° are the respective changes in enthalpy and entropy at the reference temperature.

Combining the equations above, the van 't Hoff equation has non-linear relationship:

$$\ln(K_{eq} \cdot \chi^\circ) = \left(-\frac{\Delta H_0^\circ}{RT} - \frac{\Delta C_p}{R} \left(1 - \frac{T_0}{T}\right) - \frac{\Delta C_p}{R} \ln\left(\frac{T_0}{T}\right) \right) + \frac{\Delta S_0^\circ}{R} \quad (4)$$

With this, non-linear curve-fitting of $\ln(K_{eq} \cdot \chi^\circ)$ vs. $1/T$ can provide thermodynamic parameters ΔH_0° , ΔS_0° , T_0 , and ΔC_p . On the other hand, when considering the case where the enthalpy and the entropy changes are temperature independent, this will allow:

$$\Delta G^\circ = \Delta H^\circ - T\Delta S^\circ \quad (5)$$

Where ΔH° and ΔS° are the changes in enthalpy and entropy in a standard state. Combining two of the equations yields the linear van 't Hoff equation:

$$\ln(K_{eq} \cdot \chi^\circ) = -\frac{\Delta H^\circ}{R} \frac{1}{T} + \frac{\Delta S^\circ}{R} \quad (6)$$

This slope of this will be $-\Delta H^\circ/R$ by representing the enthalpy change, and y-intercept of this plot will be $\Delta S^\circ/R$ showing the entropy change involved in the dimerization reaction.

1.7 Subunit-Exchange Kinetics to Measure Kinetics of Binding Complexes

Subunits can bind together, and they can dissociate reversibly. This means that they become free subunits, and they can associate with other subunits. The kinetics of association and dissociation rates are represented as k_{on} and k_{off} . Studying kinetics in biological system is important as it provides us valuable information about timescales related to different species in the system.

Throughout the thesis, bulk FRET assays are used to characterize the subunit exchange kinetics of CLC-ec1. We observe the signal from the subunit exchange dimerization reaction when the CLC-ec1 subunits form a heterodimer. It measures the macroscopic FRET signals from the donor and acceptor over time. The kinetic information is obtained by fitting the FRET signal that is obtained from new forming heterodimers. Pan (52) derives dissociation rate constant of protein complexes of their subunit exchange from theoretical modeling. They proposed a novel method called Metabolically-labeled Affinity-tagged Subunit Exchange to measure (k_{off}) with metabolic stable isotope labeling, affinity purification and mass spectrometry. Based on this, the equations for CLC-ec1 subunit exchange experiment can be modified and written as follows:





where Cy5 labeled CLC-ec1 subunit is represented as A, and Cy3 labeled CLC-ec1 subunit is represented as B. In the equilibrium state, the number of monomers does not change over time.

Thus,

$$\frac{dA(t)}{dt} = 0 \quad (10)$$

$$\frac{dB(t)}{dt} = 0 \quad (11)$$

Considering that AB is produced after the reaction happens, the kinetics of reaction can be described as:

$$\frac{dAB(t)}{dt} = k_{on}A_0B_0 - k_{off}AB(t) \quad (12)$$

Where A_0 and B_0 are the initial concentration of A and B respectively. By solving this differential equation with initial condition

$$AB_{t=0} = 0 \quad (13)$$

The value of AB at time point t is represented as

$$AB(t) = -\frac{1}{k_{off}}(e^{-k_{off}t} \cdot k_{on}A_0B_0) + \frac{k_{on}}{k_{off}}A_0B_0 \quad (14)$$

Considering that

$$K_{eq} = \frac{k_{on}}{k_{off}} \quad (15)$$

Finally, newly formed heterodimer Cy3 and Cy5 labeled one on each subunit AB as a function of time is represented as follows:

$$AB(t) = -K_{eq}A_0B_0(1 - e^{-k_{off}t}) \quad (16)$$

Like this, the subunit exchange kinetic information is measured as dissociation rate constant (k_{off}) with a nonlinear one-phase exponential association model: $[AB] = [AB]_{eq}(1 - \exp(-k_{off}t))$ where $[AB]_{eq}$ is a new heterodimer construct at equilibrium, and $[AB]$ which is observed as a FRET signal is a new heterodimer construct at a given incubation time t .

1.8 Summary

The content presented in this section has established the fundamentals for addressing the question posed at the beginning of the introduction in this chapter: 1. Why do hydrophobic membrane proteins in the membrane, form stable complexes with other hydrophobic proteins instead of interacting with the similarly hydrophobic solvent? 2. Why do membrane protein exhibit slower dimerization kinetics? 3. Does the dimerization present a mechanism for regulating the functional behavior of each subunit?

There have not been many thermodynamic and kinetic studies on the dimerization reactions in the membrane protein systems discovered yet, and there have not been definitive answers on that. Combining different methods such as subunit capture method, FRET, and chloride functional

assays with our model membrane protein CLC-ec1 will allow us to understand the origin of driving forces of CLC-ec1 in lipid bilayers with the thermodynamic parameters involved and the regulating mechanisms depending on the oligomerization state. In addition, establishing the methods with molecular dynamic simulations to calculate the packing density with different types of small molecules between the subunits will open the door to the dimerization kinetics considering the transition energy state which could be related to the cavity volume between the subunits.

1.9 Description of Thesis Content

Chapter 2 represents the protocols and materials used throughout the thesis. The chapter starts from the solutions used in the protocols. Then, it explains each experimental methods applied within this thesis. The protocol includes protein purification, protein labeling, preparation of proteoliposomes, chloride transport function measurement, bulk Förster resonance energy transfer (FRET) measurement, and single molecule subunit capture method. The methods described in this chapter were reported in a manuscript “A thermodynamic analysis of CLC transporter dimerization in lipid bilayers” (53).

Chapter 3 introduces supporting materials which contains alignment protocols of the *Lambda III* total internal reflection fluorescence (TIRF) microscope used thoroughly within the thesis for the single-molecule experiment. TIRF microscope is an open laser microscope which is fully customizable and follows the co-localization single molecule spectroscopy (CoSMoS) design first implemented by the Gelles Laboratory at Brandeis University. This microscope is used in Chapter 4 for single-molecule imaging to study thermodynamic stability of CLC-ec1. This tutorial includes a document so that anyone who builds this microscope can easily align the microscope and saves a lot of time.

Chapter 4 starts from the question “Why do greasy membrane proteins, form stable complexes with other greasy proteins instead of interacting with the greasy lipid solvent?”. The physical reason behind the stability of the membrane protein is not well understood because the oligomerization happens via the burial of hydrophobic interfaces. However, there is little water existing in the membrane, and the hydrophobic effect should not be affected. To investigate this further, we carry out a van ’t Hoff analysis of the temperature dependency of the dimerization to quantify thermodynamic changes (ΔG°) associated with CLC-ec1 dimerization in the membranes. For this study, we use Förster Resonance Energy Transfer method to ensure that the reaction reached the dimerization equilibrium end-point on different conditions. Finally, single-molecule subunit capture method is used to measure the CLC-ec1 dimer stability as a function of temperature followed by van ’t Hoff analysis. The findings in this chapter were reported in a manuscript with a title “A thermodynamic analysis of CLC transporter dimerization in lipid bilayers” (53).

Chapter 5 starts from a question: “Why the kinetics of dimerization is slower than most biological reactions taking weeks to equilibrate at 22 °C in lipid bilayers?”. From the previous studies (14, 53), we found that CLC-ec1 dimerization reaction shows extremely slow kinetics at 22 °C taking several weeks to reach equilibrium. We hypothesize the dimerization reaction involves a high-energy transition state that requires the formation of a vacuum cavity in between the two subunits inaccessible to the surrounding solvent. This chapter shows the density analysis between the dimerization interfaces based on the coarse-grained molecular dynamic simulations. Coarse-grained molecular dynamics (CGMD) simulations are performed for 20 μ s to quantify the density in the dimerization interface with different compositions of small molecules with benzene and lysolipids at different inter-subunit separations as they are separated from 4 to 24 Å. Self-

developed Python script using MDAnalysis Python library allowed us to analyze molecular density in a separate system at various subunit distances.

In **Chapter 6**, we explore the concept of whether the dimerization of CLC-ec1 provides a mechanism for regulating the transport function in each individual monomer. It is widely observed that most membrane proteins establish stable complexes within the membrane. Previous research has provided evidence that a considerable portion of membrane protein structures in the Protein Data Bank (PDB) exist as oligomers. Therefore, **Chapter 6** aims to examine how the distinct functional states of CLC-ec1 influence the characteristics of its dimer state, including thermodynamic and kinetics stabilities as well as its tendency to undergo dynamic equilibrium reactions. We propose that the stability of the proteins decreases under activating conditions such as low pH or channel activity compared to inactive conditions like high pH or the transporter state. Moreover, we suggest that proteins in a locked-in dimer state will exhibit enhanced conformational stability, potentially resulting in the loss of their transport function. To investigate these hypotheses, we investigate the dimerization reactions at different pH levels. We also compare the dimerization reactions between the transporter version and the channel version of CLC. The findings from this research indicate a connection between the dimerization of CLC-ec1 and its stability.

The **Chapter 7**, the last section of this thesis delves into a discussion regarding how this research influences our comprehension of the kinetics and thermodynamics of membrane protein oligomerization in a broader context. It focuses on future directions that will build upon this fundamental research.

References

1. R. E. Jacobs, S. H. White, The Nature of the Hydrophobic Binding of Small Peptides at the Bilayer Interface - Implications for the Insertion of Transbilayer Helices. *Biochemistry* **28**, 3421-3437 (1989).
2. M. Milik, J. Skolnick, Insertion of Peptide Chains into Lipid-Membranes - an Off-Lattice Monte-Carlo Dynamics Model. *Proteins* **15**, 10-25 (1993).
3. J. L. Popot, D. M. Engelman, Membrane protein folding and oligomerization: the two-stage model. *Biochemistry* **29**, 4031-4037 (1990).
4. J. L. Popot, S. E. Gerchman, D. M. Engelman, Refolding of bacteriorhodopsin in lipid bilayers. A thermodynamically controlled two-stage process. *J Mol Biol* **198**, 655-676 (1987).
5. S. H. White, W. C. Wimley, Membrane protein folding and stability: physical principles. *Annu Rev Biophys Biomol Struct* **28**, 319-365 (1999).
6. K. G. Fleming, A. L. Ackerman, D. M. Engelman, The effect of point mutations on the free energy of transmembrane alpha-helix dimerization. *J Mol Biol* **272**, 266-275 (1997).
7. K. R. MacKenzie, D. M. Engelman, Structure-based prediction of the stability of transmembrane helix-helix interactions: the sequence dependence of glycophorin A dimerization. *Proc Natl Acad Sci U S A* **95**, 3583-3590 (1998).
8. R. Guo *et al.*, Steric trapping reveals a cooperativity network in the intramembrane protease GlpG. *Nat Chem Biol* **12**, 353-360 (2016).
9. H. Hong, Y. C. Chang, J. U. Bowie, Measuring transmembrane helix interaction strengths in lipid bilayers using steric trapping. *Methods Mol Biol* **1063**, 37-56 (2013).
10. H. K. Choi *et al.*, Watching helical membrane proteins fold reveals a common N-to-C-terminal folding pathway. *Science* **366**, 1150-1156 (2019).
11. G. I. Bell, Models for the specific adhesion of cells to cells. *Science* **200**, 618-627 (1978).
12. O. K. Dudko, G. Hummer, A. Szabo, Intrinsic rates and activation free energies from single-molecule pulling experiments. *Phys Rev Lett* **96**, 108101 (2006).
13. Y. Yano, K. Matsuzaki, Measurement of thermodynamic parameters for hydrophobic mismatch 1: self-association of a transmembrane helix. *Biochemistry* **45**, 3370-3378 (2006).
14. R. Chadda *et al.*, The dimerization equilibrium of a ClC Cl(-)/H(+) antiporter in lipid bilayers. *Elife* **5** (2016).

15. R. Chadda, L. Cliff, M. Brimberry, J. L. Robertson, A model-free method for measuring dimerization free energies of CLC-ec1 in lipid bilayers. *J Gen Physiol* **150**, 355-365 (2018).
16. K. Mersch, T. N. Ozturk, K. Park, H. H. Lim, J. L. Robertson, Altering CLC stoichiometry by reducing non-polar side-chains at the dimerization interface. *J Mol Biol* **433**, 166886 (2021).
17. K. N. Mersch (2021) Protein Determinants of CLC-ec1 Stoichiometry. (The University of Iowa, United States -- Iowa), p 204.
18. H. Hong, T. M. Blois, Z. Cao, J. U. Bowie, Method to measure strong protein-protein interactions in lipid bilayers using a steric trap. *Proc Natl Acad Sci U S A* **107**, 19802-19807 (2010).
19. D. Min, R. E. Jefferson, J. U. Bowie, T. Y. Yoon, Mapping the energy landscape for second-stage folding of a single membrane protein. *Nat Chem Biol* **11**, 981-987 (2015).
20. R. Dutzler, The ClC family of chloride channels and transporters. *Curr Opin Struct Biol* **16**, 439-446 (2006).
21. M. M. White, C. Miller, A voltage-gated anion channel from the electric organ of *Torpedo californica*. *J Biol Chem* **254**, 10161-10166 (1979).
22. T. J. Jentsch, K. Steinmeyer, G. Schwarz, Primary structure of *Torpedo marmorata* chloride channel isolated by expression cloning in *Xenopus* oocytes. *Nature* **348**, 510-514 (1990).
23. T. J. Jentsch, Discovery of CLC transport proteins: cloning, structure, function and pathophysiology. *J Physiol* **593**, 4091-4109 (2015).
24. A. Accardi, A. Picollo, CLC channels and transporters: proteins with borderline personalities. *Biochim Biophys Acta* **1798**, 1457-1464 (2010).
25. L. Feng, E. B. Campbell, Y. Hsiung, R. MacKinnon, Structure of a eukaryotic CLC transporter defines an intermediate state in the transport cycle. *Science* **330**, 635-641 (2010).
26. T. J. Jentsch, CLC chloride channels and transporters: from genes to protein structure, pathology and physiology. *Crit Rev Biochem Mol Biol* **43**, 3-36 (2008).
27. A. Accardi, C. Miller, Secondary active transport mediated by a prokaryotic homologue of ClC Cl- channels. *Nature* **427**, 803-807 (2004).
28. D. R. Poroca, R. M. Pelis, V. M. Chappe, ClC Channels and Transporters: Structure, Physiological Functions, and Implications in Human Chloride Channelopathies. *Front Pharmacol* **8**, 151 (2017).

29. A. Picollo, M. Pusch, Chloride/proton antiporter activity of mammalian CLC proteins CLC-4 and CLC-5. *Nature* **436**, 420-423 (2005).
30. O. Scheel, A. A. Zdebik, S. Lourdel, T. J. Jentsch, Voltage-dependent electrogenic chloride/proton exchange by endosomal CLC proteins. *Nature* **436**, 424-427 (2005).
31. A. R. Graves, P. K. Curran, C. L. Smith, J. A. Mindell, The Cl(-)/H(+) antiporter CLC-7 is the primary chloride permeation pathway in lysosomes. *Nature* **453**, 788-792 (2008).
32. J. Lisal, M. Maduke, The CLC-0 chloride channel is a 'broken' Cl-/H+ antiporter. *Nat Struct Mol Biol* **15**, 805-810 (2008).
33. C. Miller, CLC chloride channels viewed through a transporter lens. *Nature* **440**, 484-489 (2006).
34. R. Dutzler, E. B. Campbell, M. Cadene, B. T. Chait, R. MacKinnon, X-ray structure of a CLC chloride channel at 3.0 Å reveals the molecular basis of anion selectivity. *Nature* **415**, 287-294 (2002).
35. R. Dutzler, E. B. Campbell, R. MacKinnon, Gating the selectivity filter in CLC chloride channels. *Science* **300**, 108-112 (2003).
36. T. Y. Chen, Structure and function of clc channels. *Annu Rev Physiol* **67**, 809-839 (2005).
37. R. Dutzler, E. B. Campbell, R. MacKinnon, Gating the selectivity filter in CLC chloride channels. *Science* **300**, 108-112 (2003).
38. S. Traverso, L. Elia, M. Pusch, Gating competence of constitutively open CLC-0 mutants revealed by the interaction with a small organic inhibitor. *J Gen Physiol* **122**, 295-306 (2003).
39. L. Zuniga *et al.*, The voltage-dependent CLC-2 chloride channel has a dual gating mechanism. *J Physiol* **555**, 671-682 (2004).
40. B. Bennetts, M. W. Parker, Molecular determinants of common gating of a CLC chloride channel. *Nat Commun* **4**, 2507 (2013).
41. J. L. Robertson, L. Kolmakova-Partensky, C. Miller, Design, function and structure of a monomeric CLC transporter. *Nature* **468**, 844-847 (2010).
42. R. Chadda *et al.*, Membrane transporter dimerization driven by differential lipid solvation energetics of dissociated and associated states. *Elife* **10** (2021).
43. A. Accardi, Structure and gating of CLC channels and exchangers. *J Physiol* **593**, 4129-4138 (2015).

44. R. Chadda, J. L. Robertson, Measuring Membrane Protein Dimerization Equilibrium in Lipid Bilayers by Single-Molecule Fluorescence Microscopy. *Methods Enzymol* **581**, 53-82 (2016).
45. R. E. Jefferson, T. M. Blois, J. U. Bowie, Membrane proteins can have high kinetic stability. *J Am Chem Soc* **135**, 15183-15190 (2013).
46. M. Manning, W. Colon, Structural basis of protein kinetic stability: resistance to sodium dodecyl sulfate suggests a central role for rigidity and a bias toward beta-sheet structure. *Biochemistry* **43**, 11248-11254 (2004).
47. C. P. Moon, S. Kwon, K. G. Fleming, Overcoming hysteresis to attain reversible equilibrium folding for outer membrane phospholipase A in phospholipid bilayers. *J Mol Biol* **413**, 484-494 (2011).
48. W. Nguitragool, C. Miller, CLC Cl⁻/H⁺ transporters constrained by covalent cross-linking. *Proc Natl Acad Sci U S A* **104**, 20659-20665 (2007).
49. L. S. Mizoue, J. Tellinghuisen, Calorimetric vs. van't Hoff binding enthalpies from isothermal titration calorimetry: Ba²⁺-crown ether complexation. *Biophysical Chemistry* **110**, 15-24 (2004).
50. A. Niedzwiecka, E. Darzynkiewicz, R. Stolarski, Thermodynamics of mRNA 5' cap binding by eukaryotic translation initiation factor eIF4E. *Biochemistry* **43**, 13305-13317 (2004).
51. R. I. Boysen, A. J. O. Jong, M. T. W. Hearn, Binding behaviour and conformational properties of globular proteins in the presence of immobilised non-polar ligands used in reversed-phase liquid chromatography. *J Chromatogr A* **1079**, 173-186 (2005).
52. C. L. Pan, Measuring Dissociation Rate Constants of Protein Complexes through Subunit Exchange: Experimental Design and Theoretical Modeling. *Plos One* **6** (2011).
53. R. Chadda *et al.*, A thermodynamic analysis of CLC transporter dimerization in lipid bilayers. *Proc Natl Acad Sci U S A* **120**, e2305100120 (2023).

Chapter 2: Materials and Methods

2.1 Preface to the Chapter

The objective of this chapter is to show details about the general experimental and simulation methodologies used for data collection and data analysis throughout the thesis. This chapter follows some of the methods previously described by Mersch (2021) (1). The specific experimental and simulation materials and methods used in each chapter can be found in the “Materials and Methods section” of individual chapter.

2.2 Buffers

The buffers are prepared as previously introduced by Mersch (1). **Breaking buffer (BB):** 100 mM Sodium Chloride (NaCl, Research Products International (RPI), Mount Prospect, IL), 50 mM Tris(hydroxymethyl)aminomethane (RPI), 5mM Tris(2-carboxyethyl)phosphine HCl (TCEP, Soltec Ventures, Beverly, MA), pH 7.5. **Cobalt wash buffer (CoWB):** 100 mM NaCl, 20 mM Tris, 1 mM TCEP, 5 mM n-Decyl-B-D-Maltopyranoside (DM, Anatrace, Maumee, OH), pH 7.5. **Dialysis buffer (DB):** 300 mM Potassium Chloride (KCl, RPI), 20 mM Citrate (RPI), pH 4.5. **External Buffer (EB):** 150 mM Potassium Sulphate (K₂SO₄, Sigma-Aldrich, Saint Louis, MO), 1 mM KCl, 20 mM Citrate, pH 4.5. **Size exclusion buffer (SEB):** 150 mM NaCl, 20 mM 3-(N-morpholino)propanesulfonic acid (MOPS, RPI), 5 mM DM, pH 7.0.

2.3 Protein Purification

Protein purification was carried out based on the protocols introduced previously (1-4). Competent BL21-AI *E. coli* cells were transformed with a plasmid (pASK90 vector) to express

CLC-ec1 constructs. 1L of terrific broth that contains 4 mL of glycerol in each flask were inoculated with transformed *E. coli* with 1mL of 100 µg/mL ampicillin (GoldBio, Olivette, MO) each. The culture flasks were incubated at 37 °C with a shaker speed 225 RPM. Once the OD₆₀₀ reaches to 1.0, protein expression was induced with 0.2 mg/mL anhydro-tetracycline in dimethylformamide (aTC, Sigma-Aldrich). After the induction, the flasks were incubated for 3 hours, and cells were harvested (5000 × g (rcf), 20 minutes, 4 °C). The pellets were resuspended in BB to a volume of 50 mL with 10 µg lysozyme (RPI), 0.6 µM aprotinin (GoldBio), 0.84 µM leupeptin (Thermo Fisher Scientific, Waltham, MA), 10 µg DNAase (Sigma-Aldrich), 1 mM PMSF (RPI), 0.56 µM pepstatin (Thermo Fisher Scientific) to lyse the cells by sonication. 2% (w/v) of sol-grade DM was added to extract the membrane proteins under rotation for 2 hours at 22 °C. Then, the cell lysates were pelleted down (16000 RPM, 45 minutes, 4 °C) to obtain supernatant. The supernatant was loaded into a CoWB equilibrated cobalt metal affinity column (Takara Bio USA, Ann Arbor, MI). The column was washed with 20 mL of 20 mM Imidazole (RPI). Then, the protein was eluted using 400mM Imidazole (RPI). Eluted protein was concentrated by 10,000 MWCO centrifugal filter (Millipore-Sigma, Saint Louis, MO). Finally, concentrated protein was injected to a Superdex 200 Increase Size Exclusion Column (GE Life Sciences, Little Chalfont, UK) equilibrated with SEB, and CLC-ec1 protein was collected on a fraction collector from column #13 through #16 to make 1 ml volume. Obtained proteins were quantified by the Nanodrop 2000c UV-visible light spectrophotometer (Thermo Fisher Scientific) using absorbance spectra at a wavelength 280 nm.

2.4 Site Specific Labeling of CLC-ec1 using Cy3-Maleimide and Cy5-Maleimide

Fluorophore maleimide labeling was carried out with the technique described previously (1, 2). CLC-ec1 should be labeled for bulk Förster resonance energy transfer (FRET) experiment and single molecule photobleaching experiment. Initially, a protein concentration of 10 μM underwent a reaction with 50 μM of Cy3-(Cyanine 3-) or Cy5- (Cyanine 5-) or a combination of both Cy3- (Cyanine 3-) and Cy5- (Cyanine 5-) (referred to as Cy3/5) maleimide in DMSO (obtained from Lumiprobe Corporation, Hunt Valley, MD) for a duration of 10 minutes. The reaction was quenched with 5 mM cysteine from a 100 mM cysteine stock in SEB, pH adjusted to 7.0. The free dye was removed by re-binding the protein to a 0.2 mL cobalt affinity column (Talon), equilibrated in cobalt wash buffer, followed by excessive washing with 10-15 CV of CoWB and then elution with CoWB containing 400 mM imidazole, pH 7.5. As a final step, the imidazole was removed by running the eluted sample on a 3 mL Sephadex G-50 size exclusion column (Sigma-Aldrich). The quantification of the labeling efficiency was performed by placing the sample in a 1 cm quartz cuvette and analyzing it with a Nanodrop 2000c UV-VIS spectrophotometer. The absorbance spectrum was measured within the range of 190-840 nm. The protein concentration in the presence of Cy5 (or Cyanine 5) was determined using the following calculation:

$$[protein_{Cy5}] = \frac{A_{280} - (A_{Cy5,max} \times CF_{Cy5,280})}{\epsilon_{protein}} \quad (1)$$

where A_{280} represents the absorbance at a wavelength 280 nm, $A_{Cy5,max}$ is the peak absorbance of Cy5 ≈ 653 nm, $CF_{Cy5,280} = 0.017$ ($CF_{Cy5,280} = 0.05$ for Cyanine 5), is the correction factor for the absorbance of Cy5 at 280 nm, and $\epsilon_{protein}$ represents the extinction coefficient of the protein,

$\epsilon_{CLC-ec1} = 46,020 \text{ M}^{-1} \text{ cm}^{-1}$, when measured at a wavelength 280 nm. The subunit labeling yield, P_{Cy5} , is determined by:

$$P_{Cy5} = \frac{A_{Cy5,max}}{[protein_{Cy5}] \times \epsilon_{Cy5}} \quad (2)$$

where, $\epsilon_{Cy5} = 2.5 \times 10^5 \text{ M}^{-1} \text{ cm}^{-1}$ is the extinction coefficient for Cy5 at 653 nm. For the FRET studies, protein was labelled with Cy3-maleimide (Lumiprobe) or simultaneously co-labelled with Cy3- and Cy5-maleimide. When only Cy3 fluorophore was used, the same procedure was followed, except that the quantification was adjusted to account for the contribution of Cy3 at 280 nm. As a result, the protein concentration in the presence of Cy3 is determined as:

$$[protein_{Cy3}] = \frac{A_{280} - (A_{Cy3,max} \times CF_{Cy3,280})}{\epsilon_{protein}} \quad (3)$$

where $A_{Cy3,max}$ is the peak absorbance of Cy3 $\approx 555 \text{ nm}$, and $CF_{Cy3,280} = 0.08$ is the correction factor for the absorbance of Cy3 at 280 nm. The subunit labeling yield, P_{Cy3} , is calculated as:

$$P_{Cy3} = \frac{A_{Cy3,max}}{[protein_{Cy3}] \times \epsilon_{Cy3}} \quad (4)$$

where, $\epsilon_{Cy3} = 1.5 \times 10^5 \text{ M}^{-1} \text{ cm}^{-1}$ is the extinction coefficient for Cy3 at 555 nm. For labeling of Cy3 and Cy5 simultaneously, there are two correction factors that need to be considered, Cy3 and Cy5 absorbance at 280, as well as the contribution of Cy5 absorbance in the Cy3 peak. Thus, the protein concentration in the presence of Cy3 and Cy5 is calculated as:

$$\begin{aligned}
& [protein_{Cy3/Cy5}] \tag{5} \\
& = \frac{A_{280} - ((A_{Cy3,max} - (A_{Cy5,max} \times CF_{Cy5,555})) \times CF_{Cy3,280}) - (A_{Cy5,max} \times CF_{Cy5,280})}{\epsilon_{protein}}
\end{aligned}$$

where $CF_{Cy3,555} = 0.08$ is the correction factor for the absorbance of Cy5 around the Cy3 peak.

The subunit labeling yield of Cy3 in the presence of Cy5, $P_{Cy3: Cy5}$, is calculated as:

$$P_{Cy3/Cy5} = \frac{(A_{Cy3,max} - (A_{Cy5,max} \times CF_{Cy5,555}))}{[protein_{Cy3/Cy5}] \times \epsilon_{Cy3}} \tag{6}$$

and the subunit labeling yield of Cy5 in the presence of Cy3, $P_{Cy5: Cy3}$, is calculated as:

$$P_{Cy5/Cy3} = \frac{A_{Cy5,max}}{[protein_{Cy3/Cy5}] \times \epsilon_{Cy5}} \tag{7}$$

2.5 Lipid Preparation

Lipid micelles dissolved in detergent were prepared following the established protocols (2). *E. coli* polar lipid extract (EPL, Avanti Polar Lipids Inc., Alabaster, AL) in chloroform (25 mg/mL stock) was placed in a glass vial. For 2:1 POPE/POPG, 1-palmitoyl-2-oleoyl-sn-glycero-3-phosphoethanolamine (POPE, Avanti Polar Lipids Inc., Alabaster, AL) and 1-palmitoyl-2-oleoyl-sn-glycero-3-phospho-(1'-rac-glycerol) (POPG, Avanti Polar Lipids Inc., Alabaster, AL) in 25 mg/mL chloroform were mixed at ratio of 2 POPE to 1 POPG (v/v) in a glass vial. The chloroform

was dried by evaporating it using a continuous flow of 0.22 μm filtered Ultra High Purity N_2 gas (Airgas). Next, the lipids were rinsed with pentane (Sigma-Aldrich) and subsequently dried by rotating the vial under N_2 gas for approximately 10-12 minutes. This process resulted in a thin lipid film on the inner walls and the bottom of the vial. After repeating the washing step 2-3 times, the lipid film was resuspended in DB with 35 mM of CHAPS (Anatrace) to make final concentration of 20 mg/mL lipid. The lipid/detergent mixture was desolved by using a cup-horn sonicator (Qsonica, Newtown, CT) until the sample has see-through appearance.

2.6 Reconstitution of CLC-ec1 into Liposome

The reconstitution was carried out based on the method introduced in the previously literature (1, 2). The protein in detergent was added into the lipid-detergent mixture from the lipid preparation. The mixed solution was transferred into dialysis cassettes (Thermo Fisher Scientific) with a molecular weight cutoff of 10,000. Subsequently, the samples were dialyzed in a dark environment at 4 $^{\circ}\text{C}$, using 4 liters of DB. Buffer changes were done every 8-12 hours, with a total of 4 buffer changes during the process. After the dialysis, the samples were collected from the dialysis cassettes followed by three freeze-thaw cycles with -80 $^{\circ}\text{C}$ freezer to create large pauci-lamellar vesicles (LVs). At -80 $^{\circ}\text{C}$, the samples were frozen for 10 minutes, and the samples were taken out and thawed for 15 minutes at room temperature in dark.

2.7 Bulk FRET Method of CLC-ec1 Subunit-Exchange

Bulk FRET experiments were carried out as introduced previously (2). FRET was measured for fused or co-labeled proteoliposomes in the Pauci-lamellar vesicles (PLV) state

containing 1 $\mu\text{g}/\text{mg}$, $\chi = 10^{-5}$ subunits/lipid. Samples were excited at 550 nm and emission spectra was collected from 560 – 740 nm, with a 4 nm slit width, 0.05 s integration time. From the fluorescence emission spectra, the maximum intensity for Cy3 and Cy5 were found, and the ratiometric FRET signal was calculated as follows:

$$FRET\ signal = \frac{I_{Cy5,max}}{I_{Cy3,max} + I_{Cy5,max}} \quad (9)$$

2.8 Subunit Capture Single Molecule Photobleaching Measurement of CLC-ec1

Subunit capture single molecule photobleaching experiment follows the method introduced previously (1, 2, 5). In this measurement, images were collected with an objective based total internal reflection microscope (TIRF) built by Robertson Laboratory (2). For Cy5 imaging, 637 nm OBIS laser (Coherent, Santa Clara) was used to excite the Cy5 fluorophores labeled on the CLC-ec1. The laser power was adjusted to $\sim 100\ \mu\text{W}$ using a half-wave plate on the excitation path to obtain optimal S/N ratio with long photobleaching traces. Next, coverslips (25 x 25 mm, 1.0 mm thickness, Thermo Fisher Scientific) and glass slides (Gold-Seal 24 x 60 mm, 1.5mm thickness, Thermo Fisher Scientific) were washed with 0.1% Micro-90 detergent (Cole-Parmer) for 30 minutes followed by sonication for 30 minutes. After the sonication, the slides were rinsed 5 times with MilliQ water. Then, they were washed with 100% ethanol (Thermo Fisher Scientific) followed by sonication for 30 minutes. After the sonication, they were rinsed 5 times with MilliQ water. Finally, the slides went through sonication for 5 minutes in the 0.2 M KOH (Sigma-Aldrich) solution followed by rinsing with MilliQ water 5 times. Once the coverslips and the glass slides were completely cleaned and washed, silicon grease (Dow Corning, Midland, MI) was applied to

the coverslip and glass slides to create the flow channels for imaging. After loading the glass slides onto the objective lens of the microscope, 80 μL of sample were added into each chamber. We allowed ~ 3 minutes to make sure that liposomes have enough time to bind to the glass. Then, the flow channel was washed 3 times with 0.22 μm filtered DB to get rid of any proteoliposomes left unbound. The number of spots in each imaging field was ~ 100 spots by diluting it with DB. For imaging, samples were extruded through a 400 nm polycarbonate membrane (Whatman, Maidstone, UK) using LiposoFast-Basic extruder (Avestin, Ottawa, ON) 21 times. All single molecule photobleaching experiments were carried out in the DB solution.

After the photobleaching experiment, the analysis was done with the methods described previously (2, 5). Data files were analyzed through the MATLAB-based software (6). In the analysis software, Cy5 fluorescent spots were selected with a 4 x 4 pixel area of interest (AOI). The cumulative pixel brightness within each region of interest (AOI) was measured over time, and it was used to count the photobleaching steps from intensity decrease due to the photobleaching of fluorophores.

2.9 Calculation of F_{Dimer} and ΔG°

To calculate the value of F_{Dimer} of CLC-ec1 from photobleaching analysis, we use a method described previously (1, 2). F_{Dimer} is defined as dimer/lipid mole fraction (χ_D^*) divided by total reactive mole fraction (χ^*) equivalent to $\chi/2$ since the reaction only occurs between same oriented subunits:

$$F_{Dimer} = \frac{2\chi_D^*}{\chi^*} \quad (10)$$

Probabilities of experimental ideal constitutive monomers ($P_{n=1-3+}^M$) from I201W/I422W (5, 7), and ideal constitutive dimers ($P_{n=1-3+}^D$) from R230C/L249C (5, 8) are used to fit the experimental photobleaching data (P_n^{expt}). Least-squares analysis is performed from the sum of squared residuals (R^2) with the experimental data (P_n^{expt}) and a linear combination of $P_{n=1-3+}^M$ and $P_{n=1-3+}^D$ weighted by

$$R^2 = \sum_{n=1-3+} (P_n^{expt} - ((1 - F_{Dimer}) \cdot P_n^M + F_{Dimer} \cdot P_n^D))^2 \quad (11)$$

The minimum R^2 value is used to predict the best-fit of F_{Dimer} from the photobleaching experiment data. Finally, the equilibrium constant is calculated from the mole fractions of dimers and monomers. The equilibrium dimerization reaction can be written as follows for monomers (M) and dimers (D):



The dimerization equilibrium constant (K_{χ^*}) can be calculated from the mole fraction (χ^*):

$$K_{\chi^*} = \frac{\chi_D^*}{(\chi_M^*)^2} \quad (13)$$

where χ_M^* the monomer/lipid mole fraction, and K_{χ^*} the dimerization equilibrium constant in inverse mole fraction units. The total mole fraction of subunits in the membrane is:

$$\chi^* = \chi_M^* + 2\chi_D^* \quad (14)$$

The fraction of dimeric state (F_{Dimer}) is derived by substituting the total mole fraction of subunits to dimerization equilibrium expression to determine χ_D^* , and F_{Dimer} vs. χ^* was fit to the equilibrium dimerization:

$$F_{Dimer} = \frac{1 + 4\chi^*K_{\chi^*} - \sqrt{1 + 8\chi^*K_{\chi^*}}}{4\chi^*K_{\chi^*}} \quad (15)$$

From this, we can determine the equilibrium constant (K_{χ^*}) leading to the free energy of membrane protein dimerization:

$$\Delta G^\circ = -RT\ln(K_{\chi^*}) \quad (16)$$

2.10 Measurement of CLC-ec1 Function

Chloride transport function was measured as described previously (1, 2, 9). First, proteins were reconstituted into lipids at 1 $\mu\text{g}/\text{mg}$ corresponding to a $\chi_{\text{reconstituted}} = 1.4 \times 10^{-5}$ subunit/lipid. Freeze-thawed samples were extruded through a 400 nm polycarbonate membrane (Whatman, Maidstone, UK) using LiposoFast-Basic extruder (Avestin) for 21 times. To measure the chloride transport function in the chamber, DB in the proteoliposome sample was replaced with the EB using a G50 Sephadex column (GE Life Sciences). The chloride transport function was measured using a potentiometer which is a chloride sensing electrode (Cole-Parmer, Vernon Hills, IL). To begin with, 3.8 mL of external buffer (1 mM KCl, 150 mM K_2SO_4 , 20 mM Citrate pH 4.5 with NaOH) was added to the measurement beaker for the recording, followed by 15 μL of 10 mM KCl for calibration of the signal. Then, proteoliposomes (100 μL of extruded sample \sim 200 μL) in EB

were added into the measurement beaker. By adding KCl into the beaker, the concentration of Cl⁻ becomes higher on the inside of the membrane, forming a Cl⁻ concentration gradient, and thus Cl⁻ ions will start to flow outside. However, as soon as the first Cl⁻ ion moves out, it creates electrical imbalance and acts against the chemical gradient of Cl⁻ ion which makes chloride ion export energetically unfavorable. Ion transport was directly initiated by adding 5 μL of 1 mM K⁺ ionophore valinomycin (Sigma-Aldrich) and 2 mM of protonophore FCCP (Sigma-Aldrich). Valinomycin and FCCP allow potassium ions and protons to flow outside, therefore dissipating the electrical imbalance and setting the potential to zero and Cl⁻ ions will start to flow again. After the initial Cl⁻ transport is finished, 50 μL of 1.5 M n-Octyl-β-D-Glucopyranoside (β-OG, Anatrace) detergent was added at the end of the transport to break all the liposomes and count the number of inactive liposomes. From the chloride efflux measurement, the traces were normalized to total [Cl⁻], then fit to a two-component exponential relaxation function to obtain k_{CLC} , k_{leak} and F_0 as follows:

$$Normalized [Cl^-]_{ext} = (1 - F_0)(1 - e^{-(k_{CLC}+k_{leak})t}) + (F_0)(1 - e^{-k_{leak}t}) \quad (8)$$

For the fitting, the k_{leak} value was set to be 0.0008 rel. Cl⁻/ sec from the result on the previous measurement done with 2:1 POPE/POPG liposomes (2).

2.11 Preparing CLC-ec1 and Lipid Bilayer for Coarse-Grained Molecular Dynamics Simulations

Preparation of CLC-ec1 and lipid bilayer for coarse-grained molecular simulations (MD) follows the procedures previously introduced by Ozturk & Bernhardt et al. (10). To briefly explain, the crystal structure of WT CLC-ec1 dimer (1OTS in PDB) (11) was used to convert the structure

into the coarse-grained representation with a Martinize script (12). In this system, E113 is protonated in both subunits and D417 is protonated only in one subunit (13). The lower and upper cutoff distances for the elastic network are set to 0.5 nm and 0.9 nm, respectively. The force constant for elastic bonds is 500 kJ/mole/nm². This elastic network was created independently for each protomer, devoid of any inter-subunit elastic bonds. The CLC-ec1 dimer, derived from the crystal structure (1OTS in PDB), was oriented in a manner where its dimerization interface is perpendicular to the *x*-axis, while the transmembrane segment aligns parallel to the *z*-axis. Then, the coarse-grained protein structure was embedded into a coarse-grained lipid bilayer by INSANE (INSert membrANE) script to embed CLC-ec1 proteins into the center of lipid bilayer and build coarse-grained simulation systems containing a pure 1-palmitoyl-2-oleoyl-sn-glycero-3-phosphocholine (POPC) lipid bilayer including 0.15 M NaCl and water (90% regular and 10% antifreeze water) with a box size of 25 nm × 15 nm × 10 nm (14). Next, Martini 2.0 force field parameters were applied to measure the interactions of coarse-grained beads in the system (15), and the system was energy-minimized followed by equilibration with the steps introduced previously (16). The initial minimization step was required to remove the initial steric clashes within the systems using a soft-core potential. This step was followed by another minimization using the regular 12-6 Lennard-Jones potential. Initial equilibration was done while restraining the positions of the protein's backbone beads using a harmonic potential with a force constant of 1000 kJ/mole/nm² for 10 ps, followed by 500 kJ/mole/nm² for 3 ns since increasing the number of minimization steps might result in large gaps between the protein and lipid beads, as lipid molecules tend to attract each other more rapidly than the proteins do. The time step was continuously increased from 2 fs to 20 fs. The pressure and temperature were set to 1 bar and 310 K by utilizing the semi-isotropic Berendsen barostat (17) with the velocity-rescaling algorithm

(18). Once all the steps are completed, 20 μ s-long coarse-grained MD simulations were run using GROMACS (2021.5). In the production step, the system was switched to the Parinello-Rahman barostat (19) which was suggested by de Jong et al. (16). A set of collective variables was applied to maintain the central position of both CLC-ec1 protomers within the simulation box. It also restrains the dimerization interface of one protomer with respect to the other protomer and the inter-subunit separation between the two CLC-ec1 protomers. The Plumed 2 software was used to apply harmonic restraints on these collective variables, with a force constant of 2000 kJ/mole/nm² (20). In order to maintain the protomers at the center of the simulation box, the geometric center was calculated based on the collective variables G_1 and G_2 . The coordinates in the x and z dimensions for this center were restrained using harmonic potentials with a force constant of 2000 kJ/mole/nm². Finally, the inter-subunit distance was determined by establishing a distance vector from the geometric center of G_1 and G_2 collective variables of one protomer to that of the other protomer.

References

1. K. N. Mersch (2021) Protein Determinants of CLC-ec1 Stoichiometry. (The University of Iowa, United States -- Iowa), p 204.
2. R. Chadda *et al.*, The dimerization equilibrium of a ClC Cl(-)/H(+) antiporter in lipid bilayers. *Elife* **5** (2016).
3. A. Accardi, L. Kolmakova-Partensky, C. Williams, C. Miller, Ionic currents mediated by a prokaryotic homologue of CLC Cl⁻ channels. *J Gen Physiol* **123**, 109-119 (2004).
4. M. Maduke, D. J. Pheasant, C. Miller, High-level expression, functional reconstitution, and quaternary structure of a prokaryotic ClC-type chloride channel. *J Gen Physiol* **114**, 713-722 (1999).
5. R. Chadda, L. Cliff, M. Brimberry, J. L. Robertson, A model-free method for measuring dimerization free energies of CLC-ec1 in lipid bilayers. *J Gen Physiol* **150**, 355-365 (2018).
6. L. J. Friedman, J. Gelles, Multi-wavelength single-molecule fluorescence analysis of transcription mechanisms. *Methods* **86**, 27-36 (2015).
7. J. L. Robertson, L. Kolmakova-Partensky, C. Miller, Design, function and structure of a monomeric ClC transporter. *Nature* **468**, 844-847 (2010).
8. W. Nguitragool, C. Miller, CLC Cl⁻/H⁺ transporters constrained by covalent cross-linking. *Proc Natl Acad Sci U S A* **104**, 20659-20665 (2007).
9. M. Walden *et al.*, Uncoupling and turnover in a Cl⁻/H⁺ exchange transporter. *J Gen Physiol* **129**, 317-329 (2007).
10. T. N. Ozturk *et al.*, Mitigation of membrane morphology defects explain stability and orientational specificity of CLC dimers. *bioRxiv* 10.1101/2023.03.16.533024, 2023.2003.2016.533024 (2023).
11. R. Dutzler, E. B. Campbell, R. MacKinnon, Gating the selectivity filter in ClC chloride channels. *Science* **300**, 108-112 (2003).
12. D. H. de Jong *et al.*, Improved Parameters for the Martini Coarse-Grained Protein Force Field. *J Chem Theory Comput* **9**, 687-697 (2013).
13. J. D. Faraldo-Gomez, B. Roux, Electrostatics of ion stabilization in a ClC chloride channel homologue from *Escherichia coli*. *Journal of Molecular Biology* **339**, 981-1000 (2004).

14. T. A. Wassenaar, H. I. Ingolfsson, R. A. Bockmann, D. P. Tieleman, S. J. Marrink, Computational Lipidomics with insane: A Versatile Tool for Generating Custom Membranes for Molecular Simulations. *J Chem Theory Comput* **11**, 2144-2155 (2015).
15. S. J. Marrink, H. J. Risselada, S. Yefimov, D. P. Tieleman, A. H. de Vries, The MARTINI force field: coarse grained model for biomolecular simulations. *J Phys Chem B* **111**, 7812-7824 (2007).
16. D. H. de Jong, S. Baoukina, H. I. Ingolfsson, S. J. Marrink, Martini straight: Boosting performance using a shorter cutoff and GPUs. *Comput Phys Commun* **199**, 1-7 (2016).
17. H. J. C. Berendsen, J. P. M. Postma, W. F. Vangunsteren, A. Dinola, J. R. Haak, Molecular-Dynamics with Coupling to an External Bath. *J Chem Phys* **81**, 3684-3690 (1984).
18. G. Bussi, D. Donadio, M. Parrinello, Canonical sampling through velocity rescaling. *J Chem Phys* **126** (2007).
19. M. Parrinello, A. Rahman, Polymorphic Transitions in Single-Crystals - a New Molecular-Dynamics Method. *J Appl Phys* **52**, 7182-7190 (1981).
20. G. A. Tribello, M. Bonomi, D. Branduardi, C. Camilloni, G. Bussi, PLUMED 2: New feathers for an old bird. *Comput Phys Commun* **185**, 604-613 (2014).

Chapter 3: *The Lambda III*, Total Internal Reflection Fluorescent (TIRF) Microscope Alignment Tutorial

3.1 Preface to the Chapter

I wrote a protocol for the *Lambda III* total internal reflection fluorescence (TIRF) microscope, which is a microscope that can be used for single-molecule imaging. It is an open laser microscope that is fully customizable and follows the co-localization single molecule spectroscopy (CoSMoS) design first implemented by the Gelles Laboratory at Brandeis University (1). This microscope has several advantages, including two excitation arrangements, a micro-mirror path for TIRF and highly inclined and laminated optical sheet (HILO) microscopy, allowing the laser light to be directed at a sharp angle through the sample. The emission can be detected in four wavelength channels for simultaneous quad-viewing capabilities. In addition, the emission can be detected by two separate detectors, and electron multiplying charge-coupled device (EMCCD) (Andor, iXon3 X-8623) or complementary metal-oxide-semiconductor (CMOS). There is already a guide to building this TIRF microscope published previously (2), but the protocols introduced in the paper does not provide enough amount of information for the alignment of the microscope. Therefore, I provide a tutorial document for alignment in this chapter of my thesis, so that anyone who builds a *Lambda III* TIRF microscope can easily align the microscope.

3.2 Abstract

Lambda III total internal reflection fluorescence (TIRF) microscope has solved a lot of challenges in studying protein folding, oligomerization, and kinetics of protein complexes by providing clear images with low background signals using evanescent waves. Here I describe an alignment protocol for building a *Lambda III* TIRF microscope using micromirrors. The alignment of this type of scientific microscope requires a significant time investment, therefore it is necessary to have straightforward protocols so that people can follow the protocols step by step to build the microscope. In my protocol, I have arranged the alignment process thoroughly from the alignment of the excitation and emission paths of the microscope for multi-color imaging to the exiting path from the micromirror. I also explain how to work with lasers and a micrometer slide ruler. All of these are necessary components when aligning the optical setups in the *Lambda III* microscope. This protocol will help users construct the *Lambda III* TIRF and save time when aligning the microscope by speeding up the alignment procedures by 1 month.

3.3 Introduction

Understanding the physical driving force of folding and oligomer formation in membrane proteins within the membrane has been challenging in the membrane protein field due to limitations in the experimental methods in purification and observation (3, 4). One of the methods for investigating the oligomerization of membrane proteins is single molecule imaging technique using TIRF microscopy (5). The TIRF microscope has an objective lens-based setup where an evanescent field is generated by Total Internal Reflection (TIR). The TIRF microscope detects samples in an induced evanescent field by selectively exciting the fluorescently labeled proteins

attached to the glass surface providing the high signal to noise ratio (SNR) on the image of individual fluorophores. In this protocol, we focus on the alignment of a multi-color TIRF microscope containing 488nm, 532nm, 637nm, and Infrared (IR) lasers for single-molecule experiments. The first content is about the alignment of the excitation pathway. The excitation pathway is the most important part as it is the part where the collimated beam is located, and the proper size beam is made for the single molecule imaging. It will cover the different components for changing the size of the beam, producing a collimated beam, and attenuating the beam power in the excitation pathways. The second content of the protocol is about the alignment of the beam to the platform. The purpose of this content is to ensure that laser light coming into the platform is parallel to the ground for a precise and uniform excitation to the sample. The third content explains the alignment of the excitation micromirror. This content is about aligning the micromirror that receives the incoming excitation light for total internal reflection at the slide/sample interface, so it reflects the light at 90° upwards relative to the optical table. The fourth content describes the adjustment of the exiting micromirror. The main objective of this alignment section is to remove the exiting light from TIR and direct the light out of the emission path so that background noise is not created in our image. The fifth content is about positioning L_1 & L_2 lenses. The objective of this content is to locate the lenses at the right distance to get the precise focus of the emission iris. The sixth content in the protocol describes the alignment of emission path. The objective here is to align the light in the emission path. The emission light that is reflected from the sample should go through the emission path and directed to CCD if the emission alignment allows the emitted light from the sample to be centered on the emission field for imaging. The seventh content of the protocol will be about the alignment for multi-color imaging. This allows us to conduct multi-wavelength TIRF imaging using three distinct fluorophores Cy3, Cy5, and GFP in different

wavelength ranges. The eighth content of the protocol provides a guide the user on how to adjust the laser power with a half-wave plate in the excitation path. Finally, the last content explains how to use a scale bar for microscope imaging and analysis.

3.4 Procedure

3.4.1 Alignment of the excitation pathway

The laser light must be aligned such that it is parallel to the optical table. The excitation pathway includes several components for changing the size of the beam, producing a collimated beam, and attenuating the beam power.

1. **Clear the path for the incoming excitation beam.** Remove the rail in the excitation path and introduce a 5X objective lens in the light path.
2. **Setting up the iris in front of the objective lens.** Use an iris in front of the objective to make sure that the laser beam is centered and is hitting the wall without being blocked by optics.
3. **Placement of cage rods.** Add cage rods and make sure they are level using a post-holder tool so that the height of cage rods can be compared with adjacent lasers.
4. **Placement of the optical components into cage rods.** Insert pinhole, the second lens of a beam expander, and half waveplate into an assembly.
5. **Adjustment of the pinhole position.** Center the position of the pinhole by measuring light transmittance, and the shape of the beams. T-shirt shaped anodized aluminum drop-in alignment targets can be used to make sure the beam is traveling along the center of the rods. Once the best position is found, tighten the screw of the pinhole.

6. **Introduction of the final dichroic mirror.** Place the final dichroic mirror and check if the mirror is at the right height using the post-holder tool to make sure that the beam is hitting the dichroic mirror at a 45° angle.

7. **Determination of the second lens of the beam expander position.** Make sure the beam is collimated by following the diameter over the longest distance possible. Once the position where the beam is collimated is located, fix the second lens position by tightening the screw.

8. **Setting up a quarter waveplate and beam splitter into the path.** Insert a variable attenuator and a quarter waveplate in the path.

9. **Final beam alignment with two irises.** Place two irises between the dichroic mirror (**Fig. 1-①**, **②**, **③**, **④**) and broad band mirror (**Fig. 1-⑤**). After setting up the irises, adjust the dichroic mirror (**Fig. 1-①**, **②**, **③**, **④**). Finally, make sure that the beam is going through the center of the target.

3.4.2 Alignment of the excitation beam onto a platform

Typically, the excitation beam alignment is carried out at the beginning when building the microscope. However, from time to time, one will want to check that the light coming into the micro-mirrors is parallel. The objective here is to ensure that the excitation laser light is coming into the platform parallel. To do this, one will need to move all optics out of the beam path and align the laser with a fiducial marker on the wall, or the ruler tool which specifies the correct height of the beam.

1. **Clear the path for the incoming excitation beam.** Translate the incoming and exiting micromirrors using the screw on the manipulator so that micromirrors are out of the beam path.

Be careful and watch the micromirrors while doing this so that nothing is inadvertently bumped. The goal here is to provide access so that the beam can directly go to the target.

2. Removal of final focusing lens. Remove the final focusing lens. The iris should be in the path so that the beam size can be adjusted.

3. Removal of the quadrupole detector (QPD) module. Remove the QPD module. It can be swung out of the way when detached from the platform. The purpose of this is to provide access to the target.

4. Checking the beam on the excitation iris. Open the excitation iris, and check if the beam is hitting the center of iris. If the beam is not hitting the center of the iris, adjust the dichroic mirror (DM) (**Fig. 1-** ② or ③ or ④) in the excitation side and place it to hit the center of iris. (Test with all colors 488, 532 and 637nm individually) * *Do not try to adjust the beam with the broadband (BB) mirror (Fig. 1-⑤) since it shares the path with all the lasers for excitation.*

5. Confirming the position of the beam. Check if the beam is hitting the target on the wall. Alternatively, the ruler tool can be used on the table to ensure that the beam is parallel at several positions along the table.

6. Final alignment with a final focusing lens. Insert the final focusing (FF) lens. Adjust the X and Y manipulator screws of the excitation lens to align the beam on the target of the wall.

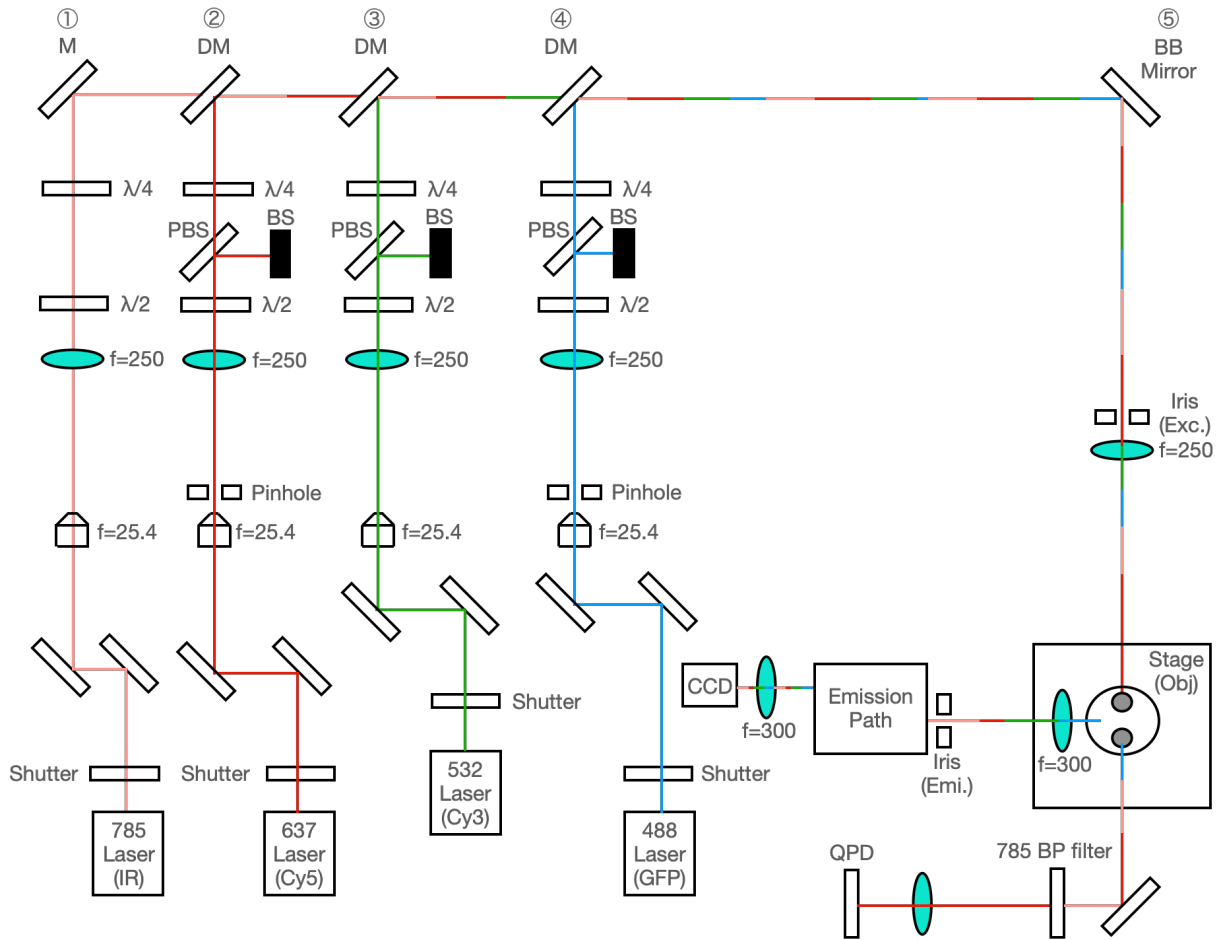


Figure 1. Schematic view of the optical setup for excitation path of micromirror TIRF microscope. A general component of an objective lens based micromirror TIRF microscope. Each laser beam (shown as pink, red, green, and blue solid lines) can be combined using a long pass dichroic mirror (②, ③, ④) and broadband mirror (⑤), dichroic mirrors can select and transmit a specific range of wavelength. Each beam is expanded and collimated when the beam is going through the Keplerian beam expander in the excitation path (Objective lens $f = 25.4$ mm, lens $f = 250$ mm). These lenses are chosen based on the diameter of the input beam and output beam. The beam intensity is adjusted by an attenuator composed of a $\lambda/2$ waveplate in the excitation path and a polarizing beam-splitting cube. Also, a $\lambda/4$ waveplate is for circular polarization of the incoming beam. The individual incoming beams go through a corresponding band-pass filter. Iris before the excitation to the sample is used to adjust the beam diameter for excitation. Finally, combined beams are reflected by the excitation micromirror for excitation to the sample.

3.4.3 Alignment of the excitation micromirror

The objective here is to align the micromirror that receives the incoming excitation light for TIR at the slide/sample interface so that it reflects the light at 90° upwards relative to the optical table. ** Note, the incoming laser light, including the final focusing (FF) lens should have already been aligned parallel to the table as described in the previous section.*

1. Clear the path for the incoming excitation beam. Remove the final focusing lens and iris and take out the lens and put the iris part again to adjust the size of the beam while aligning micromirrors. The purpose of this is to ensure that the light is coming through straight and is not perturbed by the final focusing (FF) lens. This makes the initial alignment easier, and the lens will be added back later.

2. Initial placement of excitation micromirror. Set up the excitation micromirror using a tweezer in a visually aligned position so that the angled mirror is facing the incoming beam. Be careful not to touch the mirrored coating with the tweezers. Also, make sure that the mirror magnet is seated properly on the metal ledge. Since the entire holder is metal, it is possible for the magnet to adhere at an improper angle. Gently nudge the mirror to check that it is stable. Check the mirror from the side to see that it is properly seated and angled. ** Visually inspect the micro-mirror from the top and the side. Here, it is necessary to confirm that the mirror is seated properly and appears visually aligned at a right angle. This will put the user in a good position for the rest of the alignment.*

3. Centering the beam on the mirror. Adjust the mirror with the three translation axes on the manipulator so that the beam hits the center of the mirror. The iris is used to reduce the beam size.

There should not be any scattering of transmitted light because that means the beam is leaking and not hitting the center of the mirror.

4. Aligning the beam on the target by mirror rotation. Now, the mirror angle must be adjusted to align the beam with the objective alignment tool. There are two ranges of motion here. Rotation of the mirror about its vertical axis, and rotation of the arm that the mirror sits on. First, rotate the mirror (**Fig. 2**). Using forceps, grab the sides of the micromirror and rotate it to bring the beam to the center of the bottom of the alignment tool. The beam position can be aligned along the x-axis by rotating the micromirror about the z-axis. If the beam is not hitting the center of the alignment tool on the bottom, use y-positioner to bring it to center, and check the target on the top of the alignment tool. Try to bring the beam to the center on the target on both the top and the bottom of the alignment tool as close as possible.

5. Aligning the beam on the target by mirror tilt. Once the beam is brought as close to center as possible, try to adjust the beam by tilting the micromirror (loosening the screw at the bottom). Once the beam hits the target, check it with the objective holder alignment tool (Try not to tighten it too much) and see if the light is hitting the center at the bottom and the top. ** The user will need to iterate through steps 4 and 5 to obtain alignment onto the target.*

6. Centering the beam on the mirror. Try to move the micromirror plate holder along the x and y axis using the micromirror positioner (**Fig. 2**). The alignment of the beam should not change with these movements.

7. Introducing the excitation final focusing (FF) lens. Once the laser is hitting the center of the target on the ceiling, put the excitation final focusing lens and the iris part back.

8. Centering the beam on the mirror. It is possible that reintroducing the lens moves the spot on the mirror. It is important to re-confirm that the beam is centered on the mirror, and that there is

no scattering of excitation light. Adjust the translation axes so that the mirror is centered. ** At this point, the lens should not be perturbed. If the lens was perturbed, then it may be off-axis; if that is the case, go back to the section “Alignment of the excitement beam onto a platform” for beam alignment.*

9. Introducing objective lens and sample holder. Screw in the objective and load multi-color fluorescent bead samples into the slide, being careful not to change the settings on the collar.

10. Adjusting the z-position of the final focusing lens. Move it back and forth along the rail until the tightest spot of the emerging beam is achieved. (If the emerging beam from the objective lens doesn't hit the ceiling at the desired spot, then some fine adjustment can be done by x-y translation on the final focusing lens)

11. Fixing the final focusing lens at the right distance. Once a good position is found, fix the final focusing lens.

12. Getting TIRF image by changing the position of micromirror. Turn on the camera and laser. (Change the readout rate to 10MHz at 14-bit, EM gain to 7) and change the position along the y-direction of the micromirror so that the TIRF angle is obtained by moving the screw of the micromirror while checking the image on the camera. Try to move the laser to the wall further until you get the TIRF image.

13. Confirming TIRF with single molecule measurement. Load single molecule samples into another lane and check the image with a single molecule sample. (Change Readout Rate to 1MHz at 16-bit, and Electron Multiplier Gain Level to 300). ** It is important to check that the field of view doesn't translate when going from TIRF to Epi.*

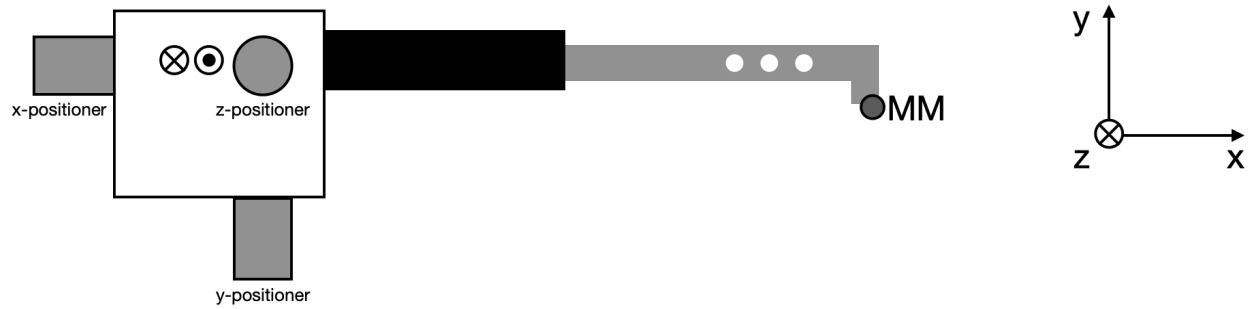


Figure 2. Schematic view of an excitation micro-mirror positioner. Micromirror receives the incoming excitation beam for total internal reflection at the sample. The excitation micromirror reflects the light at 90° upwards relative to the optical table. Excitation micro-mirror positioner helps to adjust the position of the micromirror in an x, y, and z direction. If the beam is not hitting the center of the target, x, and y positioners are used to bring the beam to the center. Once the beam is brought to the center as close as possible, the beam can be adjusted by tilting the micromirror by loosening the screw at the bottom. Finally, the beam should be centered on the mirror and the excitation final focusing (FF) lens. It is important to re-confirm that the beam is centered on the mirror after bringing all the optical components back to the setup and that there is no scattering of excitation light.

Table 1. Summary of the beam movement based on the alignment on the excitation micromirror. The table shows how the beam moves on the target based on the translational and the rotational movement using the micro-mirror positioner. The x and z positioner movements do not change the location of the beam, but the y positioner movement allows the beam position to move along the y-axis. Rotation of the micromirror about the z-axis using the tweezers will move the beam position along the x-axis. Rotation of the micromirror using the micromirror positioner arm will let the beam move along the y-axis.

Alignment	Movement of beam	On the target
x-positioner adjustment	No change	<p>Beam spot on the target of the ceiling</p>
y-positioner adjustment	↕	
z-positioner adjustment	No change	
Rotation of micromirror about the z-axis	↔	
Rotation of micromirror about the x-axis (Rotation of the arm)	↕	

3.4.4 Adjusting the exiting micromirrors

The main objective here is to remove the exiting light from TIR and direct it out of the emission path so that it does not include any background signals in our image. As a bonus, this light can be used for autofocusing. ** It is safer to align this with a regular laser line like 637 nm instead of the IR.*

1. Initial placement of exiting micromirror from the bottom. Once the excitation micromirror is in the right position for the TIRF imaging, set up the exiting micromirror using a tweezer from the bottom. The reason to set up the exiting micromirror from the bottom is to avoid removing the objective lens and sample slide since they have been correctly focused.

2. **Removal of QPD module.** Unscrew and remove the QPD module. It can be swung out of the way when detached from the platform. The purpose of this is to provide access to the target on the wall.
3. **Aligning the beam on the target by mirror tilt.** Check if the beam is hitting the target on the wall. If not, rotate the exiting micromirror with a tweezer from the bottom to bring the beam to the center of the target.
4. **Bringing the QPD module back to the setup.** Once the beam is hitting the center, bring the QPD path back and attach the parts to the setup.
5. **Beam alignment on the QPD sensor with 637nm laser.** Take a 785 nm bandpass filter out (**Fig 3 - ①**) so that 637 nm wavelength laser beam can be used to adjust QPD. ** The user will need to adjust the QPD with 637 nm (or 488, 532 nm) laser first. Since the IR laser is invisible, it is dangerous to use it when it is not aligned yet.*
6. **Beam alignment on QPD sensor with 637nm laser by mirror adjustment.** Try to bring x, y QPD values in the middle of the x and y axis (~ 5) by rotating the screws of the mirror in the QPD path. The reason for this step is to make the beam to hit the center of the QPD. ** It is important to do this process while the image is perfectly in focus.*
7. **Turning on the IR laser.** Once both x and y values are in the middle of QPD with a 637nm laser, turn on the IR laser, and insert 785nm again. Beam adjustment must be done with IR as a last step on the QPD since the IR laser will eventually be used for the TIRF lock.
8. **Beam alignment on the QPD sensor with IR laser.** Focus the image and see if QPD x, y value is at around 5. The reason for this step is to make the IR laser hit the center of the QPD.

9. Beam alignment on the QPD sensor with IR laser by mirror adjustment. If QPD x, y value is not around 5, use the screw of the mirror in the QPD path so that QPD values around 5 are achieved. * *This only requires small movement.*

10. Confirmation with TIRF-lock calibration. Calibrate and check if we are getting calibration (calibration along the y-axis) value $0.5 \mu\text{m/volt}$.

11. Adjusting the size of the excitation iris for the expected calibration value. If the calibration value is not around $0.5 \mu\text{m/volt}$, try to adjust the size of the excitation. (Size of the spot on QPD is important when calibrating)

12. Confirmation with TIRF-lock. Once the QPD is aligned with good focus, try to use the TIRF-lock value (k_p : 0.5, k_i : 0.008, Average 50) and change the field of view and check if the TIRF-lock works fine.

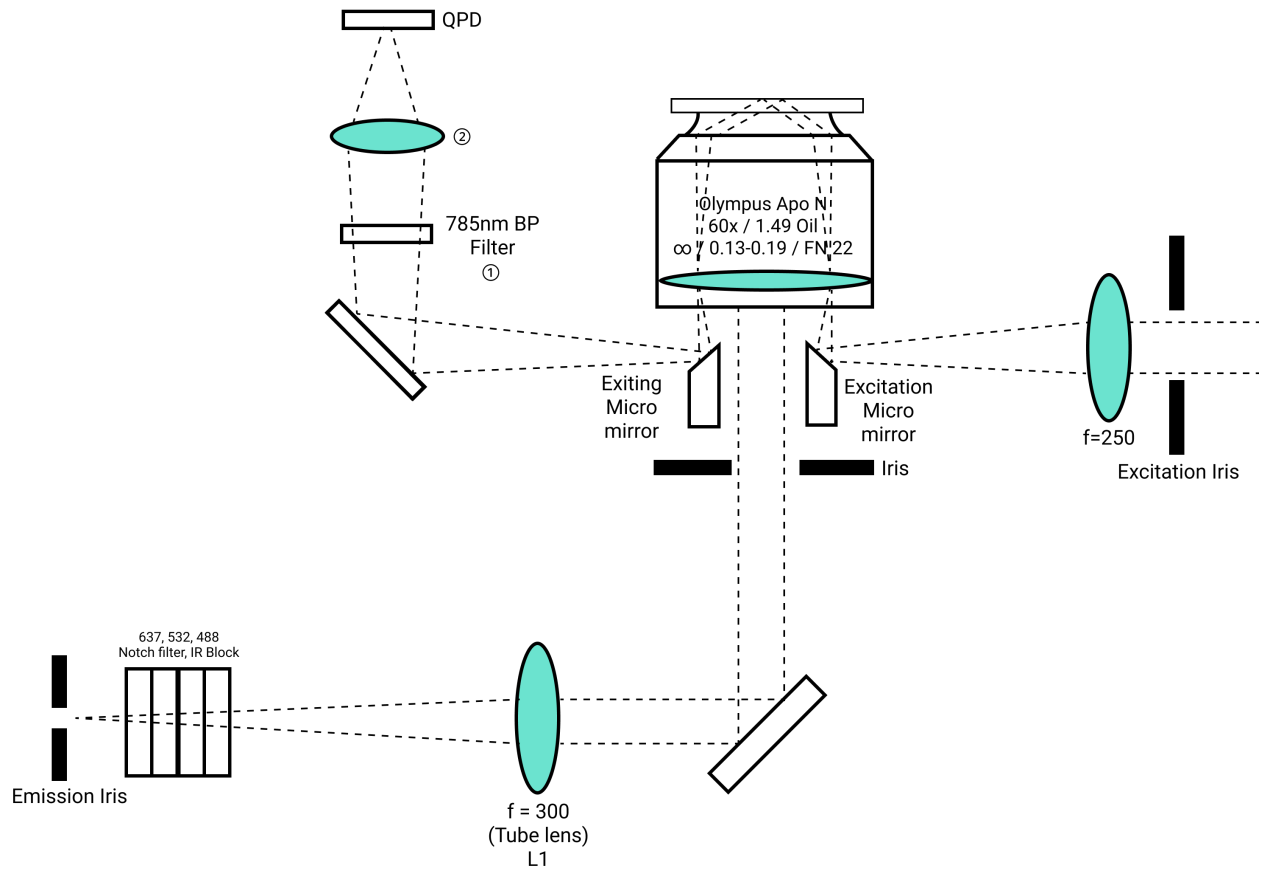


Figure 3. Schematic view of objective lens site. The excitation beam goes through the excitation iris and focusing lens ($f = 250$ mm), and it is reflected by the excitation micromirror to transmit the beam to the sample stage. The beam is reflected and bounced back by the exiting micromirror. The beam is filtered by a 785 nm band pass filter (①) so that only the IR laser beam can be transmitted. The beam is focused by the lens (②) in front of the QPD module and the signal is focused at the QPD panel for the alignment of the TIRF lock feature. On the other hand, the emission light from the sample is bounced by the broadband mirror and goes through the tube lens ($f = 300$ mm). Image is created at the emission iris after the beam is selected by multiple layers of 488 nm, 532 nm, and 637 nm IR block filters.

3.4.5 Positioning of L₁ & L₂ lenses in emission path

The main objective here is to position the lenses at the proper distance to get the right focus using the emission iris.

1. **Adjusting the lens distance at the focal length of the lens.** Try to adjust the distance between the lens (shown in **Fig 4-**①, ②, ③, ④) and the emission iris to be at the focal length of the lens (i.e. – 250mm) (shown in **Fig 4-**①, ②, ③, ④).
2. **Checking the focus of the lens with the edges of the emission iris.** Check with an image if the edge of the image looks sharp. * *The edges of the emission iris should be checked as an object using the light source.*
3. **Fixing the lenses at the right distance.** Once a sharp edge has been achieved, tighten the screw to fix the lenses at the distance found.

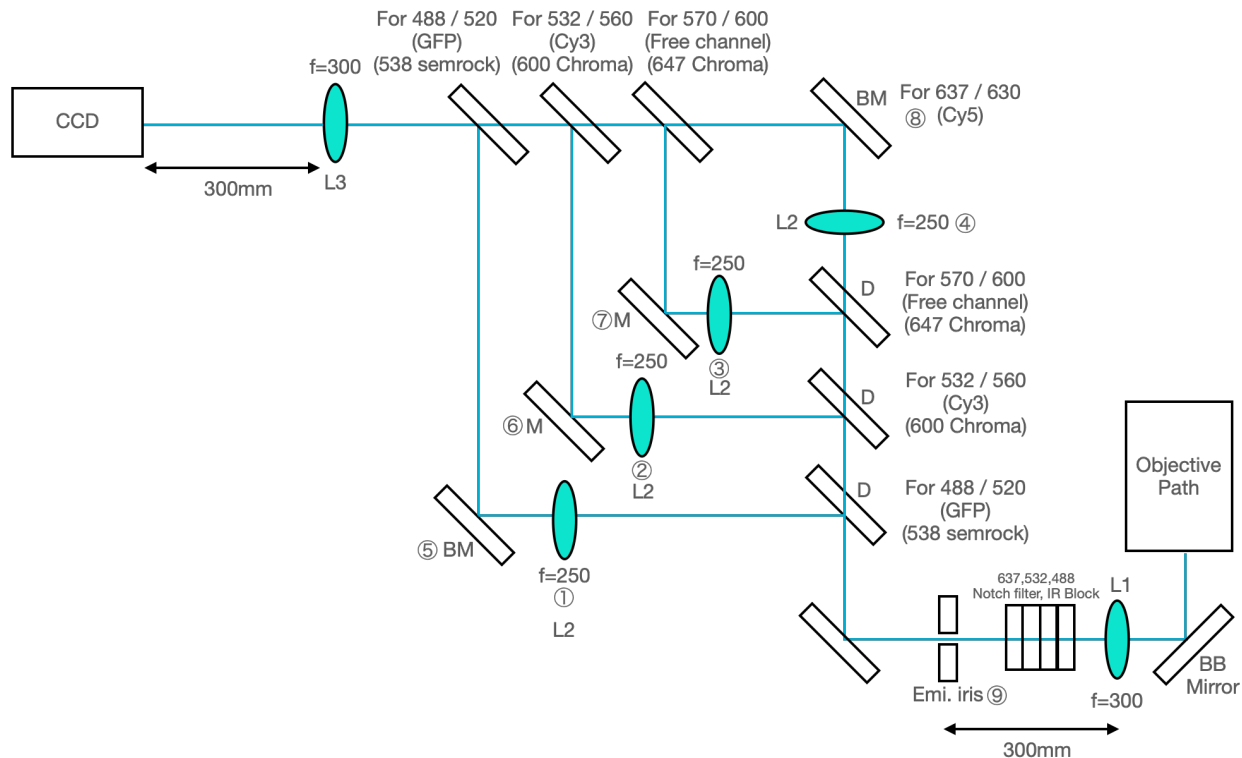


Figure 4. Schematic view of the optical setup for emission path of mmTIRF microscope. The beam exits the objective lens and is bounced by the broadband (BB) mirror below the objective lens and directed to the emission path. Multiple layers of the notch filter and IR blocker are set in the emission path to selectively and clearly transmit the emission light of 532 nm, 488 nm, and 637 nm to the CCD. The emission iris is set to adjust the size of the image field to the CCD. DM mirrors are set in the emission path for multi-color imaging (488/520 nm for GFP, 532/560 nm for Cy3, 570/600 nm, 637/630 nm for Cy5 imaging). Image is first created at the position where the emission iris is located, and it is passed through L₁ (f = 300 mm), L₂ (f = 250 mm), and L₃ (f = 300 mm) by expanding the size of the beam. Finally, a single molecule image is created at CCD using an L₃ lens.

3.4.6 Alignment for emission path

The objective here is to align the emission path. The emission light that is reflected from the sample goes through the emission path for imaging at CCD. If this alignment is done properly, both the excitation and the emission field should be perfectly aligned.

1. **Removal of CCD camera.** Mark the position where it was placed so that it can easily be mounted after alignment.
2. **Setting up the mirrors.** Set up two mirrors in the excitation path, Place one mirror between **Fig 1-④** and **Fig 1-⑤**, the other mirror in front of the L3 (f=300mm) lens (**Fig 5-⑨**) so that the light can go through the excitation path backward. (**Fig. 5**)
3. **Checking the height of the beam coming out from the mirror in front of the L3 lens.** Tilt the mirror in front of the L3 lens (**Fig. 5-⑨**) so that the beam can come toward the user and measure the height of the beam. If it is not at 4.5-inch height, align the height to 4.5-inch by using the screws of the mirror in front of the L3 lens (**Fig. 5-⑨**).
4. **Placement of two irises between the two mirrors.** Two irises should be placed between the two mirrors to align the beam going into the emission path.
5. **Adjusting the position of the mirrors.** Move the position of mirrors back and forth so that the beam is hitting the center of the two irises.
6. **Aligning the beam going into the emission path for the 637 nm channel.** Place a t-shirt shaped anodized aluminum drop-in alignment target right in front of the mirror (637/630) (**Fig. 5-⑧**), and change/tilt the position of the mirror in front of L3 lens (**Fig. 5-⑨**) to bring the beam to the center of the target, and place the target right before the emission iris and align the beam using the mirror (**Fig. 5-⑧**) * *Do not use the screw of the mirror in front of L3 lens (Fig. 5-⑨).*

7. **Emission path alignment for 488 nm channel.** Once the alignment is completed with the 637 nm laser, turn on the 532 nm laser and insert the 538 nm filter and use the screw of the mirror (**Fig. 5-⑤**) to align the path while checking the target right before the emission iris.
8. **Emission path alignment for 532 nm channel.** Replace a filter (for wavelength 538 nm) with a filter (for wavelength 600 nm) and use the screw of the mirror (**Fig. 5-⑥**) to align the path while checking the target right before the emission iris.
9. **Emission path alignment for a free channel.** Take out the filter (for wavelength 600 nm) and insert a filter (for wavelength 647 nm) and use the screw of the mirror (**Fig. 5-⑦**) to align the path while checking the target right before the emission iris.
10. **Checking the beam at the target on the ceiling.** Remove the 637, 532, and 488nm notch filter, IR blocker from the path, and check if the beam is coming out straight to the ceiling.

3.4.7 Alignment for multi-color imaging

The main objective here is to establish a system for multi-color imaging by adjusting the field of view for different colors.

1. Preparation for alignment with multi-color fluorescent beads. Change Readout Rate to 10MHz at 14-bit, and Electron Multiplier Gain Level to 7 and check Electron Multiplier Gain Enabled so that the light can be turned on while working. (Experiment setup -> Camera Setup -> Horizontal Pixel Shift -> Readout Rate) ** It is important to reduce the gain while turning on the light to prevent damage to the CCD camera.*

2. Introducing an objective lens and a sample holder. Set up a sample holder onto the objective lens and inject multi-color fluorescent beads into the lane.

3. Alignment of 637nm laser image field. Turn on the 637nm laser and adjust the size of the field using emission iris and excitation iris. Adjust the size of emission iris so that it can fit in the field (shown in **Fig. 6-①**) and make the excitation iris size slightly smaller than the emission iris. ** If the spots are not in focus, move the lens (shown in **Fig. 4-④**) slightly to bring it to focus. Once the 637 nm excitation path is aligned, move on to aligning the 532nm excitation path.*

4. Alignment of 532nm laser image field. Turn on the 532nm laser and bring the field to the position (shown in **Fig. 6-④**) by adjusting the mirror (shown in **Fig. 4-⑥**). ** If the spot is not in focus, move the lens (shown in **Fig. 4-②**) slightly back and forth to bring it to focus. Once the 532nm excitation path is aligned, move onto aligning the 488nm excitation path.*

5. Alignment of 488nm laser image field. Turn on the 488nm laser and bring the field to position (shown in **Fig. 6-②**) by adjusting the mirror (shown in **Fig. 4-⑤**). ** If the spots are not in focus,*

*move the lens (shown in **Fig. 4-①**) back and forth to bring it to focus. Once 532, 488, 637nm excitation paths are aligned, turn the all the lasers on to see every field is properly focused.*

6. Alignment of the free-channel image field. By adjusting the mirror (shown in **Fig. 4-⑦**), bring the field to the position (shown in **Fig. 6-③**).

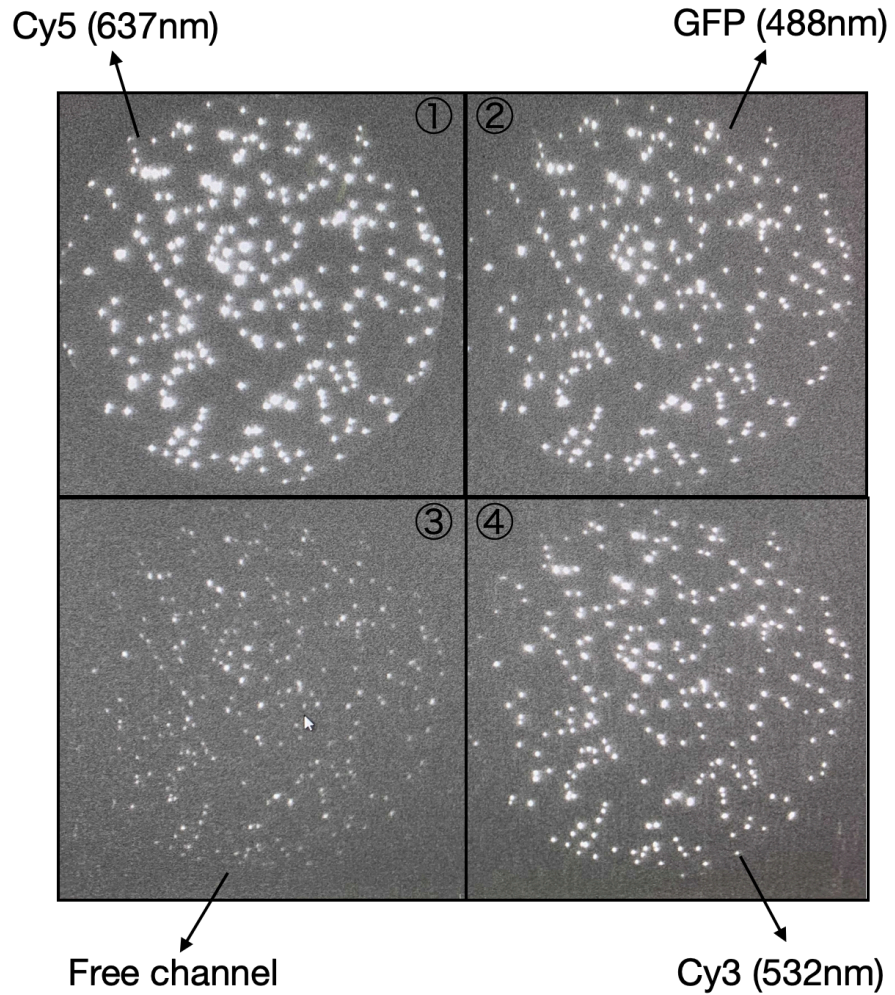


Figure 6. Images created on the CCD. CCD is divided into multiple channels for multi-color imaging. The higher left channel collects light in a wavelength range of 630 - 637 nm for Cy5 imaging. The higher right channel collects light in a wavelength range of 488 - 520 nm for GFP imaging. The lower right channel collects light in a wavelength range of 532 - 560 nm for Cy3, and the lower left channel collects light in a wavelength range of 570 - 600 nm with a current optical setup.

3.4.8 Adjustment of the laser power

The main purpose of changing the laser power is to obtain proper laser intensity so that the samples do not photobleach too fast or too slow.

1. **Measurement of laser intensity.** Place the laser power meter right behind the final focusing lens and turn the laser on. Turn the laser power meter on and read the intensity value on the screen.
2. **Rotating the half-waveplate on the excitation site.** Rotate the half-waveplate to change the laser intensity while checking the intensity value on the laser power meter.
3. **Examine with photobleaching measurement.** Once the laser intensity has been changed, carry out photobleaching experiments (see Chapter 2). Compare time to photobleach between now and before.

3.4.9 Micrometer slide ruler for scale bar

The main purpose of this protocol is to show how a scale bar is used on the microscope for images for future analyses.

1. **Placement of the micrometer slide ruler on the slide holder.** Invert the slide (coverslip faces objective) and place the micrometer slide ruler on the slide holder. Use tape to attach the slide on the slide holder stably.
2. **Preparation for using the micrometer slide ruler.** Change Readout Rate to 10 MHz at 14-bit to record at the fastest speed and disable Electron Multiplier Gain so that it does not damage the CCD chip and the light can be turned on while working. (Experiment setup -> Camera setup -> Horizontal pixel shift -> Readout rate)

3. Focusing the micrometer slide ruler and Recording. Move the sample in the x-y plane to bring in the scale bar (black lines) in the center then use the move in the z-direction to focus. Use white light (no laser required) to illuminate the scale. Record a short video on the CCD camera. * *Keep an eye on the slide while moving it in the z-direction so that it does not break or damage the objective lens.*

4. Adding a scale bar on the image. Stretch the scale bar image over the image that to be analyzed. Draw a line from the left edge of a black line to the left edge of the next right black line. This will be the size of your micrometer scale. If a 10 μm micrometer scale was used, the length of the line will be 10 μm . Delete the scale bar image and the scale bar will be attached to the image to be analyzed.

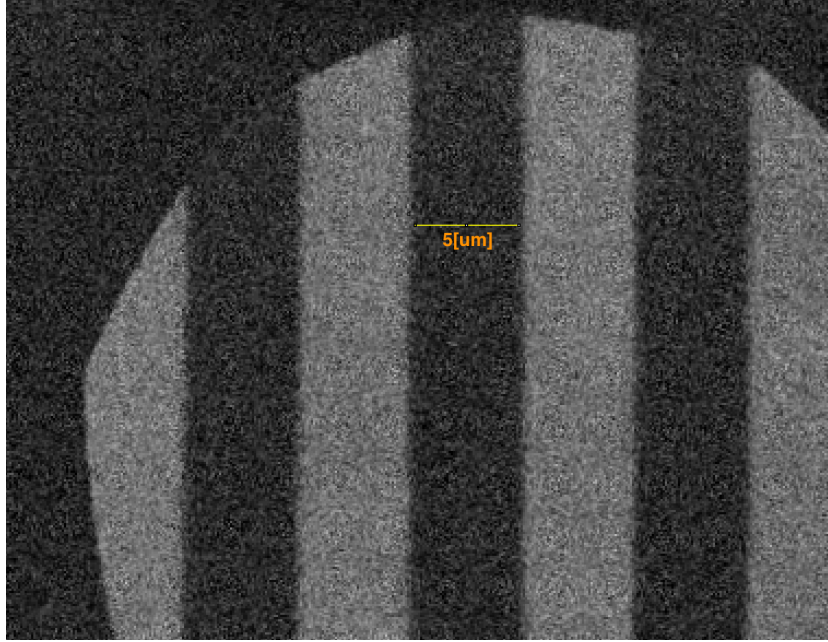


Figure 7. Micrometer slide ruler for scale bar. The image represents the micrometer slide ruler on the EMCCD camera (iXon 3). The scale bar was imaged by illuminating the fluorescent light on a 5 μm scale. The image goes through the lenses on the emission optical path, and the final image is created on the CCD. Considering the magnification of the emission path, the image on the sample stage will be magnified by 120 times ($300/3 \times 300/250$) considering the current optical setups meaning that a 5 μm distance on the sample stage will have a 600 μm distance on the CCD camera. This will take up 75 pixels on the CCD camera with an 8 $\mu\text{m} \times 8 \mu\text{m}$ individual pixel size of EMCCD.

References

1. L. J. Friedman, J. Gelles, Multi-wavelength single-molecule fluorescence analysis of transcription mechanisms. *Methods* **86**, 27-36 (2015).
2. J. Larson *et al.*, Design and construction of a multiwavelength, micromirror total internal reflectance fluorescence microscope. *Nat Protoc* **9**, 2317-2328 (2014).
3. S. H. White, W. C. Wimley, Membrane protein folding and stability: physical principles. *Annu Rev Biophys Biomol Struct* **28**, 319-365 (1999).
4. J. U. Bowie, Solving the membrane protein folding problem. *Nature* **438**, 581-589 (2005).
5. K. N. Fish, Total Internal Reflection Fluorescence (TIRF) Microscopy. *Curr Protoc* **2**, e517 (2022).

Chapter 4: A Thermodynamic Analysis of CLC Transporter Dimerization in Lipid Bilayers

4.1 Preface to the Chapter

We present the first report of a thermodynamic dissection of the assembly reaction of a large membrane protein complex in membranes, by carrying out a van 't Hoff analysis of the dimerization free energy of the chloride/proton antiporter CLC-ec1 in lipid bilayers to answer why membrane proteins form stable complexes via greasy interfaces instead of remaining solvated by the surrounding greasy lipids which we still do not understand the physical reasons due to a lack of quantitative experimental data for these reactions. This work has been published by Proceedings of the National Academy of Sciences of the United States of America (PNAS, 120, e2305100120, doi.org/10.1073/pnas.2305100120) in 2023 with authors, Dr. Rahul Chadda, Robyn Mahoney-Kruszka, Dr. Elizabeth Kelley, Dr. Nathan Bernhardt, Dr. Priyanka Sandal, and Dr. Janice L. Robertson.

4.2 Abstract

The CLC-ec1 chloride/proton antiporter is a membrane embedded homodimer where subunits can dissociate and associate, but the thermodynamic driving forces favor the assembled form at biological densities. Yet, the physical reasons for this stability are confounding since binding occurs via the burial of hydrophobic protein interfaces yet the hydrophobic effect should not apply since there is little water within the membrane. To investigate this further, we quantified the thermodynamic changes associated with CLC dimerization in membranes by carrying out a

van 't Hoff analysis of the temperature dependency of the free energy of dimerization, ΔG° . To ensure that the reaction reached equilibrium under changing conditions, we utilized a Förster Resonance Energy Transfer based assay to report on the relaxation kinetics of subunit exchange as a function of temperature. These equilibration times were then applied to measure CLC-ec1 dimerization isotherms as a function of temperature using the single-molecule subunit-capture photobleaching analysis approach. The results demonstrate that the dimerization free energy of CLC in *E. coli* like membranes exhibits a non-linear temperature dependency corresponding to a large, negative change in heat capacity, a signature of solvent ordering effects including the hydrophobic effect. Consolidating this with our previous molecular analyses suggests that the non-bilayer defect required to solvate the monomeric state is one source of the observed change in heat capacity and is a generalizable driving force for protein association in membranes.

4.3 Introduction

A long-standing mystery surrounding membrane proteins is how they fold and form stable macromolecular complexes inside the hydrophobic environment of the cellular membrane. As described in the two-stage model of alpha-helical membrane protein folding (1) non-polar helices must first partition into the membrane phase, and then these helices come together to form a thermodynamically stable folded structure, often via non-polar interfaces. The sheer observation of these structures indicates that the folded/assembled ensemble must be thermodynamically favorable over dissociated and disassembled forms, where the non-polar interfaces are solvated by the surrounding non-polar lipid solvent. For soluble proteins, which also assemble via hydrophobic interfaces, association is driven in large part due to the gain in free energy upon the burial of non-polar residues away from water, a phenomenon known as the hydrophobic effect (2). Yet, in the membrane, there is very little water, and so we do not expect the hydrophobic effect to be relevant.

Why then is the free energy of the assembled state more favorable in membrane environment and is there a compensatory generalizable solvent-dependent driving force that takes the place of the normally ubiquitous hydrophobic effect? This remains one of the major unanswered questions in our understanding of protein folding due to the limited amount of thermodynamic information of membrane protein assembly reactions in membranes.

To address this gap in our knowledge, we established a robust model system where greasy membrane protein association equilibrium is quantifiable in lipid bilayers (3–8). CLC-ec1 is a Cl⁻/H⁺ antiporter that forms a homodimer of two identical subunits, each containing its own independent transport pathway (9). The non-polar dimerization interface is relatively large, 1200 Å² per subunit and embedded within the membrane's hydrocarbon core. It is a robust protein system where the integrity of functional fold can be measured using reconstituted chloride transport assays (10), and structure can be determined using x-ray crystallography (11). It has also been demonstrated to be capable of existing in both dimeric and monomeric forms while preserving structure and function (3). Following this, we developed methods for quantifying the in-membrane equilibrium dimerization reaction of the CLC antiporter using single-molecule microscopy (4). This approach demonstrates that the dimerization is reversible and yields a free energy of stability of -10.9 kcal/mole relative to the 1 subunit/lipid standard state, in 2:1 POPE/POPG lipid bilayers. To put this into a practical perspective, this means that 10 subunits expressed in the inner membrane of *E. coli* containing 10⁷ lipids, will be observed in the dimeric form 90% of the time. From a biological standpoint, we interpret this thermodynamic stability as being more than sufficient as the dimer will be the predominant form at any reasonable expression level. Thus, it is apparent that CLC has evolved a mechanism for strong stability within the

membrane phase via greasy interfaces alone, while the physical reasons for this stability remain unknown.

A critical step in identifying the physical and molecular driving forces involved is the ability to decompose free energies into thermodynamically meaningful changes in enthalpy and entropy. In general, changes in enthalpy reflect differentials in non-bonded interactions, while changes in entropy reflect the difference in accessible microstates for the system. Understanding how each of these thermodynamic parameters change, in tandem with strategic inspection of the involvement of the protein and solvent, can reveal the molecular factors that define the balance of equilibrium. One way of accessing this information is by carrying out a van 't Hoff analysis of the temperature dependency of the reaction free energy. The change in the standard-state Gibbs free energy associated with dimerization, ΔG° , is defined as:

$$\Delta G^\circ = -RT \ln(K_{eq} \cdot \chi^\circ) \quad (1)$$

where R is the gas constant, T is the temperature in Kelvin, K_{eq} is the equilibrium association constant and χ° is the standard-state, which we define in mole fraction units as 1 subunit/lipid. Typically, the standard-state factor is omitted from this equation as it is conventionally set to the mathematically convenient value of 1 mole/L. However, since we are working in the 2-dimensional membrane reaction space (12) we select the similarly arbitrary, but mathematically convenient standard-state of 1 subunit/lipid for in-membrane reactions. Note, the term is explicitly included in eq. 1 so it is not forgotten, especially since other standard state definitions, such as area density are often used in the literature in this field. At a given temperature, T , the free energy is decomposed as:

$$\Delta G^\circ = \Delta H^\circ - T\Delta S^\circ \quad (2)$$

where ΔH° and ΔS° are the changes in standard-state enthalpy, and entropy associated with the dimerization reaction. Equating (1) and (2), yields the van 't Hoff equation:

$$\ln(K_{eq} \cdot \chi^\circ) = -\frac{\Delta H^\circ}{R} \frac{1}{T} + \frac{\Delta S^\circ}{R} \quad (3)$$

and plotting $\ln(K_{eq} \cdot \chi^\circ)$ vs. $1/T$ allows for the determination of ΔH° and ΔS° . If the enthalpy and entropy changes are temperature independent, then the relationship will be linear, with slope = $-\Delta H^\circ/R$ and y-intercept = $\Delta S^\circ/R$. However, proteins and their surrounding solvent, e.g., water or lipids, can possess high heat capacities, meaning that there may be significant changes in heat capacity associated with changes in protein conformation or assembly. With this, enthalpy and entropy changes will also depend on the temperature as follows:

$$\Delta H^\circ(T) = \Delta H_0^\circ + \Delta C_p(T - T_0) \quad (4)$$

$$\Delta S^\circ(T) = \Delta S_0^\circ + \Delta C_p \ln(T/T_0) \quad (5)$$

where ΔC_p is the change in molar heat capacity, T_0 is an arbitrary reference temperature, and ΔH_0° and ΔS_0° are the respective changes in enthalpy and entropy at the reference temperature. Thus, combining eq. (4) and (5) with (3), the van 't Hoff equation becomes a non-linear relationship:

$$\ln(K_{eq} \cdot \chi^\circ) = \left(-\frac{\Delta H_0^\circ}{RT} - \frac{\Delta C_p}{R} \left(1 - \frac{T_0}{T} \right) - \frac{\Delta C_p}{R} \ln \left(\frac{T_0}{T} \right) \right) + \frac{\Delta S_0^\circ}{R} \quad (6)$$

This is a complex function that has a quadratic dependency, but non-linear curve-fitting of $\ln(K_{eq} \cdot \chi^\circ)$ vs. $1/T$ with eq. 6 can provide the thermodynamic changes ΔC_p , ΔH_0° , ΔS_0° and T_0 that accompany the reaction.

In the present study, we report a thermodynamic dissection of the CLC-ec1 dimerization equilibrium in *E. coli* polar lipid (EPL) and 2:1 POPE/POPG lipid bilayers by carrying out a van 't Hoff analysis of the temperature dependency of the dimerization free energy. Both membrane conditions were verified to be in the liquid and bilayer phase across a wide range of temperatures to allow for these studies. To ensure equilibration of our samples across a wide range of temperatures, we developed a dynamic in-membrane subunit-exchange kinetic assay by measuring time-dependent ensemble FRET. In addition, we verify that the protein remains functionally capable of chloride transport from 22 - 62 °C under the same incubation conditions. With this, we can measure equilibrium CLC-ec1 dimerization isotherms as a function of temperature using the single-molecule subunit-capture photobleaching approach. The results show that the free energy of CLC-ec1 dimerization in EPL and 2:1 POPE/POPG membranes is temperature dependent, with a non-linear van 't Hoff relationship indicating an observation corresponding to a large negative change in heat capacity, $\Delta C_{P,EPL} = -2.0 \pm 0.3 \text{ kcal mol}^{-1} \text{ K}^{-1}$ and $\Delta C_{P,2:1POPE/POPG} = -1.7 \pm 0.3 \text{ kcal mol}^{-1} \text{ K}^{-1}$ and consequently, temperature dependent relationships of ΔH° and ΔS° . Such thermodynamic changes are a signature of the hydrophobic effect (13) as well as other solvent ordering changes such as those observed in phase transitions or may arise from coupling to other hidden equilibrium reactions, such as conformational changes. Consolidating these results with our previous computational analysis of membrane solvation structures around the dimerization

interface indicates that the non-bilayer membrane defect appearing exclusively in the monomeric state is the molecular basis for high heat capacity providing the energetic driving force for dimerization in membranes.

4.4 Materials and Methods

4.4.1 Protein purification

DNA constructs for CLC-ec1 C85A/H234C (WT), and C85A/H234C/R230C/L249C (RCLC) have been described earlier, along with their expression and purification methods (4, 6). Briefly, BL21-AI *E. coli* cells transformed with the expression plasmid were lysed by sonication and the protein extracted from membrane fragments into 2% n-Decyl- β -D-Maltopyranoside (DM; Anatrace, Maumee OH) containing 5 mM TCEP (Tris (2-carboxyethyl) phosphine; Soltec Bioscience, Beverly, MA) to ensure that the introduced cysteine residue at residue 234 (H234C) remains in a reduced state for maleimide labeling. After pelleting cellular debris by centrifugation, the protein was affinity purified using TALON cobalt affinity resin (Clontech Laboratories, Mountain View, CA) followed by size exclusion chromatography on Superdex 200 10/30 GL size exclusion column (GE Healthcare, Little Chalfont, UK) into size exclusion buffer (SEB): 150 mM NaCl, 20 mM MOPS pH 7.0, 5 mM analytical-grade DM. Molar extinction coefficients for WT and RCLC are 46,020 M⁻¹ cm⁻¹ and 49,630 M⁻¹ cm⁻¹ respectively, and molecular weights for WT and RCLC is 52,000 g/mol and 49,630 g/mol respectively.

4.4.2 Preparation of lipids

Detergent solubilized lipid micelles were prepared as described before (4). Briefly, a desired amount of *E. coli* polar lipid extract (EPL), 2:1 POPE/POPG or POPE/POPG/bovine

cardiolipin (Avanti Polar Lipids Inc., Alabaster, AL) in chloroform (25 mg/mL stock) was dispensed in a glass vial. The chloroform was evaporated under a continuous stream of 0.22 μm filtered Ultra High Purity N_2 gas (Airgas), and then the lipids were washed in pentane and then dried while rotating the vial, approximately 10-12 minutes, leaving a thin film of lipids along the walls and the bottom of the tube. After repeating the washing step twice, the lipid film was resuspended in Dialysis Buffer (DB: 300 mM KCl, 20 mM citrate pH 4.5, adjusted with NaOH) to a final concentration of 20 mg/mL and 35 mM of CHAPS was added. The lipid/detergent mixture was solubilized using a cup-horn sonicator (Qsonica) until the sample achieved a homogenous translucent appearance.

4.4.3 Protein labeling and reconstitution

After purification by size-exclusion chromatography, 10 μM protein was reacted with 50 μM of either Cy3-, or Cy5-, or a 1:8 mixture of Cy3- and Cy5- (Cy3/5) maleimide in DMSO (Lumiprobe Corporation, Hunt Valley, MD) for 10 minutes, then quenched with 5 mM cysteine from a 100 mM cysteine stock in SEB, pH adjusted to 7.0. The free dye was removed by re-binding the protein to a 0.2 mL cobalt affinity column (Talon), followed by excessive washing with 10-15 CV of cobalt column wash buffer (CoWB: 100 mM NaCl, 20 mM Tris, 5 mM DM, pH 7.5), and then elution with CoWB containing 400 mM imidazole, pH 7.5. As a final step, the imidazole was removed by running the eluted sample on a 3 mL Sephadex G-50 size exclusion column (Sigma-Aldrich). The labeling yield was quantified by placing the sample in a 1 cm quartz cuvette in a Nanodrop 2000c UV-VIS spectrophotometer and measuring the absorbance spectrum between 190-840 nm. For details on calculating the protein concentration, Cy3, Cy5 and Cy3/Cy5 labeling yield, see the **SI Appendix**.

For the bulk FRET experiments, co-labeled samples were reconstituted at 1 $\mu\text{g}/\text{mg}$, $\chi = 10^{-5}$ subunits/lipid in the EPL/CHAPS micelles and then dialyzed against dialysis buffer, at 4 $^{\circ}\text{C}$ in the dark, and maintaining a 1000-fold sample to dialysis buffer ratio with 5 buffer changes over 48-72 hours. The proteoliposomes used in the $\text{WT}_{\text{Cy3}} + \text{WT}_{\text{Cy5}}$ fusion experiments were also prepared at 1 $\mu\text{g}/\text{mg}$, $\chi = 10^{-5}$ subunits/lipid in the EPL/CHAPS micelles, in separate volumes that would correspond to a final acceptor to donor ratio that matches the co-labeled $P_{\text{Cy5}}/P_{\text{Cy3}}$ ratio. For example, if $P_{\text{Cy5}}/P_{\text{Cy3}} = 6$ for the co-labeled sample, and $P_{\text{Cy3}} = 0.80$ and $P_{\text{Cy5}} = 0.65$ for the independently labeled samples, then 100 μL of WT_{Cy3} and 747 μL of WT_{Cy5} liposomes were prepared and dialyzed separately, and the full volumes of each sample after dialysis were combined for the "fused" samples upon freeze-thaw. This resulted in fused samples with $P_{\text{Cy5}}/P_{\text{Cy3}} \sim 6$, even if there was variation in the dilution of the lipid concentrations in each cassette during dialysis. For freeze-thawing to form PLVs, proteoliposomes or empty liposomes were retrieved from dialysis, frozen and thawed by alternating between -80 $^{\circ}\text{C}$ and room temperature for 15 and 20 minutes respectively, for a total of two times and then stored at -80 $^{\circ}\text{C}$ until further use. Room temperature is defined as ambient laboratory temperature around 21-23 $^{\circ}\text{C}$.

For the photobleaching experiments, WT-Cy5 protein was mixed with 20 mg/mL EPL/CHAPS micelles at 0.0001, 0.001, 0.01, and 0.1 $\mu\text{g}/\text{mg}$, corresponding to $\chi = 10^{-9}$, 10^{-8} , 10^{-7} and 10^{-6} subunit/lipid mole ratio. In addition, "empty" EPL liposomes were prepared in parallel to use in the freeze-thaw fusion/dilution studies. To avoid any possibility of contamination, samples were dialyzed in separate buckets.

4.4.4 Bulk FRET measurements in PLVs

Förster Resonance Energy Transfer (FRET) was measured for fused or co-labeled EPL proteoliposomes in the PLV state using a Fluorolog 3-22 fluorometer with double monochromators on both excitation and emission paths (Horiba Jobin-Yvon, Edison NJ). Samples were excited at 550 nm and spectra was collected from 560 - 740 nm, with a 4 nm slit width, 0.05 s integration time. Typically, 0.3 mL of PLVs were added to a sub-micro quartz cuvette (Starna Cells, Atascadero, CA). Up to four samples were examined in parallel, maintained at a set temperature (22 – 80 °C) in the Peltier controlled 4-position turret holder (Horiba Jobin-Yvon, Edison NJ). The rate of acquisition was set at once every hour for 22, 31, and 37 °C samples, 30 minutes for the 44 °C, once every minute for the 50 and 56 °C, 1.5 minutes for the 62, 68, 74, 80 °C experiments. The ratiometric FRET signal was calculated as follows:

$$FRET\ signal = \frac{I_{Cy5,max}}{I_{Cy3,max} + I_{Cy5,max}} \quad (9)$$

For fitting of the subunit-exchange kinetics, the FRET signals were normalized by setting the first time point of the $WT_{Cy3+Cy5}^{fused}$ measurement, representing either the $WT_{Cy3}+WT_{Cy5}$ value before or immediately after freeze-thaw to 0, and the initial time point of the parallel $WT_{Cy3/Cy5}$ end-point control sample to 1. Depending on the sample and temperature, the normalized FRET signal was either time invariant (e.g., RCLC controls), showed a single exponential time constant (e.g., $WT_{Cy3+Cy5}^{fused}$), or two-component kinetics (e.g., $WT_{Cy3/Cy5}$ at high temperatures). To estimate the normalized FRET signal for the time invariant traces, the data was fit to a linear function, $Norm.FRET\ signal = m * t + b$, where t represents time in hours and the slope, m, was set to 0. For the single-exponential data, the time-course was fit to $Norm.FRET\ signal = Y_0 *$

$(Plateau - Y_0) * (1 - e^{-kt})$, with the initial value, Y_0 , set to 0. For the two component kinetic traces, the data was separated into a fast and slow component, and each region was fit with its own exponential association function as above. For the fast component, Y_0 was set to 0 for $WT_{Cy3+Cy5}^{fused}$ samples and 1 for $WT_{Cy3/Cy5}$ samples. The fits for the slow components were unconstrained.

For the FRET reversibility studies, $WT_{Cy3/Cy5}$, $WT_{Cy3+Cy5}^{fused}$, $RCLC_{Cy3/Cy5}$ or $RCLC_{Cy3+Cy5}^{fused}$, all at 1 $\mu\text{g}/\text{mg}$, $\chi = 10^{-5}$ subunits/lipid in EPL, in the PLV state, were retrieved from the cuvette after 48-hours of FRET measurements at 37 °C. The samples were mixed with 5X excess (v/v) 2:1 POPE/POPG PLVs containing 1 $\mu\text{g}/\text{mg}$, $\chi = 10^{-5}$ subunits/lipid of un-labeled WT protein. Typically, 60 μL of labeled sample was mixed with 240 μL of un-labeled sample. The membranes were fused by 3 freeze-thaw cycles, and the FRET scans were resumed on the diluted samples for additional 48 hours at 37 °C. The choice to dilute the samples with 2:1 POPE/POPG proteoliposomes was made to reduce the background signal due to a contaminating fluorescence in EPL.

The 2:1 POPE/POPG FRET measurements were carried out using a TECAN Spark plate reader with a modified procedure. Samples were excited at 534 nm and the emission spectra was collected from 553 – 740 nm, with a 4 nm step size and 40 μs integration time. Typically, 100 μL of PLVs were added to a black, half well 96-well plate (Corning). For 22 °C samples, a scan was done immediately after freeze-thaw and then the plate was kept in the dark, covered by aluminum foil and incubated at room temperature (≈ 22 °C) for 48 hours. For 37 °C samples, a scan was done immediately after freeze-thaw and then the plate was covered by aluminum foil and incubated in a benchtop incubator set to 37 °C for 48 hours. Additional scans were taken hourly for the first 5 – 8 hours, and then every 4 hours over 48 hours. For 56 and 62 °C samples, a scan was collected

immediately after freeze-thaw and then 3 x 1 mL aliquots of WT_{Cy3+Cy5}^{fused} and co-labeled WT_{Cy3/Cy5} samples were placed into dry baths set to 56 or 62 °C. For each measurement, 3 x 75 µL samples were taken and then placed on ice, in the dark, every 10 minutes over 1 hour and then every 30 minutes for another 2 – 3 hours for the 56 °C incubation. For the 62 °C incubation, samples were taken every minute over 10 minutes, then every 10 minutes over the course of an hour, and another sample at 1.5 hours. Once the time course was complete, the samples were added to a 96 well plate and scanned.

4.4.5 Single-molecule subunit capture photobleaching analysis

The details of this method have been described previously (4, 5). Briefly, WT CLC-ec1 is labeled with Cy5 and reconstituted across a wide range of protein densities, from $\chi = 10^{-9}$ to 10^{-6} subunits/lipid, corresponding to 0.0001 - 0.1 µg/mg of protein per lipid. These proteoliposomes are freeze-thawed (FT) to form large pauci-lamellar vesicles (PLVs) where multiple copies of subunits exist within each bilayer even at dilute protein densities. The PLV membranes are incubated at the desired temperature and then the samples are extruded forming small unilamellar vesicles with a defined size distribution. The statistics of subunit capture into the vesicle population follows a Poisson-like distribution and depends on the prior oligomer equilibrium distribution in the larger membranes. We quantify the probability distribution of Cy5-subunit occupancy per liposome by carrying out single-molecule photobleaching analysis on a total internal reflection fluorescence (TIRF) microscope, and then extract the fraction of dimer, F_{Dimer} , of the population by comparing the experimental probability distribution to monomer and dimer control distributions (6). Following this approach, we have been able to show that CLC-ec1 undergoes a reversible dimerization reaction in 2:1 POPE/POPG lipid bilayers, and reported an equilibrium constant of

$K_{eq} = 4.1 \times 10^7$ lipids/subunit corresponding to a free energy of $\Delta G^{\circ}_{2:1 POPE/POPG} = -10.9$ kcal/mole relative to the 1 subunit/lipid standard state (4, 6).

In the current studies, titrations were prepared by the reconstitution method (designated by super-script “R”) or by in-bilayer dilution. For dilution studies, WT-Cy5 PLVs were prepared at 1 $\mu\text{g}/\text{mg}$ and then combined with empty EPL PLVs to achieve in at 0.0001 $\mu\text{g}/\text{mg}$, 0.001 $\mu\text{g}/\text{mg}$, 0.01 $\mu\text{g}/\text{mg}$, and 0.1 $\mu\text{g}/\text{mg}$, $\chi = 10^{-9}$, 10^{-8} , 10^{-7} , and 10^{-6} subunits/lipids respectively, followed by 3 freeze-thaw cycles to fuse the membranes together. The diluted samples were incubated at the designated temperature (22 °C – 62 °C) in separate dry baths for indicated times, in the dark, to allow for equilibration of the dimerization reaction. Following this, the PLV samples were brought to room temperature before extrusion 21-times through a 400 nm nucleopore filter at room temperature. Liposomes were imaged using total internal reflection fluorescence (TIRF) microscopy and single-molecule photobleaching analysis was carried out as described before (4–6). Images were analyzed as described previously using custom image analysis software in MATLAB (38).

For the lower temperature studies (4 °C, 11 °C, 18 °C), the 4 °C samples were incubated in the cold room (4 °C – 5 °C) in the dark, and the samples (11 °C, 18 °C) were incubated in a dry bath in the cold room. The photobleaching experiments were done at 0.001 $\mu\text{g}/\text{mg}$ after 2, 4, 6, 16, 20, 45 weeks to check whether the samples reached dimerization equilibrium after the incubation.

4.4.6 K_{eq} and van 't Hoff parameter estimation

The fraction of subunits in the dimeric form, F_{Dimer} , was estimated from the single-molecule photobleaching probability distributions as described previously (4, 6, 39). To estimate K_{eq} for each sample, a bootstrap fitting analysis script was written in MATLAB and carried out on

the cumulative F_{Dimer} , vs. χ^* data set selecting 8 data points at random from a total set of 12-20, and fitting to the dimerization isotherm:

$$F_{Dimer} = \frac{1 + 4\chi^*K_{eq} - \sqrt{1 + 8\chi^*K_{eq}}}{4\chi^*K_{eq}} \quad (10)$$

The selection process was iterated 100 times with K_{eq} limits = $\{10^{-10}, 10^{-5}\}$. All estimates are reported in **Table S2**.

The van 't Hoff fitting was carried out in two ways. First, the mean \pm standard deviation from the bootstrapped estimates of K_{eq} were fit with the linear (eq. 3) and non-linear (eq. 6) forms of the van 't Hoff equations in GraphPad Prism for simpler visualization. Second, a bootstrap estimation approach was used by writing a MATLAB script to fit the $\ln(K_{eq})$ vs $1/T$ estimation set to the linear and non-linear functions. For EPL samples, 15 data points were selected from a total set of 900, iterated 1000 times. For the 2:1 POPE/POPG samples, non-linear and linear van 't Hoff fittings were carried out with 30 data points selected from a total set of 400, iterated 1000 times. The results from the fitting for both linear and non-linear models, are reported in **Table S3**.

4.4.7 Functional measurements

Chloride transport assays from 400 nm extruded liposomes were performed as described previously (4, 10). After completion of the bulk FRET measurements, the PLV samples were retrieved from cuvettes and stored in sealed tubes at room temperature, 2-3 days, until the functional assays could be conducted. For 62 °C experiment, the sample was incubated for 0.1 h at 62 °C in the dry bath to capture the state in equilibrium before the aggregation reaction happens. For higher temperature (68 – 80 °C) samples, the chloride transport assays were conducted after

incubating the samples for 2.5 ± 0.8 h at 68 °C, 1.9 ± 0.2 h at 74 °C and 2.7 ± 1.2 h at 80 °C so that the plateau is reached in aggregation reaction from bulk FRET measurements. For 2:1 POPE/POPG samples, the chloride transport assays were conducted after incubating the samples for 46.0 ± 1.0 h at 37 °C, 0.6 ± 0.0 h at 56 °C and 0.3 ± 0.0 h at 62 °C, mean \pm standard deviation, all $n = 3$.

Materials and methods related to supplementary data for differential scanning calorimetry, small-angle x-ray scattering and the calculation of the number of waters associated with the membrane in molecular dynamics simulations can be found in the **SI appendix**.

4.5 Results

4.5.1 CLC-ec1 dimers exhibit dynamic subunit exchange in lipid bilayers

Before measuring the temperature dependency of the dimerization equilibrium of CLC-ec1, we first needed a way of monitoring reaction equilibration as a function of temperature. Previously, we assessed the dynamic equilibration of CLC-ec1 dimerization in 2:1 POPE/POPG lipid bilayers using the single-molecule subunit capture approach (4). This method examines the population of Cy5 labeled CLC-ec1 subunits that are reconstituted into large, multilamellar membranes.

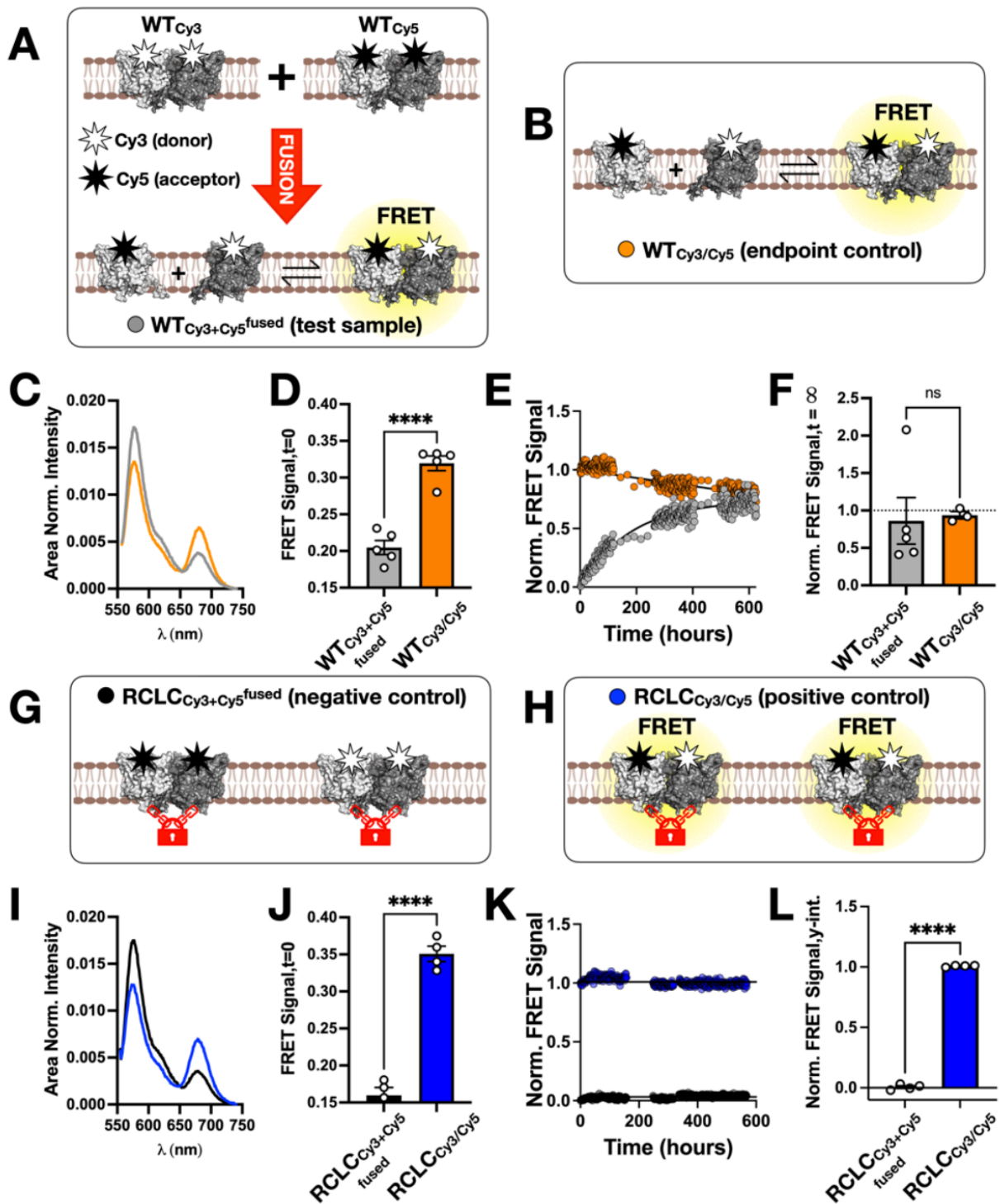


Figure 1. Dynamic exchange CLC-ec1 subunits in membranes observed by bulk FRET. (A) Cartoon depicting the subunit exchange reaction in membranes. CLC-ec1 is labeled with FRET donor Cy3 (white star) or FRET acceptor Cy5 (black star) and reconstituted into EPL bilayers at $\chi = 10^{-5}$ subunits/lipid. The following samples are studied: WT_{Cy3+Cy5}^{fused} (light grey) indicates separately labeled proteoliposome samples that have been fused into the same membrane by 3x freeze-thaw and (B) a reaction endpoint positive control of WT co-labeled with Cy3 and Cy5

before reconstitution, WT_{Cy3/Cy5} (orange). **(C)** Area normalized bulk emission spectra from excitation at 565 nm for WT_{Cy3} + WT_{Cy5} and WT_{Cy3/Cy5} right before fusion, defined as $t = 0$. **(D)** Initial FRET signal = $I_{Cy5,max}/(I_{Cy3,max} + I_{Cy5,max})$ showing significant increase in heterodimeric FRET signal in the WT_{Cy3/Cy5} sample. Data represented as mean \pm sem, $n = 5$. Statistics calculated using the unpaired parametric student's t-test (****, $p < 0.0001$). P_{Cy5}/P_{Cy3} labeling ratios were comparable, WT_{Cy3+Cy5}^{fused} = 5.8 ± 0.6 , WT_{Cy3/Cy5} = 5.8 ± 0.4 (ns, $p = 0.96$). **(E)** Time-dependent normalized FRET signals for WT samples at ambient temperature, ≈ 22 °C. The data is normalized by defining the initial time point of the WT_{Cy3+Cy5}^{fused} samples as 0 and the co-labeled WT_{Cy3/Cy5} signal as 1, and time-courses are fit to an exponential association function with Y_0 constrained to 0 and 1 respectively. **(F)** Endpoint normalized FRET signals, defined from the plateau value for the exponential fit (ns, $p = 0.46$). **(G)** Cartoon depicting the negative control RCLC_{Cy3+Cy5}^{fused} (black) with R230C/L249C intersubunit disulfide cross-linked CLC-ec1-Cy3 and CLC-ec1-Cy5 incapable of subunit exchange, and **(H)** positive control RCLC_{Cy3/Cy5} co-labeled with Cy3 and Cy5 prior to reconstitution. **(I)** Area normalized emission spectra from RCLC_{Cy3+Cy5} and RCLC_{Cy3/Cy5} right before fusion, defined as $t = 0$. **(J)** Initial FRET signal for RCLC_{Cy3+Cy5} and RCLC_{Cy3/Cy5}, data represented as mean \pm sem, $n = 4$, (***, $p = 0.0007$). P_{Cy5}/P_{Cy3} labeling ratios were comparable, RCLC_{Cy3+Cy5}^{fused} = 4.6 ± 0.4 , RCLC_{Cy3/Cy5} = 4.0 ± 0.2 (ns, $p = 0.1934$). **(K)** Time-dependent normalized FRET signals for RCLC samples at ambient temperature, ≈ 22 °C with linear fits (slope = 0). **(L)** Y-intercept FRET signals from the linear fit (****, $p < 0.0001$).

The samples can be incubated under different conditions, and then the protein population is assessed by measuring the random capture of subunits into extruded liposomes, which follows Poisson-like statistics. This is quantified by direct counting of subunit occupancy in liposomes using single-molecule photobleaching analysis. Provided the protein density, Cy5 labeling yield and liposome size distribution are known, then the photobleaching probability distribution directly reports on the proportion of monomers and dimers in the original membranes. In our previous study, we examined time-dependent equilibration by carrying out a perturbative dilution study in the membrane, where a dimeric population was diluted by freeze-thaw fusion with empty vesicles and the protein population observed to shift towards monomers when examined by single-molecule photobleaching (4). This reaction was studied at room temperature, ≈ 22 °C, and the conversion of the photobleaching distribution, with increasing single-step photobleaching

probabilities, P_1 , and decreasing two-step probabilities, P_2 , were observed to slowly relax with $t_{1/2} = 4.2$ days. (**Fig. S4A**).

This study demonstrated path-independence of the reaction, but since it only reflects the shift towards monomers, we wanted to develop another method to report on the formation of new dimeric species in the system. We did this by measuring the subunit-exchange behavior of CLC-ec1 at constant protein density. In the subunit-exchange assay, WT CLC-ec1 is labeled by either a FRET donor, Cy3, or FRET acceptor, Cy5, and then reconstituted separately into EPL bilayers at densities where the dimeric form prevails, e.g., $1 \mu\text{g}/\text{mg}$ or $\chi = 10^{-5}$ subunits/lipid (**Fig. 1A**). The donor and acceptor-labeled subunits are then introduced into the same membrane by freeze/thaw mediated fusion, $\text{WT}_{\text{Cy3}+\text{Cy5}^{\text{fused}}}$, where subunits dissociate, diffuse and re-associate leading to the formation of new Cy3/Cy5 heterodimers was monitored by measuring the ratiometric FRET signal. This is compared to a positive endpoint control where WT is originally co-labeled with Cy3/Cy5, $\text{WT}_{\text{Cy3}/\text{Cy5}}$ (**Fig. 1B**). To examine the dynamic range to detect subunit exchange, separately labeled proteoliposome samples of WT_{Cy3} and WT_{Cy5} were aliquoted in the same cuvette at a ratio of $P_{\text{Cy5}}/P_{\text{Cy3}} = 6.0 \pm 0.5$, but not fused, yielding a baseline FRET signal for $\text{WT}_{\text{Cy3}} + \text{WT}_{\text{Cy5}}$ of 0.20 ± 0.01 . This reflects the background FRET signal that corresponds to the initial condition of no Cy3/Cy5 heterodimers, yet the endpoint control of $\text{WT}_{\text{Cy3}/\text{Cy5}}$ labeled at a ratio of $P_{\text{Cy5}}/P_{\text{Cy3}} = 6.2 \pm 0.6$, yielded a FRET signal for $\text{WT}_{\text{Cy3}/\text{Cy5}}$ of 0.32 ± 0.01 , a significant increase over the background (**Fig. 1C, D**). Upon incubation of $\text{WT}_{\text{Cy3}+\text{Cy5}^{\text{fused}}}$ sample at room temperature, a slow but consistent increase in FRET is observed which converges to the $\text{WT}_{\text{Cy3}/\text{Cy5}}$ co-labeled FRET signal with a $t_{1/2} = 8.9 \pm 1.8$ days (**Fig. 1E, F**), on the order of what we observed in our photobleaching dilution study in 2:1 POPE/POPG (4). Since the reaction occurs over long timescales, we compared these results with control studies on R230C/L249C (RCLC) CLC-ec1, which forms

spontaneous inter-subunit disulfide bonds and is incapable of subunit exchange (6, 14). In this case, the negative control is reflected by fusion of RCLC_{Cy3} and RCLC_{Cy5} liposomes, RCLC_{Cy3+Cy5}^{fused} (Fig. 1G) and the positive control is given by the co-labeled RCLC sample, RCLC_{Cy3/Cy5} control samples (Fig. 1H). While a similar dynamic range is observed (Fig. 1I, J), these constitutively dimeric constructs show unchanged FRET signals over the same period (Fig. 1K, L), ruling out artifacts from non-specific protein aggregation or differential bleaching of fluorophores along this timescale. Altogether, these results support the hypothesis that the exponentially saturating increase in FRET signal observed in WT samples is due to CLC subunit-exchange within the membrane.

4.5.2 CLC-ec1 undergoes subunit-exchange across many temperatures while remaining functionally folded

In these studies, we focus first on the reaction in EPL, because of prior studies indicating that the gel to liquid phase transition is lower, reported as $T_{m,EPL} \approx 2 \text{ }^\circ\text{C}$ (15) vs. $T_{m,2:1POPE/POPG} \approx 19 \text{ }^\circ\text{C}$ (16) in SUV preparations. However, our studies are conducted with freeze/thawed membranes and studies of large EPL membranes have shown the ability to undergo hexagonal phase transitions at higher temperatures, attributed to the combination of PE and cardiolipin (17–19). To investigate this, we studied our freeze/thawed EPL membranes and compared these with 2:1 POPE/POPG (Fig. S1). Differential scanning calorimetry (DSC) shows that freeze/thawed EPL membranes do not show any main phase transition from 0 - 100 °C, or any hexagonal phase at higher temperatures. To compare, we examined freeze/thawed 0.67 POPE/0.33 POPG (i.e., 2:1 POPE/POPG) and 0.67 POPE/0.23 POPG/0.1 bovine cardiolipin and these samples showed the main gel to liquid phase transition in the 15 - 20 °C range, but also did not depict an additional phase transition at higher temperatures (Fig. S1A). In case the signal is not detectable by DSC, we

examined the same membrane preparations by small-angle x-ray scattering (SAXS). First, we reviewed the morphology of these large liposome preparations by re-analyzing our previous cryo-EM imaging studies of 2:1 POPE/POPG liposomes after freeze/thaw (20). As expected, these liposomes are large and can contain multiple layers, but are mainly uni- and bi-lamellar (**Fig. S1B, S1C**). We therefore refer to them as paucilamellar vesicles (PLVs), where the preferential formation of unilamellar structures is likely due to the lipid charge (21). The membranes readily fuse within two freeze/thaw cycles, as indicated by FRET measurements of NBD-POPE and Rhodamine-B-POPE doped membranes (**Fig. S1D**). The SAXS spectra for both 2:1 POPE/POPG and EPL show the bilayer features, but with a lack of Bragg peaks that are often found in multilamellar samples, in agreement with our finding of these being predominantly uni- and bi-lamellar distributions (**Fig. S1E**). From these spectra, the low q scattering data was fit with a bilayer shape form, for both EPL and 2:1 POPE/POPG PLVs, to obtain measurements of the phosphate-phosphate bilayer thickness (**Fig. S1F**) and interlamellar spacing (**Fig. S1G**). In both EPL and 2:1 POPE/POPG conditions, across increasing temperatures, we found no significant changes in the bilayer properties, and no evidence of hexagonal phase transition. The disparities between our membrane preparations and those reported previously (17–19), may be due to the differences in lipid composition with *E.coli* growth temperatures, lipid concentrations and hydration levels in the preparations, or the high salt and low pH conditions of our buffer, all of which can influence the structure and phase behavior of lipid mixtures.

With evidence that the bilayer structure and properties do not change significantly over this temperature range, we carried out the subunit-exchange experiment while incubating samples at different temperatures from 31 to 80 °C. As expected, increasing temperature accelerates the rate of CLC subunit exchange in the WT samples (**Fig. 2A, B**), but not RCLC (**Fig. 2C**). Examining

the WT reaction alone, up to 37 °C, we observe comparable behavior to the room temperature samples, with $WT_{Cy3+Cy5}^{fused}$ showing an exponential association while $WT_{Cy3/Cy5}$ remained generally constant.

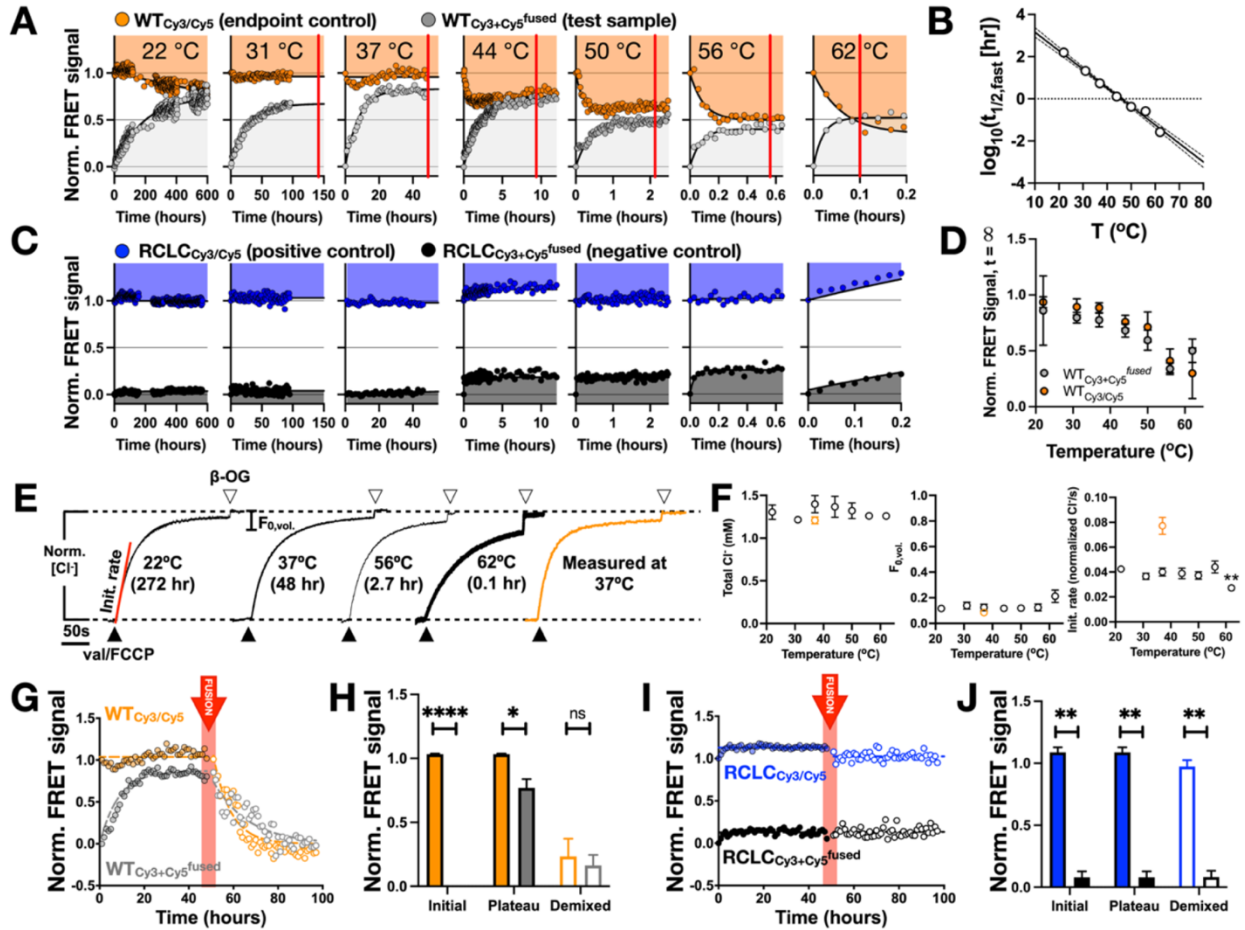


Figure 2. Temperature dependency and reversibility of CLC-ec1 subunit exchange in membranes. (A) Normalized time-dependent FRET signals for WT as a function of increasing temperature, 22 - 62 °C. Data are fit with an exponential association curves with time constant $t_{1/2,fast}$. (B) Plot of $\log(t_{1/2,fast})$ as a function of temperature, fit with a straight line. (C) Lack of subunit exchange in RCLC samples. Data are fit with a straight line, slope = 0. (D) Normalized end-point FRET signals from fitted plateaus. Data represented as mean \pm sem, $n = 2 - 6$. (E) Representative chloride efflux traces from liposomes reconstituted at $\chi = 1 \times 10^{-5}$ subunits/lipid in EPL incubated at 22 - 62 °C for the noted time, then measured at room temperature. Black triangle - addition of valinomycin/FCCP, white triangle - addition of β -OG. Orange trace shows a chloride transport measurement conducted directly at 37 °C. (F) Total Cl^- concentration in the measurement cell after addition of β -OG, fractional volume of inactive vesicles, $F_{0,vol}$, and initial rate of chloride efflux as a function of incubation temperature. Data represented as mean \pm sem, $n = 2 - 4$. Statistical tests were calculated using an un-paired parametric student's t-test compared to the 22 °C data. (G) Reversibility of the heterodimeric $\text{WT}_{\text{Cy3/Cy5}}$ FRET signal at 37 °C examined by freeze-thaw fusion with 5x volume of unlabeled WT proteoliposomes. (H) End-point FRET signals before and after dilution by unlabeled protein. (I) Disulfide cross-linked $\text{RCLC}_{\text{Cy3/Cy5}}$ does not show reversibility, (J) and no significant changes in end-point FRET signals after dilution.

However, at higher temperatures, WT_{Cy3/Cy5} exhibited an exponential decay, with the two samples converging to a lower plateau value. At 62 °C and above, a second kinetic component is also observed, with a slowly increasing FRET signal in both WT and RCLC samples (**Fig. S2**). For the WT samples, these two behaviors can be separated by fitting with fast and slow time dependencies, whereas the RCLC samples only show the slow time component. The fast component between 22 - 62 °C reveals a linear relationship between the logarithm of $t_{1/2, fast}$ and temperature (**Fig. 2B**). Under our experimental conditions, the exponential fits mainly report on the dissociation rate constant (22). Increasing temperature speeds up the reaction that is being observed, which is what would be expected for simple dissociation. However, other reaction mechanisms remain possible, which would require further kinetic analysis to dissect. Examining the plateau FRET values from these fits shows that the fast component is contained within the endpoint control (**Fig. 2D**), while the slow component leads to an increase in FRET beyond the co-labeled WT_{Cy3/Cy5} or RCLC_{Cy3/Cy5} dimeric samples suggesting possible higher-order aggregation of the protein within the membrane at temperatures > 62 °C.

Next, we investigated whether the subunit-exchange exists between folded subunits by measuring chloride transport function from the exact same proteoliposomes studied in our FRET measurements, after the equilibration was complete, generally 8 times longer than $t_{1/2, fast}$ (**Fig. 2E**). After incubation at elevated temperatures, the membranes are still capable of holding a chloride gradient, maintain the capacity to transport chloride at comparable rates and with similar fractions of active vesicles (**Fig. 2F**) compared to liposomes at room temperature. Only samples that were incubated > 62 °C and for extended periods of time showed a significant decrease in activity corresponding to possibly aggregated protein accompanied by the increased FRET signals (**Fig. S3**), with similar results were observed with the RCLC controls. Finally, we measured the transport

activity of WT directly at 37 °C, and the transport activity increases, further supporting the model that elevated temperatures accelerate the kinetics of subunit-exchange, which occurs via functionally folded subunits.

As a final test, we examined whether the increasing FRET signal observed in WT_{Cy3+Cy5}^{fused} samples at 37 °C was reversible by diluting the end-point FRET samples by freeze-thaw fusion with 5-times excess of un-labeled WT proteoliposomes. Upon fusion, we observe that both WT_{Cy3+Cy5}^{fused} and WT_{Cy3/Cy5} signals exponentially decrease (**Fig. 2G, H**) while RCLC samples show no change (**Fig. 2I, J**). Altogether, these results support the hypothesis that the fast time dependency in FRET signals observed from 22 - 62 °C reflects the dynamics of CLC subunit exchange, and that this behavior is separable from other reactions, such as aggregation, that dominates at higher temperatures.

4.5.3 The temperature dependency of CLC-ec1 dimerization equilibrium in EPL membranes

Having validated that the CLC dimerization reaction is well-defined from 22 - 62 °C, we carried out a van 't Hoff analysis of the dimerization free energy by measuring equilibrium dimerization isotherms across the pre-validated range of incubation temperatures. From our previous experiments monitoring time dependent FRET, we observed some changes in the plateau FRET values that could correspond to changes in dimerization (**Fig. 2A, D**). To quantify this rigorously,

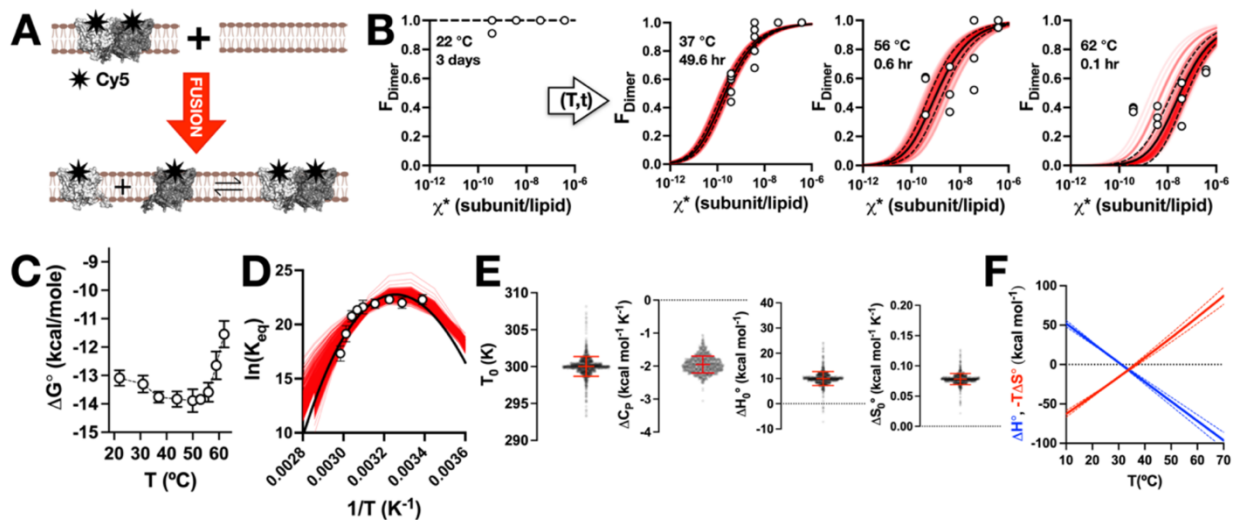


Figure 3. Temperature dependency of CLC-ec1 dimerization equilibrium in EPL membranes. (A) Schematic of the dilution titration experiment. WT_{Cy5} CLC-ec1 is reconstituted in EPL at $\chi_{rec.} = 2 \times 10^{-5}$ subunits/lipid where dimers are predominant. The final mole fraction density is achieved by in-membrane dilution 10-10,000x by freeze-thaw fusion with empty EPL vesicles, then incubated at the indicated temperature for $t_{inc.} \approx 8 \times t_{1/2}$ of the subunit-exchange relaxation time. (B) The single-molecule photobleaching subunit capture approach is used to measure the resultant dimer population in the membrane, F_{Dimer} vs. χ^* , for non-equilibrated samples at 22 °C diluted and assessed after only 3 days incubation, 37 °C diluted after 49.6 h incubation, 56 °C dilution after 0.6 h, and 62 °C dilution after 0.1 h incubation. Data represent $n = 3-5$ independently prepared samples. Red lines indicate bootstrap fitting to the equilibrium dimerization isotherm in MATLAB (8 data points selected at random from a total set of 12-20, iterated 100 times and limits = $\{10^{-10}, 10^{-5}\}$). Black line indicates non-linear fitting of all experimental data to the dimerization isotherm with GraphPad Prism. (C) Average bootstrapped distributions of ΔG° (kcal/mole), mean \pm STD. All populations are significantly different ($p < 0.0001$, unpaired parametric t-test) from the reconstituted, equilibrated 22 °C sample (22^R). (D) Non-linear van 't Hoff fitting carried out by bootstrapping analysis in MATLAB (15 data points selected from a total set of 900, iterated 1000s). (E) Distributions of thermodynamic parameters from non-linear bootstrapping fits (mean \pm STD, 1000 bootstrapped fits): $T_0 = 300.0 \pm 1.3$ K, $\Delta C_p = -2.0 \pm 0.3$ kcal mol⁻¹ K⁻¹, $\Delta H_0^\circ = 10.0 \pm 2.7$ kcal mol⁻¹ and $\Delta S_0^\circ = 0.078 \pm 0.009$ kcal mol⁻¹ K⁻¹. (F) Temperature dependent enthalpy (blue) and entropy (red) contributions to the change in free energy of CLC dimerization in membranes. Data represented as mean \pm STD, 1000 bootstrapped values.

we returned to our single-molecule subunit capture approach that allows us to carry out a full titration of the dimerization reaction as a function of protein density to measure the equilibrium constant as a function of temperature (4, 5). In these studies, we reconstituted the protein across a

density range of $\chi = 10^{-9}$ to 10^{-6} subunits/lipid, again in the membrane condition of *E. coli* polar lipid (EPL) extract (**Fig. S5**, “22^R” samples). The EPL lipid environment has a stabilizing effect on the CLC-ec1 dimerization, with $K_{eq} = 5.3 \pm 1.9 \times 10^9$ lipids/subunit and $\Delta G_{EPL}^\circ = -13.1 \pm 0.3$ kcal/mole, resulting in a stabilization of $\Delta \Delta G_{EPL-2:1 POPE/POPG} = -2.3$ kcal/mole (**Table S2**).

To isolate and study the effect of temperature on the K_{eq} , proteoliposomes prepared at $\chi = 10^{-5}$ subunits/lipid, i.e., 1 $\mu\text{g}/\text{mg}$ density, were serially diluted by freeze/thaw fusion with excess membranes and then incubated at various temperatures for the appropriate equilibration time (**Fig. 3A**). This perturbative approach ensured identical initial conditions for all samples, and with that an ability to robustly measure changes in the dimerization isotherms due to the difference incubation conditions. The sample diluted and incubated at 22 °C showed no change in photobleaching probability distribution over period of 1-3 days acting as a non-equilibrated negative control (**Fig. 3B**). For the other temperatures, 31 - 62 °C, the samples are incubated for $\approx 8 \times t_{1/2, fast}$ as measured by the bulk FRET subunit-exchange relaxation kinetics. The results show that the equilibrium dimer distribution shifts with temperature, which is apparent above 53 °C, and reflected in the distribution of the dimerization free energies (**Fig. 3C**). Plotting the data in van 't Hoff form, $\ln(K_{eq} \cdot \chi^\circ)$ vs. $1/T$, shows that the data is best described by a non-linear van 't Hoff model, indicative of a change of heat capacity upon dimerization (**Fig. 3D**). Over the temperature range of $T = 22 - 62$ °C, this yields a reference temperature of $T_0 = 300.0 \pm 1.3$ K and observed thermodynamic parameters of $\Delta H_0^\circ = 10.0 \pm 2.7$ kcal mol⁻¹ K⁻¹, $\Delta S_0^\circ = 0.078 \pm 0.009$ kcal mol⁻¹ K⁻¹, and $\Delta C_P = -2.0 \pm 0.3$ kcal mol⁻¹ K⁻¹ (**Fig. 3E, Table S3**). The large change in heat capacity consequently means that ΔH° and ΔS° are temperature dependent functions (**Fig. 3F**), and at the physiological temperature of $T = 37$ °C, $\Delta H_{310}^\circ = -9.5 \pm 2.5$ kcal mol⁻¹ and $-T\Delta S_{310}^\circ = -4.4 \pm 2.4$ kcal mol⁻¹. A consequence of a non-linear van 't Hoff relationship is that it exhibits a quadratic

dependency on temperature, predicting that dimerization becomes weaker at colder temperatures. To test this prediction, we attempted measurements below room temperature, but did not observe significant perturbations in our starting probability distributions. We expect that the experiments are limited by the exceedingly slow kinetics under these conditions (**Fig. S4**), and so we restrict our conclusions for this reaction to the testable range of $T = 22 - 62$ °C.

4.5.4 CLC-ec1 dimerization exhibits a non-linear temperature dependency in 2:1 POPE/POPG

EPL is a crude membrane extract, and although it allows these studies to be conducted at lower temperatures, this complex membrane preparation introduces complexity. DSC and SAXS measurements (**Fig. S1**) indicate that there are no discernable changes in bilayer phase or structure as temperatures are increased. However, as an alternate approach, we studied the CLC-ec1 dimerization reaction in 2:1 POPE/POPG lipid bilayers, a simpler synthetic mimic of the EPL composition. We first examined whether dynamic subunit exchange of CLC-ec1 was observable in this lipid composition. As in EPL, WT_{Cy3+Cy5}^{fused} vs. WT_{Cy3/Cy5} CLC-ec1 in 2:1 POPE/POPG shows a significant dynamic range in the FRET signal enabling the characterization of Cy3/Cy5 heterodimer formation in the membrane (**Fig. 4A**). Following the samples after freeze/thaw fusion into the same membrane, WT_{Cy3+Cy5}^{fused}, reveals a similar exponentially increasing time course that becomes faster as the temperature is increased (**Fig. 4B**). Estimation of the endpoint FRET signals indicates that the WT_{Cy3+Cy5}^{fused} and WT_{Cy3/Cy5} FRET signals converge supporting equilibration of the dimer complexes (**Fig. 4C**), and the protein remains functional for chloride transport even after incubation at higher temperatures (**Fig. 4D**). Measurements of the dimerization isotherms of CLC-ec1 in 2:1 POPE/POPG membranes after dilution and incubation at 37, 56 and 62 °C show that

protein populations redistribute into temperature dependent dimerization isotherms (**Fig. 4E**, **Table S2**).

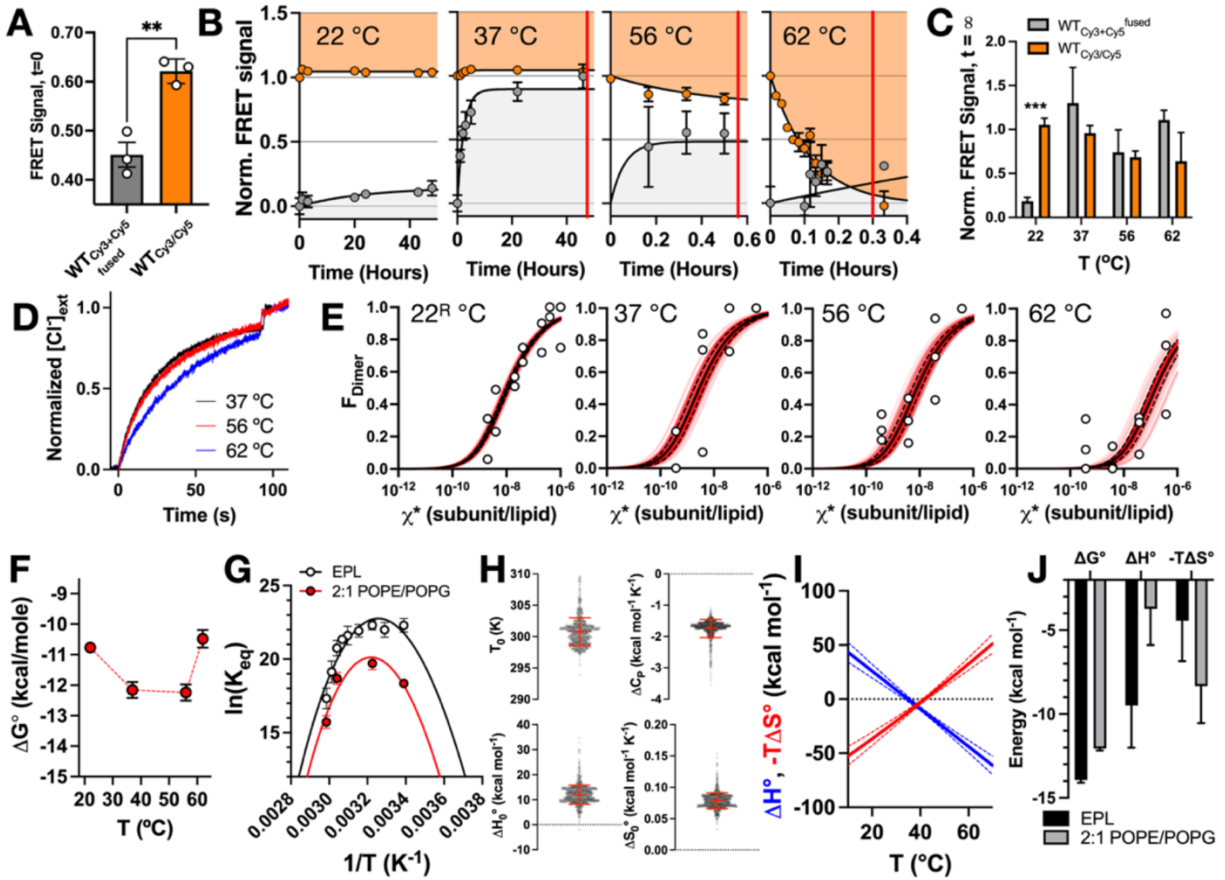


Figure 4. Temperature dependency of CLC-ec1 dimerization in 2:1 POPE/POPG lipid bilayers. (A) FRET signals for WT_{Cy3+Cy5}^{fused} and WT_{Cy3/Cy5} in 2:1 POPE/POPG prior to membrane freeze/thaw (mean ± sem, n = 3; **, p = 0.0042). (B) Subunit-exchange reactions as a function of incubation temperature. Data represented as mean ± std for n = 2-3 reading replicates. Black lines indicate exponential fits, while the red line shows the incubation times for the dimerization equilibration studies: 46 ± 1 hours for 37 °C, 0.6 ± 0.0 hours for 56 °C and 0.3 ± 0.0 hours for 62 °C, mean ± sem, n=3. (C) Endpoint estimates of normalized FRET signals subunit exchange, WT_{Cy3+Cy5}^{fused} and WT_{Cy3/Cy5} endpoints are not significantly different, except for 22 °C (***, p = 0.0006) as samples were not equilibrated and only monitored for 2 days. (D) Representative traces of Cl⁻ transport function from CLC-ec1 in 2:1 POPE/POPG vesicles extruded after incubation at 37 °C for 46 hours, 56 °C for 0.6 hours and 62 °C for 0.3 hours. (E) Equilibrium dimerization isotherms from subunit capture photobleaching analysis, as described in Fig. 3. Data represent n = 3 independently prepared samples. Red lines indicate bootstrap fitting of the experimental data to the equilibrium dimerization isotherm in MATLAB, with 8 – 14 data points (67% of total) selected at random from a total set of 12-21, iterated 100 times and limits = {8.5⁻⁹, 10⁻⁵}. Black line indicates direct non-linear fitting of all experimental data to the dimerization isotherm with GraphPad Prism. (F) Average bootstrapped distributions of ΔG° (kcal/mole), mean ± standard deviation. All populations are significantly different (p < 0.0001, unpaired parametric t-test) from the reconstituted, equilibrated 22 °C sample (22^R). (G) Non-linear (lnK_{eq}(T) = -ΔH₀^o/RT - ΔC_P(1 - T₀/T)/R + ΔS₀^o/R - (ΔC_P/R)ln(T₀/T)) van 't Hoff fitting of mean ± std 2:1 POPE/POPG (red) and EPL (black) results. (H) Distributions of thermodynamic parameters from non-linear bootstrapping fits (mean ± standard deviation over 1000 bootstrapped

fits): $T_0 = 300.8 \pm 2.2$ K, $\Delta C_p = -1.7 \pm 0.3$ kcal mol⁻¹ K⁻¹, $\Delta H_0^\circ = 12.0 \pm 3.8$ kcal mol⁻¹ and $\Delta S_0^\circ = 0.079 \pm 0.013$ kcal mol⁻¹ K⁻¹. **(I)** Temperature dependent enthalpy, $\Delta H^\circ(T) = \Delta H_0^\circ + \Delta C_p(T - T_0)$, blue, and entropy, $-T\Delta S^\circ(T) = -T(\Delta S_0^\circ + \Delta C_p \ln(T/T_0))$, red, contributions to the change in free energy of CLC dimerization in 2:1 POPE/POPG membranes. Data represented as mean \pm standard deviation over 1000 bootstrapped values. **(J)** Comparison of thermodynamic contributions to CLC-ec1 dimerization stability in EPL vs. 2:1 POPE/POPG at 37 °C.

Estimation of the free energy of dimerization as a function of temperature shows a non-linear dependency, as was observed for the reaction in EPL, but now with the parabolic features more discernable (**Fig. 4F**). Plotting the data in van 't Hoff form and comparing with EPL, we find that both relationships are best fit to a non-linear model (**Fig. S5**) with similar shapes and mid-points, although the 2:1 POPE/POPG curve is shifted lower compared to EPL (**Fig. 4G**). The fitted thermodynamic parameters for CLC-ec1 dimerization in 2:1 POPE/POPG membranes yields $T_0 = 300.8 \pm 2.2$ K, $\Delta C_p = -1.7 \pm 0.3$ kcal mol⁻¹ K⁻¹ and $\Delta S_0^\circ = 0.078 \pm 0.013$ kcal mol⁻¹ K⁻¹, which are similar to the values measured for EPL, with a slight difference in the enthalpic contribution, $\Delta H_0^\circ = 12.0 \pm 3.8$ kcal mol⁻¹ (**Fig. 4H, Table S3**) and the temperature dependent relationship (**Fig. 4I**). These differences can be seen by decomposing ΔG° at a single temperature, 37 °C (i.e., 310 K), as a function of the lipid composition (**Fig. 4J**). While $\Delta G^\circ_{EPL}(37 \text{ }^\circ\text{C}) = -13.8 \pm 0.2$ kcal mol⁻¹, the enthalpic contribution is $\Delta H^\circ_{EPL}(37 \text{ }^\circ\text{C}) = -9.5 \pm 2.5$ kcal mol⁻¹ while $\Delta H^\circ_{PEPG}(37 \text{ }^\circ\text{C}) = -3.7 \pm 2.2$ kcal mol⁻¹ ($\Delta G^\circ_{PEPG}(37 \text{ }^\circ\text{C}) = -12.2 \pm 0.3$ kcal mol⁻¹). On the other hand, $-T\Delta S^\circ_{EPL}(37 \text{ }^\circ\text{C}) = -4.4 \pm 2.4$ kcal mol⁻¹ compared to $-T\Delta S^\circ_{PEPG}(37 \text{ }^\circ\text{C}) = -8.3 \pm 2.2$ kcal mol⁻¹. Thus, at the same temperature, the enthalpic vs. entropic contributions flip in these two lipid compositions. However, the free energy of dimerization is comparably stable and both reactions are characterized by a large and similar change in ΔC_p , indicating a common physical mechanism for dimerization stability that is linked predominantly to the heat capacity change.

4.6 Discussion

4.6.1 CLC dimerization is in a dynamic equilibrium in lipid membranes

Adding to our previous studies (4–8), the results presented here demonstrate that the large CLC-ec1 chloride/proton antiporter participates in a dynamic dimerization reaction inside of the lipid bilayer. This involves dissociation and re-association of the subunits inside the membrane all while maintaining functional transport activity. At the physiological condition of 37 °C, the heterodimeric FRET time-course exhibits a half-time to steady state at about 6 hours, indicating that the reaction is slow but dynamic. Slow kinetics of membrane protein association within membranes has been observed before, as indicated in steric-trapping studies of diacylglycerol kinase trimers (23) and glycophorin-A dimers (24, 25). Since subunit-exchange kinetics are dependent on the reaction association and dissociation rates, and other variables such as donor and acceptor stoichiometries (22), we reserve the quantitative analysis of the reaction kinetics for future study. Still, the observation of the exponentially increasing FRET signals and convergence to heterodimeric controls provides strong evidence that the FRET signal is reporting on the formation of heterodimers arising from dynamic subunit-exchange in the membrane, challenging the long-held presumption that CLC antiporters are obligatory complexes.

The evidence of dynamic assembly in membranes means that the probability of dimers is dependent on thermodynamically relevant parameters such as density of protein relative to lipid solvent, the composition of the lipid solvent, temperature, pressure, and chemical linkage. This means that the oligomerization is contextual and can redistribute in a regulatory manner inside of the membrane, even after dimers have formed. We observe this through lipid dependencies on the dimerization equilibrium, for example, as is observed when we switch the membrane composition to EPL from the synthetic mimic of 2:1 POPE/POPG, which stabilizes dimerization by about 2.3

kcal mol⁻¹ at room temperature, ≈ 22 °C. We have yet to identify the reason for this stabilizing effect but speculate that it is a factor particular to the native extract, such as an unexplored lipid component. Yet, the observation that this reaction can be shifted by lipids, and in the opposite direction of the effect of short-chain lipids that we observed previously (7), further demonstrates we are working with equilibrium reactions in the membrane where the membrane plays a role in defining the thermodynamic balance.

While quantitative stabilities are an absolute first step, to understand the thermodynamic forces involved, we must push the analysis further and dissect the change in free energy into changes in enthalpy and entropy. In aqueous solutions, this sort of dissection can be straightforward, as the direct heats of association can be measured by isothermal calorimetry. However, this approach is not possible for equilibrium association measurements within the membrane phase, as one cannot simply add membrane to the system and have it spontaneously incorporate with the pre-existing lipid bilayer. With this, the study of thermodynamic dissection of membrane protein association in lipid bilayers has been limited to only a few studies, where a temperature dependency of the free energy can be measured using a van 't Hoff analysis.

The first partial study of this sort was carried out for Gramicidin dimerization, a Na⁺-selective ion channel across the membrane that is formed by the association of two pentadecapeptides, one in each leaflet of the membrane (26). The probability of functional dimer formation is determined by the dynamic observation of electrical currents measured using single-channel bilayer electrophysiology. The temperature dependency of the dimerization was measured in dioleoyl-lecithin/n-decane at $T = 10, 25$ & 40 °C. However, these three points are not sufficient to confidently discriminate between different van 't Hoff models required for a full thermodynamic analysis.

The second study that has been reported involves the dimerization of poly-alanine/leucine transmembrane helix measured by the temperature dependency of FRET (27–29). This is a weak affinity dimer complex, and so the studies could be carried out using bulk FRET measurements, and more recently expanded to single-molecule FRET microscopy where dynamic dimer formation is readily observable. As far as we know, these sets of studies reflect the historical record of quantitative, temperature dependency measurements for assembly of membrane embedded proteins in membranes. Furthermore, the thermodynamic dissection of the free energy of CLC dimerization in membranes reveals itself to be the first large biological transport complex of a multi-helical folded protein where thermodynamic information can now be obtained and provides an essential next step to understanding the physical behavior of other biological membrane protein systems.

It is important to note that while our results indicate that we can measure the temperature dependency of this complex whilst in the membrane, this may not be experimentally accessible for all proteins. Because of the slow kinetics at ambient temperatures, we used a trick of incubating the system at higher temperatures, then locked in the oligomeric distribution by bringing the samples to room temperature where we could measure full dimerization isotherms using our single-molecule subunit-capture approach. Still, because many membrane protein complexes have been observed to be slow to dissociate (23), it may be possible to extend this measurement to other membrane protein systems.

4.6.2 Dimerization of CLC involves the observation of a large change in heat capacity

The van 't Hoff analysis for CLC dimerization in both EPL and 2:1 POPE/POPG lipid bilayers both show a non-linear temperature dependency. This suggests that the association of two

monomers into a dimer involves the appearance of a large negative change in heat capacity. There are multiple molecular explanations for this, and it is important to note that these are all observed thermodynamic parameters (ΔG°_{obs} , ΔH°_{obs} , ΔS°_{obs} , $\Delta C_{P,obs}$) until the molecular mechanism is identified. In the remainder of this discussion, we will provide a summary of some of these options and their likely participation in the mechanism of CLC dimerization.

The concept of a heat capacity change can be a difficult to consider for those outside of the field of protein self-assembly, but particularly in the study of membrane proteins since we have not many opportunities to consider data like this so far. Thus, it is worth some extra discussion here. In their book on biological thermodynamics, Dill & Bromberg simply state that the heat capacity “*describes the storage of energy (or enthalpy) in bonds that break or weaken with increasing temperature*” (2). To elaborate on this, heat energy that is applied to the sample is distributed into both kinetic and potential energy (30). The increase in kinetic energy results in faster velocities and therefore an increase in temperature. However, the heat energy can also be distributed into potential energy of the vibrations of molecular bonds. As a result, these interactions can be disrupted, allowing for increased rotational freedom without increasing the velocity of the molecule. Thus, systems that contain substantial networks of non-bonded interactions can possess a high heat capacity. A classic example of a substance with high molar heat capacity is water since it participates in an extensive hydrogen bonding network. Addition of heat changes the hydrogen bond distribution, weakening bonds and decreasing the order of molecules relative to each other. Consider the change in state of water from ice to liquid. A rough estimate of the melting of a protein-sized 30 Å ice crystal like a snowflake, is predicted to exhibit $\approx 5 \text{ kcal mol}^{-1} \text{ K}^{-1}$ change in heat capacity, resulting from only the changes in the network of hydrogen bonds (30).

With this, we go back and consider our observation that the change in heat capacity of CLC dimerization reaction is about -1.7 to -2.0 kcal mol⁻¹ K⁻¹, in both lipid compositions. This is a large value that is on the order of the upper limit of observed heat capacity changes observed for proteins, and comparable to the phase transition melting of a protein-sized ice crystal. What could be the molecular explanation for such a large heat capacity difference between the monomeric and dimeric states of CLC in membranes? For this we turn to our understanding of heat capacity changes in soluble protein self-assembly. Large changes in heat capacity have been observed to accompany significant changes in the exposure of non-polar groups to water, a phenomenon that is better known as the hydrophobic effect (31). The molecular explanation of this has been attributed to the unfolded or dissociated state, leading to exposure of non-polar surfaces to water. The surrounding first shell of waters cannot form hydrogen bonds with the non-polar groups, and therefore adopt highly organized solvation structures, often referred to as “icebergs” around these exposed surfaces. Addition of heat can be distributed into the remaining hydrogen bonds, weakening them to promote disordering of the water at the interface. The expected contribution from the hydrophobic effect can be predicted by measuring non-polar molecule partitioning into water. For example, benzene partitioning into water exhibits a heat capacity change of 0.27 cal mol⁻¹ K⁻¹ Å⁻² (32), and this value can be multiplied by the expected change in non-polar surface exposure to predict the heat capacity change between the dissociated/unfolded and associated/folded states (33). In general, these predictions agree well with experimental measurements for both protein folding and oligomerization in water, reaching heat capacity changes of -1 kcal mol⁻¹ K⁻¹. However, this value is considerably lower than what we observe for CLC dimerization in the membrane. To add to this, if we apply the same hydrophobic effect calculation to CLC, which exposes about 2400 Å² of its binding interface upon dissociation, we

only expect $\Delta C_p = -0.7 \text{ kcal mol}^{-1} \text{ K}^{-1}$ in the direction of association. It is reasonable to assume that this interface does not become exposed to water as it must remain membrane embedded to still function as a chloride transporter, and so the actual amount that is predicted to come from the hydrophobic effect must be much smaller. This therefore limits the contribution of the hydrophobic effect that could be attributed to exposure of the non-polar binding interface and instead points to other causes such as the surrounding solvent.

What types of solvent changes could account for such differences in molecular ordering? Our previous investigation into the changes in membrane structure around the monomeric and dimeric states of CLC provide some clues as to what may be conferring this anomalous heat capacity change (7). Extensive coarse-grained molecular dynamics simulations sampling lipids around the reaction endpoints, revealed that the membrane thins and twists to solvate the exposed dimerization interface in the monomeric state. This change in membrane shape arises from the favorable energetics of matching the membrane to the hydrophobic surface of the protein, however, it comes at a cost in terms of the total free energy of the system. But in the typical palmitoyl-oleoyl lipids that comprise EPL, these longer lipids cannot adequately pack in this region, resulting in significant lipid tilting, a reduction of local lipid packing and increased water penetration near the acyl chains (**Fig. S6**). Naturally, the partitioning of water into the membrane carries with it the hydrophobic effect, and further analysis of our previous coarse-grained molecular dynamics simulations (7) indicates that 5 water beads interact with C4 beads at the end of the lipid tails in the membrane defect per monomer compared to 2.5 water beads in a comparable area in the bulk lipid bilayer (**Table S4**). While these estimates are based on bead contacts and not necessarily penetration into the membrane, the average orientation of the lipids over the simulation indicates that this reflects, in part, burial of waters into the hydrophobic core that are removed

upon dimerization. The actual number of waters that become buried cannot be estimated by coarse-grained simulations directly, as each bead represents 4 atomic waters. Still, these results demonstrate that differential water partitioning near lipid chains occurs in the monomeric and dimeric states, and this would carry with it the energetic consequences of the hydrophobic effect. While the penetration of water in the membrane seems to be a likely candidate, we also must consider that there are other components to this, such as changes in the hydrogen bonding of lipid headgroups and even the strength of non-bonded van der Waals interactions. Since nearly 37 lipids are impacted around the dimerization interface (**Table S4**), we anticipate that the sum of smaller effects over many lipid and water molecules could account for the large change in heat capacity that is observed in our system.

Membrane dependent changes in heat capacity have been observed before, in another system where van 't Hoff analysis was carried out on an in-membrane dimerization reaction (27, 28). In this study, the dimerization free energy of a synthetic transmembrane helix (AALALAA)₃ was measured in C14 to C20 PC membranes exhibiting linear temperature dependencies. However, changing the lipid composition to the longer C22 lipids, which are hydrophobically mismatched to the dimer state, introduces a non-linear temperature dependency with a heat capacity change of +0.6 kcal mol⁻¹ K⁻¹ in the direction of dimerization. This implies that the monomeric state is more suitably solvated in the lipid bilayer, with the dimeric state ordering the solvent molecules in the system. The number of studies here are small, but both transmembrane helix dimerization and large CLC dimerization appear to have the capacity for changes in heat capacity linked to changes in solvent order factoring into the thermodynamic stability of dimerization within the membrane. Note the fact that both association reactions introduce non-linear temperature dependencies with large heat capacity changes suggests a potential mechanism

for temperature sensitivity that may be pertinent to other membrane protein reactions within the membrane (34).

Finally, there is another reason for observing a large change in heat capacity that may not actually involve any actual changes in heat capacity. This occurs when the reaction studied is coupled to another hidden equilibrium. For example, consider the possibility that the isolated monomer is in an equilibrium of two conformational states, M & M' :



Where $K_{MM'}$ is the equilibrium constant for the monomer conformational change, associated with an enthalpy change of $\Delta H_{MM'}$. With this linked equilibrium, the observed heat capacity decomposes into the actual heat capacity changes from both steps of the reaction, and a third term that does not depend on any heat capacity changes (35):

$$\Delta C_{P,obs} = \Delta C_{P,MD} + \frac{\Delta C_{P,MM'}}{1 + K_{MM'}} - \left(\frac{(\Delta H_{MM'})^2}{RT^2} \frac{K_{MM'}}{(1 + K_{MM'})^2} \right) \quad (8)$$

In this case, it is possible that the heat capacity change of the dimerization could be zero, $\Delta C_{P,MD} = 0$, as well as the heat capacity change for the conformational change, $\Delta C_{P,MM'} = 0$, but a non-linear temperature dependency of the free energy is still observed yielding an apparent heat capacity change that comes from the change in enthalpy of the linked reaction. This been observed before, for example, the binding of the tetrameric single-stranded DNA binding protein (SSB) from *E. coli* to oligodeoxyadenylates, which demonstrates a non-linear temperature dependency

with a large negative change in heat capacity, $\Delta C_{P,obs} \sim -0.5 \text{ kcal mol}^{-1} \text{ K}^{-1}$ (35, 36). Further examination demonstrates that the non-linearity in the van 't Hoff analysis arises because of the linkage of the binding to base stacking in the single-stranded DNA. As such, anomalously large changes in heat capacity are often observed in other DNA binding reactions, such as F Factor Relaxase to single-stranded DNA, which exhibits $\Delta C_P = -3.3 \text{ kcal mol}^{-1} \text{ K}^{-1}$ in the direction of binding (37), and is expected to be the result of both the hydrophobic effect but also base stacking. Relating these results back to CLC, it remains possible that the dimerization reaction is coupled to other hidden equilibria that we do not yet know about. For example, conformational changes of the monomer or different dimer complexes are plausible considerations and require further investigation to understand the full molecular mechanism. In addition, changes in the membrane state could also be linked to the dimerization reaction in this way. While our studies of the physical properties of EPL and 2:1 POPE/POPG over the investigated temperature range show no indication of structural or phase changes, this remains a possibility if studying the reaction in other compositions. Altogether, our main finding indicates that the CLC-ec1 dimerization reaction yields an anomalously large heat capacity change in both EPL and 2:1 POPE/POPG lipid bilayers, possibly larger than what the hydrophobic effect or other solvent ordering could provide, and so it supports the possibility that linkage to other hidden equilibria could also contribute to this striking observation.

4.7 Conclusion

This study demonstrates that CLC dimers are dynamic and reversible assemblies in the membrane, forming across a wide range of temperatures. This finding enables a rare thermodynamic analysis of the free energy for binding within the membrane by van 't Hoff

analysis. The results demonstrate that dimerization of the hydrophobic CLC interface is accompanied by an observed, large negative change in heat capacity, resembling the signature of the hydrophobic effect in driving soluble protein dimerization in water. Placing these results in context with previous computational work suggests that this heat capacity change could arise from the removal of a thinned membrane defect that is required to solvate the exposed dimerization interface in the monomeric state, which becomes buried upon binding. In addition, the magnitude of the change also suggests that dimerization reaction could be linked to some other hidden equilibrium, such as protein conformational changes. Finally, we find that the temperature dependency of CLC dimerization is pronounced, introducing a new model system for considering other temperature dependent reactions in the membrane such as ion channel gating.

4.8 Acknowledgments

The Robertson lab is supported by the National Institute of General Medical Science, National Institutes of Health (R01GM120260, R21GM126476). EGK acknowledges support from the Center for High Resolution Neutron Scattering, a partnership between the National Institute of Standards and Technology and the National Science Foundation under Agreement No. DMR-2010792. The identification of any commercial equipment does not imply recommendation or endorsement by NIST. The authors also thank the Australian Centre for Neutron Scattering (ACNS) for access to the SAXS instrument and Dr. Anna Sokolova and Dr. Andrew Whitten for their assistance with SAXS data collection and processing, and Tim Lohman, Chris Miller and the Robertson laboratory for useful discussions.

References

1. J. L. Popot, D. M. Engelman, Membrane protein folding and oligomerization: the two-stage model. *Biochemistry-us* **29**, 4031–4037 (1990).
2. K. A. Dill, S. Bromberg, D. Stigter, Molecular Driving Forces. 93–107 (2010).
3. J. L. Robertson, L. Kolmakova-Partensky, C. Miller, Design, function and structure of a monomeric ClC transporter. *Nature* **468**, 844–7 (2010).
4. R. Chadda, *et al.*, The dimerization equilibrium of a ClC Cl(-)/H(+) antiporter in lipid bilayers. *Elife* **5**, e17438 (2016).
5. R. Chadda, J. L. Robertson, Measuring Membrane Protein Dimerization Equilibrium in Lipid Bilayers by Single-Molecule Fluorescence Microscopy. *Methods Enzymol* **581**, 53–82 (2016).
6. R. Chadda, L. Cliff, M. Brimberry, J. L. Robertson, A model-free method for measuring dimerization free energies of CLC-ec1 in lipid bilayers. *J Gen Physiology* **150**, 355–365 (2018).
7. R. Chadda, *et al.*, Membrane transporter dimerization driven by differential lipid solvation energetics of dissociated and associated states. *Elife* **10**, e63288 (2021).
8. K. Mersch, T. N. Ozturk, K. Park, H.-H. Lim, J. L. Robertson, Altering CLC stoichiometry by reducing non-polar side-chains at the dimerization interface. *J Mol Biol* **433**, 166886 (2021).
9. M. Maduke, D. J. Pheasant, C. Miller, High-Level Expression, Functional Reconstitution, and Quaternary Structure of a Prokaryotic Clc-Type Chloride Channel. *J Gen Physiol* **114**, 713–722 (1999).
10. M. Walden, *et al.*, Uncoupling and Turnover in a Cl⁻/H⁺ Exchange Transporter. *J Gen Physiology* **129**, 317–329 (2007).
11. R. Dutzler, E. B. Campbell, M. Cadene, B. T. Chait, R. MacKinnon, X-ray structure of a ClC chloride channel at 3.0 Å reveals the molecular basis of anion selectivity. *Nature* **415**, 287–294 (2002).
12. K. G. Fleming, Standardizing the Free Energy Change of Transmembrane Helix–Helix Interactions. *J Mol Biol* **323**, 563–571 (2002).
13. P. D. Ross, S. Subramanian, Thermodynamics of protein association reactions: forces contributing to stability. *Biochemistry-us* **20**, 3096–3102 (1981).
14. W. Nguitragool, C. Miller, Uncoupling of a CLC Cl⁻/H⁺ Exchange Transporter by Polyatomic Anions. *J Mol Biol* **362**, 682–690 (2006).

15. G. F. White, K. I. Racher, A. Lipski, F. R. Hallett, J. M. Wood, Physical properties of liposomes and proteoliposomes prepared from Escherichia coli polar lipids. *Biochimica Et Biophysica Acta Bba - Biomembr* **1468**, 175–186 (2000).
16. B. P. Navas, *et al.*, Composition dependence of vesicle morphology and mixing properties in a bacterial model membrane system. *Biochimica Et Biophysica Acta Bba - Biomembr* **1716**, 40–48 (2005).
17. M. B. Jackson, J. E. Cronan, An estimate of the minimum amount of fluid lipid required for the growth of escherichia coli. *Biochimica Et Biophysica Acta Bba - Biomembr* **512**, 472–479 (1978).
18. H. Nakayama, T. Mitsui, M. Nishihara, M. Kito, Relation between growth temperature of E. coli and phase transition temperatures of its cytoplasmic and outer membranes. *Biochimica Et Biophysica Acta Bba - Biomembr* **601**, 1–10 (1980).
19. S. Morein, A.-S. Andersson, L. Rilfors, G. Lindblom, Wild-type Escherichia coli Cells Regulate the Membrane Lipid Composition in a “Window” between Gel and Non-lamellar Structures (*). *J. Biol. Chem.* **271**, 6801–6809 (1996).
20. L. Cliff, R. Chadda, J. L. Robertson, Occupancy distributions of membrane proteins in heterogeneous liposome populations. *Biochimica Et Biophysica Acta Biomembr* **1862**, 183033 (2019).
21. N. Kučerka, J. Pencer, J. N. Sachs, J. F. Nagle, J. Katsaras, Curvature Effect on the Structure of Phospholipid Bilayers. *Langmuir* **23**, 1292–1299 (2007).
22. D. Goulet, Modeling, Simulating, and Parameter Fitting of Biochemical Kinetic Experiments. *Siam Rev* **58**, 331–353 (2016).
23. R. E. Jefferson, T. M. Blois, J. U. Bowie, Membrane Proteins Can Have High Kinetic Stability. *J Am Chem Soc* **135**, 15183–15190 (2013).
24. L. E. Fisher, D. M. Engelman, J. N. Sturgis, Detergents modulate dimerization, but not helicity, of the glycophorin A transmembrane domain 11 Edited by G. von Heijne. *J Mol Biol* **293**, 639–651 (1999).
25. H. Hong, T. M. Blois, Z. Cao, J. U. Bowie, Method to measure strong protein–protein interactions in lipid bilayers using a steric trap. *Proc National Acad Sci* **107**, 19802–19807 (2010).
26. E. Bamberg, P. Läuger, Temperature-dependent properties of gramicidin A channels. *Biochimica Et Biophysica Acta Bba - Biomembr* **367**, 127–133 (1974).
27. Y. Yano, K. Matsuzaki, Measurement of Thermodynamic Parameters for Hydrophobic Mismatch 1: Self-Association of a Transmembrane Helix †. *Biochemistry-us* **45**, 3370–3378 (2006).

28. Y. Yano, A. Yamamoto, M. Ogura, K. Matsuzaki, Thermodynamics of insertion and self-association of a transmembrane helix: a lipophobic interaction by phosphatidylethanolamine. *Biochemistry-us* **50**, 6806–14 (2011).
29. Y. Yano, Y. Watanabe, K. Matsuzaki, Thermodynamic and kinetic stabilities of transmembrane helix bundles as revealed by single-pair FRET analysis: Effects of the number of membrane-spanning segments and cholesterol. *Biochimica Et Biophysica Acta Bba - Biomembr* **1863**, 183532 (2021).
30. A. Cooper, Heat capacity effects in protein folding and ligand binding: a re-evaluation of the role of water in biomolecular thermodynamics. *Biophys Chem* **115**, 89–97 (2005).
31. C. Tanford, How protein chemists learned about the hydrophobic factor. *Protein Sci* **6**, 1358–1366 (1997).
32. P. L. Privalov, S. J. Gill, Stability of Protein Structure and Hydrophobic Interaction. *Adv Protein Chem* **39**, 191–234 (1988).
33. P. R. Connelly, J. A. Thomson, Heat capacity changes and hydrophobic interactions in the binding of FK506 and rapamycin to the FK506 binding protein. *Proc National Acad Sci* **89**, 4781–4785 (1992).
34. D. E. Clapham, C. Miller, A thermodynamic framework for understanding temperature sensing by transient receptor potential (TRP) channels. *P Natl Acad Sci Usa* **108**, 19492–7 (2011).
35. M. E. Ferrari, T. M. Lohman, Apparent Heat Capacity Change Accompanying a Nonspecific Protein-DNA Interaction. Escherichia coli SSB Tetramer Binding to Oligodeoxyadenylates. *Biochemistry* **33**, 12896–12910 (1994).
36. A. G. Kozlov, T. M. Lohman, Adenine base unstacking dominates the observed enthalpy and heat capacity changes for the Escherichia coli SSB tetramer binding to single-stranded oligoadenylates. *Biochemistry* **38**, 7388–97 (1999).
37. J. C. Stern, B. J. Anderson, T. J. Owens, J. F. Schildbach, Energetics of the Sequence-specific Binding of Single-stranded DNA by the F Factor Relaxase Domain*. *J Biol Chem* **279**, 29155–29159 (2004).
38. L. J. Friedman, J. Gelles, Multi-wavelength single-molecule fluorescence analysis of transcription mechanisms. *Methods San Diego Calif* **86**, 27–36 (2015).
39. M. Ernst, T. N. Ozturk, J. L. Robertson, A single-molecule method for measuring fluorophore labeling yields for the study of membrane protein oligomerization in membranes. *Plos One* **18**, e0280693 (2023).

Supporting Information

S4.1 Appendix

S4.1.1 Quantification of protein/fluorophore labeling yields

The protein concentration in the presence of Cy5 (or Cyanine 5) is calculated as:

$$[protein_{Cy5}] = \frac{A_{280} - (A_{Cy5,max} \times CF_{Cy5,280})}{\epsilon_{protein}} \quad (S1)$$

where A_{280} is the absorbance at 280 nm, $A_{Cy5,max}$ is the peak absorbance of Cy5 \approx 653 nm, $CF_{Cy5,280} = 0.017$ ($CF_{Cy5,280} = 0.05$ for Cyanine 5), is the correction factor for the absorbance of Cy5 at 280 nm, and $\epsilon_{protein}$ is the extinction coefficient for the protein at 280 nm. The subunit labeling yield, P_{Cy5} , is calculated as:

$$P_{Cy5} = \frac{A_{Cy5,max}}{[protein_{Cy5}] \times \epsilon_{Cy5}} \quad (S2)$$

where, $\epsilon_{Cy5} = 2.5 \times 10^5 \text{ M}^{-1} \text{ cm}^{-1}$ is the extinction coefficient for Cy5 at 653 nm. For the Förster resonance energy transfer (FRET) studies, protein was labeled with Cy3-maleimide (Lumiprobe) or simultaneously co-labeled with Cy3- and Cy5-maleimide. For Cy3-labeling alone, the same procedure was followed, except that the quantification is corrected for Cy3 contribution at 280 nm. Thus, the protein concentration in the presence of Cy3 is calculated as:

$$[protein_{Cy3}] = \frac{A_{280} - (A_{Cy3,max} \times CF_{Cy3,280})}{\epsilon_{protein}} \quad (S3)$$

where $A_{Cy3,max}$ is the peak absorbance of Cy3 ≈ 555 nm, and $CF_{Cy3,280} = 0.08$ is the correction factor for the absorbance of Cy3 at 280 nm. The subunit labeling yield, P_{Cy3} , is calculated as:

$$P_{Cy3} = \frac{A_{Cy3,max}}{[protein_{Cy3}] \times \epsilon_{Cy3}} \quad (S4)$$

where, $\epsilon_{Cy3} = 1.5 \times 10^5 \text{ M}^{-1} \text{ cm}^{-1}$ is the extinction coefficient for Cy3 at 555 nm. For labeling of Cy3 and Cy5 simultaneously, there are two correction factors to consider, Cy3 and Cy5 absorbance at 280, as well as the contribution of Cy5 absorbance in the Cy3 peak. Thus, the protein concentration in the presence of Cy3 and Cy5 is calculated as:

$$[protein_{Cy3/Cy5}] = \frac{A_{280} - ((A_{Cy3,max} - (A_{Cy5,max} \times CF_{Cy5,555})) \times CF_{Cy3,280}) - (A_{Cy5,max} \times CF_{Cy5,280})}{\epsilon_{protein}} \quad (S5)$$

where $CF_{Cy3,555} = 0.08$ is the correction factor for the absorbance of Cy5 around the Cy3 peak.

The subunit labeling yield of Cy3 in the presence of Cy5, $P_{Cy3:Cy5}$, is calculated as:

$$P_{Cy3/Cy5} = \frac{(A_{Cy3,max} - (A_{Cy5,max} \times CF_{Cy5,555}))}{[protein_{Cy3/Cy5}] \times \epsilon_{Cy3}} \quad (S6)$$

and the subunit labeling yield of Cy5 in the presence of Cy3, $P_{Cy5:Cy3}$, is calculated as:

$$P_{Cy5/Cy3} = \frac{A_{Cy5,max}}{[protein_{Cy3/Cy5}] \times \epsilon_{Cy5}} \quad (S7)$$

Altogether, we obtained the following Cy5, Cy3, and co-labeled Cy3/5 labeling yields for WT CLC-ec1: $P_{Cy5} = 0.72 \pm 0.01$ (n = 9), $P_{Cy3} = 0.79 \pm 0.01$ (n = 9), $P_{Cy5}/P_{Cy3} = 6.0 \pm 0.4$ (n = 8) (P_{Cy3}

= 0.11 ± 0.01 , $P_{Cy5} = 0.63 \pm 0.02$, respectively). For RCLC CLC-ec1, we obtained the following Cy5, Cy3, and co-labeled Cy3/5 labeling yields: $P_{Cy5} = 0.71 \pm 0.01$ (n = 6), $P_{Cy3} = 0.73 \pm 0.05$ (n = 6), $P_{Cy5}/P_{Cy3} = 4.8 \pm 0.4$ (n = 6) ($P_{Cy3} = 0.13 \pm 0.01$, $P_{Cy5} = 0.63 \pm 0.02$, respectively).

S4.1.2 Differential Scanning Calorimetry (DSC)

DSC data were collected using a MicroCal VP-DSC differential scanning calorimeter. Samples were degassed at room temperature prior to measurement, and data were collected with different heating and cooling rates to ensure that the scan rate did not impact the transition temperature. The presented data are for the second heating from 0.5 °C to 100 °C with a scan rate of 30 °C/h. The sample data were corrected for the buffer baseline using the software provided with the instrument. Lipid concentrations were measured by phosphate quantification as described previously (4), with [EPL] = 15.1 mM, [0.67 POPE/ 0.33 POPG] = 13.1 mM and [0.67 POPE/0.23 POPG/0.1 CL] = 12.9 mM. Buffer conditions were the same as in all other experiments: 300 mM KCl, 20 mM citrate, pH 4.5.

S4.1.3 Bulk FRET measurements in PLVs – membrane fusion

Membrane fusion studies were carried out at ambient room temperature following a similar procedure, where 0.02% PE-NBD (donor), 0.1% PE-RhB (acceptor), or both, 0.02% PE-NBD/0.1% PE-RhB, were added to the lipid mixtures during reconstitution. Excitation and emission wavelengths were adjusted for NBD excitation and RhB detection.

S4.1.4 Small angle x-ray scattering (SAXS)

SAXS data were collected on a Xeuss3.0 SAXS instrument at the Australian Centre for Neutron Scattering (ACNS). Measurements were performed using an X-ray wavelength (λ) of 1.42

Å (Cu K α) and a fixed sample to detector distance to collect data over a q -range of approximately $0.01 \text{ \AA}^{-1} < q < 0.3 \text{ \AA}^{-1}$, where $q = 4\pi/\lambda \sin(\theta/2)$ and θ is the scattering angle. Samples were loaded into 1.5 mm disposable quartz capillaries for the measurements. The temperature was controlled using a Peltier block, and the samples were allowed to equilibrate for 15 min at each temperature before beginning data collection. Data was collected in 15-minute frames for a total acquisition time of 1 hour. Each two-dimensional detector image was radially averaged in the Software provided with the instrument and then individually assessed for beam damage. No evidence of beam damage was seen. Background scattering from the buffer was also collected at each temperature, and the averaged one-dimensional curve from the background was subtracted from the corresponding samples. The one-dimensional curves, $I(q)$, were fit as:

$$I(q) = P(q)S(q) \quad (\text{S8})$$

In which $P(q)$ is the form factor model for a single bilayer and $S(q)$ is the lamellar structure factor. The bilayer was assumed to be symmetric and fit with a form factor that described the bilayer density as the sum of three Gaussians in which one Gaussian described the inner headgroup layer, one Gaussian was for the terminal methyl trough, and one Gaussian for the outer headgroup layer. The Gaussians describing the outer and inner headgroup layers were equivalent (38),

$$P(q) = \frac{2\pi}{q^2} \left(\sum_{i=1}^3 (\rho_i - \rho_b) d_i \exp(-d_i^2 q^2 / 2) \right. \\ \left. \times \{d_i^2 q \cos[q(R + X_i)] + (R + X_i) \sin[q(R + X_i)]\} \right)^2 \quad (\text{S9})$$

in which ρ_i corresponds to the scattering length density of the corresponding layer, ρ_b is the scattering length density of the buffer, X_i is the distance of the corresponding layer from the vesicle center, d_i is the width of the corresponding Gaussian, and R is the vesicle radius. The value of R was fixed as 100 nm during the fits based on previously published cryo TEM images of freeze-thawed vesicles that showed on average $\gg 100$ nm (20) and changing the value of R did not affect the fit results. The widths of the Gaussians for the inner and outer headgroups were fixed at $d_1 = d_3 = 2.8 \text{ \AA}$ to be consistent with previous results in literature (39). The distance between the two headgroup peaks, X_1 and X_3 , is presented phosphate-to-phosphate thickness of the bilayer (d_{PO_4}).

To account for the distribution of lamellae in the freeze-thawed samples, the data were fit with a lamellar structure factor assuming a modified exponential distribution of layers, N , as described by Scott et al. (39),

$$w_N(\Lambda) = \begin{cases} w_1 & N = 1 \\ e^{-\Lambda N} & N > 1 \end{cases} \quad (\text{S10})$$

Where Λ is the distribution parameter and is inversely related to the average number of lamellae and w_1 is the relative probability of a vesicle being unilamellar ($N = 1$). The ensemble averaged structure factor was calculated as

$$\langle S(q) \rangle = \frac{\sum_{N=1}^{N_{\max}} S_N(q) w_N(\Lambda)}{\sum_{N=1}^{N_{\max}} w_N(\Lambda)} \quad (\text{S11})$$

Where the sum is truncated at $N_{max} = [-\log(1-p)/\Lambda]$ and $p = 0.999$ was taken as the cumulative probability cutoff and $S_N(q)$ is the lamellar structure factor given by

$$S_N(q) = N + 2 \sum_{k=1}^{N-1} (N-k) \cos(kqd) \exp[-(dq/2\pi)^2 \eta \{\gamma + \ln(\pi k)\}] \quad (\text{S12})$$

Here, d is the interlamellar spacing and $d = m2\pi/q_m$ (for $m = 1,2,3\dots$) where q_m is the q-value of the primary peak in the SAXS data, γ is Euler's constant and η is the Caille parameter related to the bilayer undulations and bulk modulus of the membranes. The data were fit in Igor Pro using macros provided by NIST (40) and the Levenberg-Marquardt algorithm. The error bars are the associated uncertainties in the fit parameters.

S4.1.5 Calculation of waters in the membrane

The number of water beads associated with the membrane was analyzed for the entire coarse-grained MARTINI 2.2 molecular dynamics simulation of the CLC-ec1 monomer in 2:1 POPE/POPG as presented in (6), including 8 simulation replicates with durations of $\approx 7.5 \mu\text{s}$ each for a total combined trajectory of $60 \mu\text{s}$. Water molecules within the membrane are identified based on the presence of contacts with lipid molecules. For all-atom models, the depth of water penetration can be profiled by noting the number of hydrogen bonds formed with other waters and lipid-water contacts. However, this analysis is not possible for coarse-grained simulations as a single bead is a coarse-grained representation of 4 water molecules with no further spatial definition. Thus, our analysis relies on contact analysis alone with each lipid bead type: headgroup, phosphate, esters, and C1-C4 alkyl groups (**Fig. S6A**). Examination of the mean lipid coordinates (**Fig. S6B**) shows that these groups provide a crude indicator of the minimum bilayer depth reached

by the water molecules. With these groups defined, lipid-water contacts are counted using a distance threshold of 6 Å, as this distance lies close to the potential energy minimum derived from the Lennard Jones interactions for most MARTINI bead pairs. Once identified, each membrane water stamps a normalized density or a value of unity to nearby lattice points. This latter case is used to derive a map of the average number of water molecules residing in the membrane for each lattice point (**Fig. S6C**). In contrast, the former choice produces a map that can be used to count waters in a subset of the membrane, like at the dimerization interface or a region in the bulk. The average number of these waters is determined by integrating over lattice points, where the selection is defined using a lattice mask. Lipid numbers were calculated for the same masked membrane areas using the membrane analysis program MOSAICS (7). The area of the membrane defect, lipid numbers and water numbers are provided in **Table S4**.

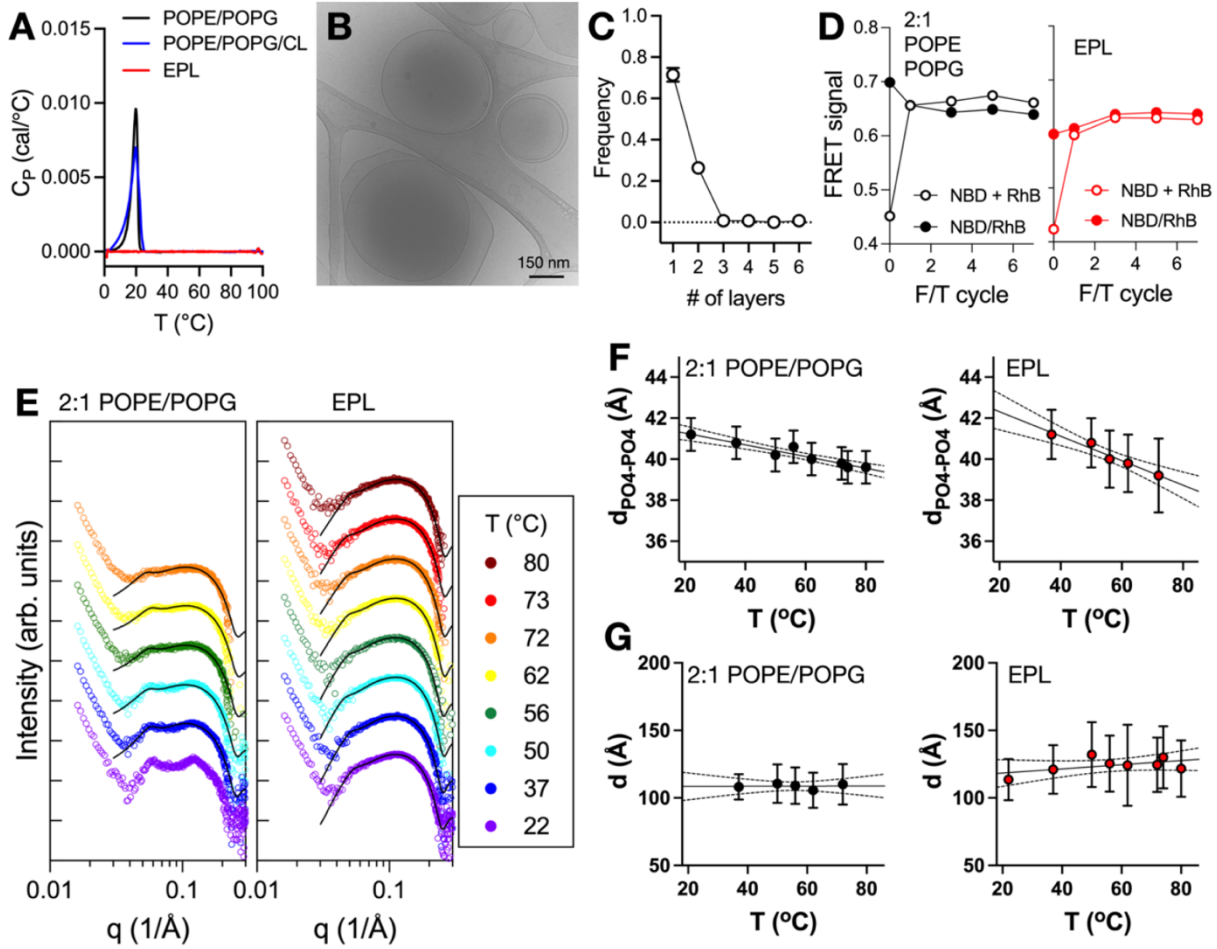


Fig. S1. Membrane properties of EPL and 2:1 POPE/POPG PLVs. All studies are in H₂O buffer conditions with 300 mM KCl, 20 mM citrate, pH 4.5. **(A)** Differential scanning calorimetry of EPL, 0.67 POPE/0.33 POPG and 0.67 POPE/0.23 POPG/0.10 bovine cardiolipin. **(B)** Cryo-EM images of freeze/thawed 2:1 POPE/POPG vesicles adapted from **(2)**. **(C)** Frequency plot of number of lamella in 2:1 POPE/POPG PLVs from cryo-EM image analysis. **(D)** 2:1 POPE/POPG and EPL membrane fusion studies monitoring FRET from mixing of donor PE-NBD and acceptor PE-RhB. **(E)** SAXS curves and fits to a combined model for a single bilayer form factor and lamellar structure factor for 2:1 POPE/POPG and EPL PLVs. **(F)** Plot of phosphate-phosphate distance for 2:1 POPE/POPG and EPL, with lines representing fits to $d_{PO4-PO4} = m \cdot T + b$: $m_{PEPG} = -0.0597 \pm 0.0074 \text{ \AA}/^\circ\text{C}$, $b_{PEPG} = 43.5 \pm 0.4 \text{ \AA}$, $m_{EPL} = -0.0286 \pm 0.0035 \text{ \AA}/^\circ\text{C}$, $b_{EPL} = 41.84 \pm 0.2 \text{ \AA}$, and **(G)** interlamellar spacing for 2:1 POPE/POPG and EPL, with lines representing fits to $d = m \cdot T + b$: $m_{PEPG} = 0.0045 \pm 0.0874 \text{ \AA}/^\circ\text{C}$, $b_{PEPG} = 108.5 \pm 4.8 \text{ \AA}$, $m_{EPL} = 0.1541 \pm 0.0983 \text{ \AA}/^\circ\text{C}$, $b_{EPL} = 115.3 \pm 5.857 \text{ \AA}$. Data represented as best-fit \pm standard error of fit.

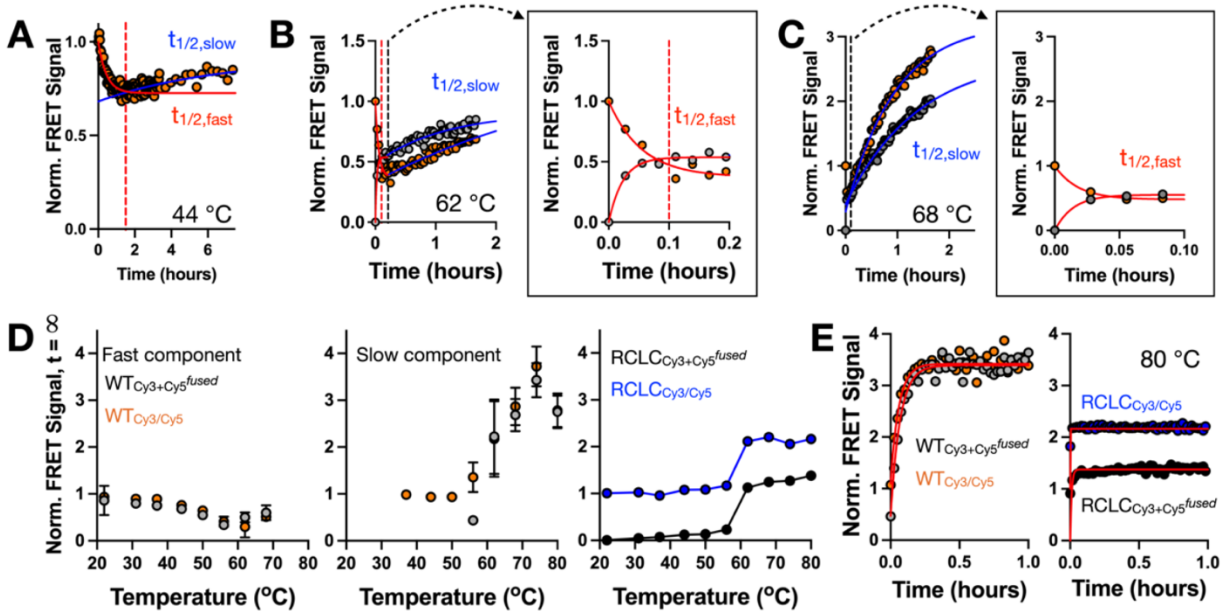


Fig. S2. Two-component FRET kinetics in CLC subunit-exchange. (A) Example of two-component FRET kinetics observed in a 44 °C time-course for WT_{Cy3/Cy5}. Fast and slow components, labeled $t_{1/2,fast}$ (red) and $t_{1/2,slow}$ (blue), respectively. Dashed red line indicates cutoff for the fitting. (B) Example of two-component FRET kinetics observed in a 62 °C time-course for both WT_{Cy3+Cy5^{fused}} (grey) and WT_{Cy3/Cy5} (orange). Box shows a zoomed in region marked by the dashed black line, revealing the fast component of the data, including a decay in the WT_{Cy3/Cy5} FRET signal before the slow increase. (C) Example of two-component FRET kinetics observed in a 68 °C time-course for both WT_{Cy3+Cy5^{fused}} (grey) and WT_{Cy3/Cy5} (orange), with the box highlighting the zoomed in region showing the fast component. Summary of the plateau/endpoint estimates for the (D) fast and slow components of the WT samples and RCLC samples. (E) Traces of WT and RCLC at 80 °C, showing differences in the plateau behavior in the different samples. Data represented as mean \pm SEM, $n = 1-5$.

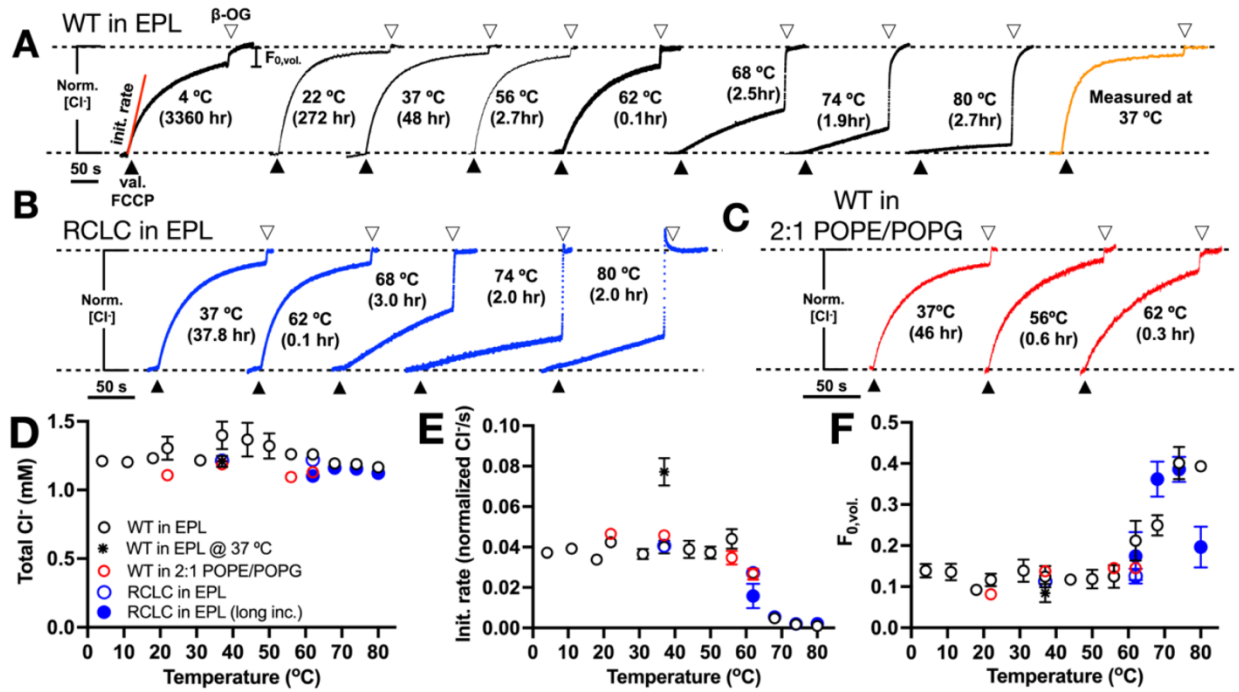


Fig. S3. CLC-ec1 chloride transport after incubation at different temperatures. (A) Representative chloride efflux traces of Cy3 and/or Cy5 labeled WT CLC-ec1 in EPL (black), (B) Cy3 and/or Cy5 labeled RCLC CLC-ec1 in EPL (blue) and (C) Cy3 and/or Cy5 labeled WT CLC-ec1 in 2:1 POPE/POPG liposomes (red). Black triangle indicates the addition of valinomycin and FCCP, white triangle indicates the addition of β -octyl-glucoside (β -OG). For all traces, the samples were incubated for the noted temperature and time and then measured at room temperature, except the orange trace, which was measured directly at 37 °C. For all experiments, protein was reconstituted at $\chi = 1 \times 10^{-5}$ subunits/lipid, i.e., 1 μ g/mg. (D) Total Cl⁻ concentration in the measurement cell after addition of β -OG, (E) initial chloride transport rate and (F) fractional volume of inactive vesicles, $F_{0,vol.}$. All samples were measured at the minimum time required for equilibration of subunit exchange (Fig. 2 & 4), except for the long incubation samples (RCLC, blue filled circles), which were measured at extended incubation times (62 °C measured at 0.3 hours). Statistics tests were carried out comparing with 22 °C or 37 °C data using the unpaired parametric student's t-test. For WT in EPL, transport activity was measured after incubation 38.7 ± 4.3 h at 37 °C, 0.1 ± 0 h at 62 °C, 3.0 ± 0 h at 62 °C, 3.0 ± 0 h at 68 °C, 2.0 ± 0 h at 74 °C, and 2.0 ± 0 h at 80 °C (mean \pm SEM, n = 2-4).

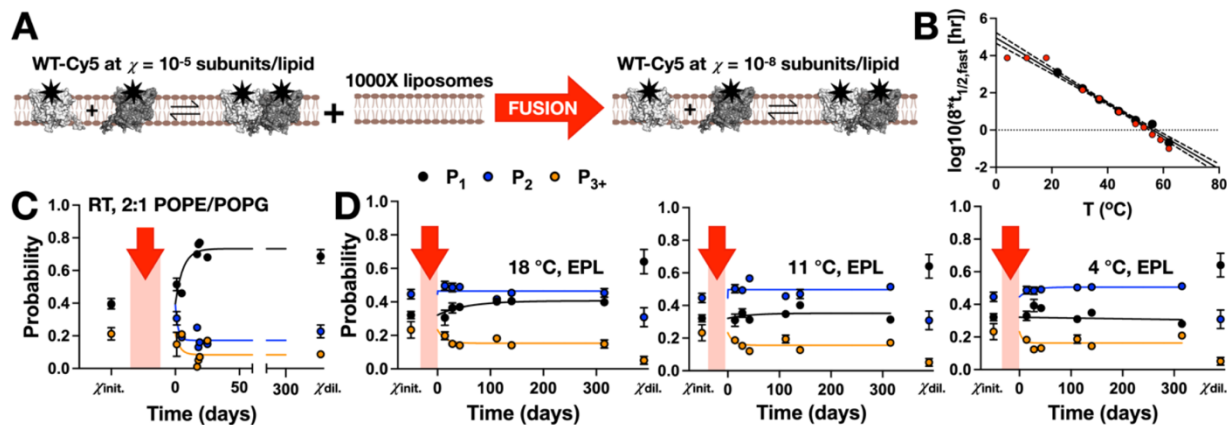


Fig. S4. Lack of evidence of CLC-ec1 dimerization equilibration in EPL at temperatures below room temperature. (A) Schematic of the in-membrane dilution studies. Dimeric WT-Cy5 reconstituted at $\chi_{rec.} = 10^{-5}$ subunits/lipid is diluted 1000-fold, to $\chi = 10^{-8}$ subunits/lipid by freeze/thaw fusion with empty vesicles and then incubated at room temperature or lower to monitor the relaxation time-course. (B) Predicted incubation times $8 \times t_{1/2}$ from the subunit exchange kinetics, black, and actual incubations times in red. (C) Photobleaching step probabilities - P_1 , P_2 & P_{3+} as a function of time for WT-Cy5 in 2:1 POPE/POPG at room temperature, RT ≈ 22 °C adapted from (5), and (D) WT-Cy5 in EPL at 18 °C, 11 °C and 4 °C. $\chi_{init.}$ corresponds to samples reconstituted at $\chi_{rec.} = 10^{-6}$ subunits/lipid and removing the instantaneous dilution effect from multi-occupied vesicles, and $\chi_{dil.}$ corresponds to the expected final dilution reconstituted at $\chi_{rec.} = 10^{-8}$ subunits/lipid, both at RT. The red arrow indicates the dilution by freeze/thaw fusion. Data represented as mean \pm SEM, $n = 2-3$.

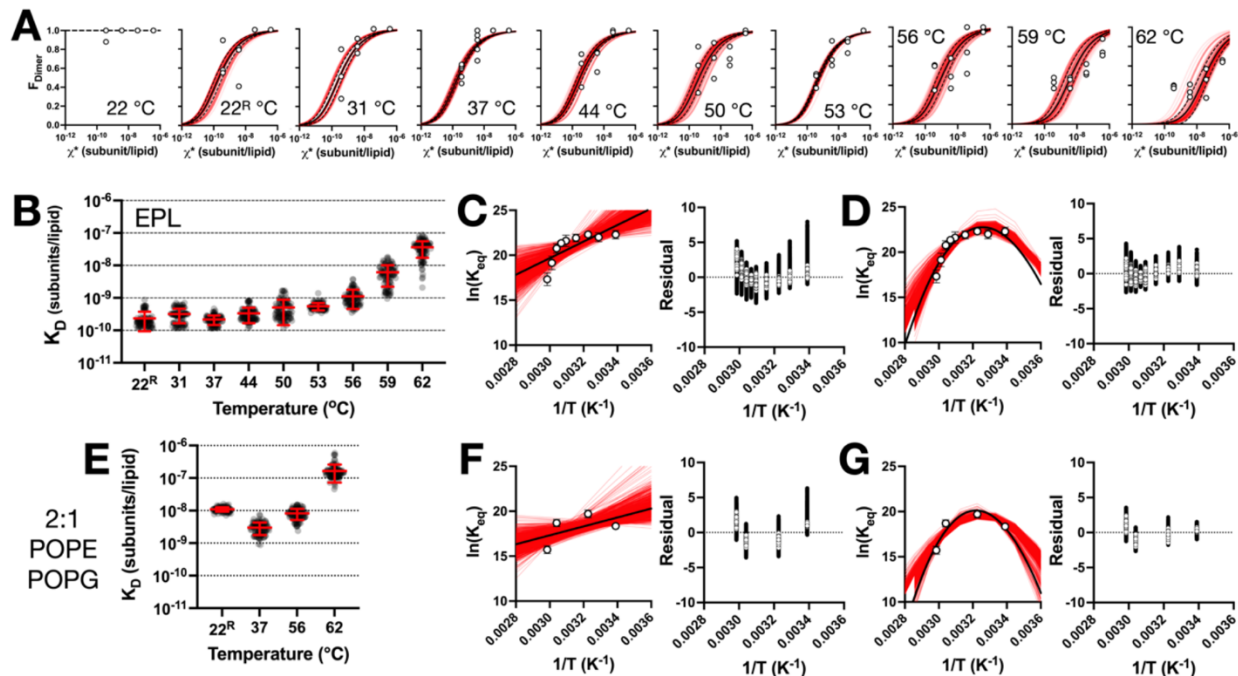


Fig. S5. Analysis of temperature dependency van 't Hoff data. (A) CLC-ec1 dimerization data in EPL, including 22 °C diluted samples before equilibration, 22^R °C reconstituted samples, and incubation of the original 22 °C diluted samples at the noted temperature yielding the equilibrated isotherms. **(B)** Bootstrap distributions of the dissociation constant, K_D (subunits/lipid) as a function of temperature. 22^R °C sample from (5, 8). **(C)** Bootstrap fitting of the van 't Hoff plots fit with a linear model (red lines) and residuals, and **(D)** non-linear function (red lines) with residuals. The black lines indicate the direct fit of the mean data. **(E)** Dissociation constant distributions of CLC-ec1 dimerization in 2:1 POPE/POPG with van 't Hoff form data fit to **(F)** the linear and **(G)** non-linear models.

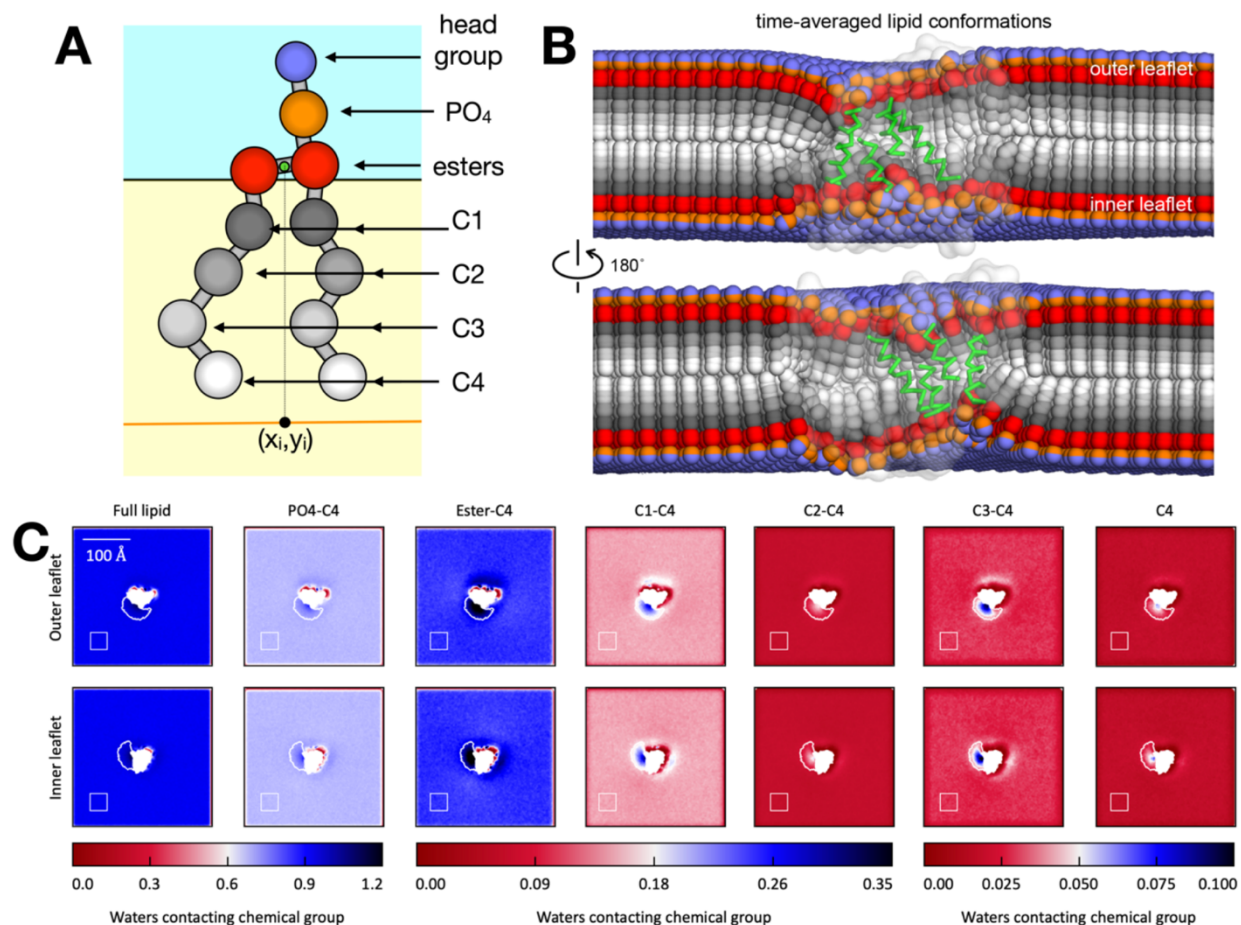


Fig. S6. The number of water molecules associated with the membrane in the monomeric state of CLC-ec1. (A) MARTINI bead types for POPE and POPG lipids. **(B)** Spatial variation of time average atomic coordinates for POPE and POPG molecules over 60 μ s of coarse-grained MARTINI 2.2 molecular dynamics simulations of CLC-ec1 in the monomeric state (shaded structure), as reported in (6). Due to isotropic dynamics, these coordinates appear as linear structures, with the individual bead types occupying a distinct band within the membrane interior. A defect in the bilayer structure is evident at the dimerization interface (green helices) with significant lipid tilting and reduction in lipid packing density. **(C)** The average number of water molecules associated with varying depths within the membrane, where the minimum depth reached is loosely correlated with the indicated lipid chemical group (Table S4). These groups are built from the groups defined in (B) and are reduced in size when moving from the full lipid on the left to the C₄ group on the right. A white outline at the dimerization interface indicates regions integrated over when counting lipids, while another region corresponding to a similar area of bulk membrane is also shown as a white square in the lower left corner of each map.

Table S1. Structural properties of lipid bilayers measured by SAXS. Membranes were studied in the freeze-thawed large, paucilamellar state in 300 mM KCl, 20 mM citrate, pH 4.5.

Temp. (°C)	EPL		2:1 POPE/POPG	
	d _{PO4-PO4} (Å)	d (Å)	d _{PO4-PO4} (Å)	d (Å)
22	41.2 ± 0.8	113.6 ± 15.3		
37	40.8 ± 0.8	121.1 ± 18.0	41.2 ± 1.2	108.2 ± 9.4
50	40.2 ± 0.8	132.0 ± 24.0	40.8 ± 1.2	110.5 ± 14.3
56	40.6 ± 0.8	125.4 ± 20.8	40.0 ± 1.4	109.0 ± 13.5
62	40.0 ± 0.8	124.2 ± 30.0	39.8 ± 1.4	105.7 ± 13.0
72	39.8 ± 0.8	124.5 ± 20.2	39.2 ± 1.8	110.1 ± 15.0
74	39.6 ± 0.8	130.0 ± 23.1		
80	39.6 ± 0.8	121.7 ± 20.9		

Table S2. Observed K_D , K_{eq} and ΔG° values for temperature dependent CLC-ec1 dimerization equilibrium in lipid bilayers. K_D and K_{eq} estimates obtained from bootstrap fitting of the dimerization isotherm to F_{Dimer} vs. χ^* data for CLC-ec1 in EPL or 2:1 POPE/POPG (PEPG) from single molecule photobleaching experiments, reported as mean \pm standard deviation from 100 fits. $\Delta G^\circ = -RT \ln(K_{eq} \chi^\circ)$ where $\chi^\circ = 1$ subunit/lipid, the mole fraction standard state. 22^R indicates samples where the density was set during reconstitution and then measured at 22 °C. 2:1 POPE/POPG 22^R data is re-fitted from (8).

Temperature (°C)	Lipid	K_D (subunits/lipid)	K_{eq} (lipids/subunit)	ΔG° (kcal/mole)
22 ^R	EPL	$2.3 \pm 1.4 \times 10^{-10}$	$5.3 \pm 1.9 \times 10^9$	-13.1 ± 0.3
31	EPL	$3.2 \pm 1.5 \times 10^{-10}$	$4.0 \pm 2.1 \times 10^9$	-13.4 ± 0.3
37	EPL	$2.2 \pm 0.7 \times 10^{-10}$	$5.1 \pm 1.6 \times 10^9$	-13.8 ± 0.2
44	EPL	$3.3 \pm 1.6 \times 10^{-10}$	$3.6 \pm 1.4 \times 10^9$	-13.8 ± 0.3
50	EPL	$5.1 \pm 3.7 \times 10^{-10}$	$2.9 \pm 1.6 \times 10^9$	-13.9 ± 0.4
53	EPL	$5.5 \pm 1.4 \times 10^{-10}$	$1.9 \pm 0.4 \times 10^9$	-13.8 ± 0.1
56	EPL	$1.1 \pm 0.7 \times 10^{-9}$	$1.2 \pm 0.6 \times 10^9$	-13.6 ± 0.3
59	EPL	$6.2 \pm 4.0 \times 10^{-9}$	$2.7 \pm 2.3 \times 10^8$	-12.6 ± 0.5
62	EPL	$3.6 \pm 1.9 \times 10^{-8}$	$4.6 \pm 6.0 \times 10^7$	-11.5 ± 0.5
22 ^R	PEPG	$1.1 \pm 0.2 \times 10^{-8}$	$9.3 \pm 1.5 \times 10^7$	-10.8 ± 0.1
37	PEPG	$3.0 \pm 1.2 \times 10^{-9}$	$4.0 \pm 1.8 \times 10^8$	-12.2 ± 0.3
56	PEPG	$8.2 \pm 3.1 \times 10^{-9}$	$1.4 \pm 0.6 \times 10^8$	-12.2 ± 0.3
62	PEPG	$1.7 \pm 0.9 \times 10^{-7}$	$7.3 \pm 3.1 \times 10^6$	-10.5 ± 0.3

Table S3. Thermodynamic parameters from non-linear and linear van 't Hoff fits. Parameter estimates obtained from bootstrap fitting of $\ln(K_{eq})$ vs. $1/T$ data to either the non-linear van 't Hoff equation: $\ln(K_{eq} \cdot \chi^\circ) = -\Delta H_0^\circ/RT - \Delta C_p(1 - T_0/T)/R + \Delta S_0^\circ/R - (\Delta C_p/R)\ln(T_0/T)$ or the linear model: $\ln(K_{eq} \cdot \chi^\circ) = -\Delta H_0^\circ/RT + \Delta S_0^\circ/R$. To calculate the enthalpy and entropy at 37°C (310K), the following equations were used: $\Delta H^\circ(T) = \Delta H_0^\circ + \Delta C_p(T - T_0)$, and $-T\Delta S^\circ(T) = -T(\Delta S_0^\circ + \Delta C_p \ln(T/T_0))$. Estimates reported as mean \pm standard deviation over 1000 bootstrap fits.

Non-linear model						
Lipid	T_0 (K)	ΔC_p (kcal mol ⁻¹ K ⁻¹)	ΔH_0° (kcal mol ⁻¹)	ΔS_0° (kcal mol ⁻¹ K ⁻¹)	$\Delta H^\circ_{37^\circ C}$ (kcal mol ⁻¹)	$-T\Delta S^\circ_{37^\circ C}$ (kcal mol ⁻¹)
EPL	300.0 \pm 1.3	-2.0 \pm 0.3	10.0 \pm 2.7	0.078 \pm 0.009	-9.5 \pm 2.5	-4.4 \pm 2.4
PEPG	300.8 \pm 2.2	-1.7 \pm 0.3	12.0 \pm 3.8	0.079 \pm 0.013	-3.7 \pm 2.2	-8.3 \pm 2.2
Linear model						
Lipid	ΔH° (kcal mol ⁻¹)			ΔS° (kcal mol ⁻¹ K ⁻¹)		
EPL	-18.9 \pm 6.1			-0.0174 \pm 0.0193		
PEPG	-10.4 \pm 4.7			0.0033 \pm 0.0149		

Table S4. Analysis of number and distribution of coarse-grained water beads in the membrane defect around the CLC-ec1 dimerization interface relative to the bulk lipid bilayer. Calculations are carried out on 8 replicates of 7.5 μs each coarse-grained MARTINI 2.2 molecular dynamics simulations in 2:1 POPE/POPG from (6). The estimated number of coarse-grained water beads that are removed from the membrane upon dimerization is equal to $2*(N_{\text{CGwater}}(\text{defect})-N_{\text{CGwater}}(\text{bulk}))$, where the factor of 2 accounts for the two subunits. Note, in the coarse-grained Martini force-field, a single water bead approximates four atomic water molecules.

Dimerization interface defect			
	Outer Leaflet	Inner Leaflet	Total Bilayer
Area (nm ²)	12.6	11.7	24.3
No. of lipids	19.0	17.7	36.7

	$N_{\text{CGwater}}(\text{defect})$			$2*(N_{\text{CGwater}}(\text{defect})-N_{\text{CGwater}}(\text{bulk}))$
Full lipid	73.4	68.4	141.8	19.1
PO4-C4	56.0	52.2	108.2	19.2
Ester-C4	24.5	23.0	47.4	23.6
C1-C4	15.1	14.3	29.4	17.8
C2-C4	7.8	7.5	15.3	12.7
C3-C4	4.1	3.9	8.0	8.0
C4	2.5	2.4	4.9	5.0

Bulk lipid bilayer			
	Outer Leaflet	Inner Leaflet	Total Bilayer
Area (nm ²)	12.5	11.5	24.0
No. of lipids	21.0	19.4	40.5

	$N_{\text{CGwater}}(\text{bulk})$		
Full lipid	68.9	63.4	132.3
PO4-C4	51.4	47.2	98.6
Ester-C4	18.6	17.0	35.6
C1-C4	10.7	9.8	20.5
C2-C4	4.7	4.2	8.9
C3-C4	2.1	1.9	4.1
C4	1.3	1.2	2.4

SI References

1. J. Pencer, S. Krueger, C. P. Adams, J. Katsaras, Method of separated form factors for polydisperse vesicles. *J Appl Crystallogr* **39**, 293–303 (2006).
2. L. Cliff, R. Chadda, J. L. Robertson, Occupancy distributions of membrane proteins in heterogeneous liposome populations. *Biochimica Et Biophysica Acta Biomembr* **1862**, 183033 (2019).
3. H. L. Scott, *et al.*, On the Mechanism of Bilayer Separation by Extrusion, or Why Your LUVs Are Not Really Unilamellar. *Biophys J* **117**, 1381–1386 (2019).
4. S. R. Kline, Reduction and analysis of SANS and USANS data using IGOR Pro. *J Appl Crystallogr* **39**, 895–900 (2006).
5. R. Chadda, *et al.*, The dimerization equilibrium of a ClC Cl(-)/H(+) antiporter in lipid bilayers. *Elife* **5**, e17438 (2016).
6. R. Chadda, *et al.*, Membrane transporter dimerization driven by differential lipid solvation energetics of dissociated and associated states. *Elife* **10**, e63288 (2021).
7. N. Bernhardt, J. D. Faraldo-Gómez, MOSAICS: A Software Suite for Analysis of Membrane Structure and Dynamics in Simulated Trajectories. *Biophys J* (2022) <https://doi.org/10.1016/j.bpj.2022.11.005>.
8. R. Chadda, L. Cliff, M. Brimberry, J. L. Robertson, A model-free method for measuring dimerization free energies of CLC-ec1 in lipid bilayers. *J Gen Physiology* **150**, 355–365 (2018).

Chapter 5: The Calculation of Cavity Volume **in the Coarse-grained MD Simulation** **Depending on Solvent Volume**

5.1 Preface to the Chapter

This is a study in progress and involves collaborative efforts from Dr. Tugba N. Ozturk who built the coarse-grained CLC-ec1 structural models, which I simulated and analyzed.

5.2 Abstract

Previous studies showed that the CLC-ec1 chloride/proton antiporter forms homodimer complexes in lipid bilayers with high kinetic stability. Subunit-exchange measurements show that it takes weeks for the system to reach equilibrium at room temperature in *E. coli* polar lipid bilayers. To account for such anomalously slow kinetics, we hypothesized that the dissociation process involves a concerted solvation step as the two subunits are moved away from one another. This implies that there are states on the reaction pathway where there are no lipids or protein interactions at the binding surface, in other words, the reaction introduces vacuum cavities that are inaccessible to the surrounding lipid solvent, presenting high energy configurations that could act as kinetic barriers in the reaction. To examine if this is occurring, we carried out molecular dynamics simulations of CLC-ec1 subunits in palmityl-oleoyl phosphatidylcholine (POPC) lipid bilayers at different degrees of subunit separation, from 8 to 24 Å measured from a centrally defined axis and analyzed lipid solvation in between the subunits. Next, we examined whether mixed lipid bilayers, containing smaller lipoidal molecules such as the lysolipid palmitoyl phosphatidylcholine (PPC) or benzene could occupy these cavities, providing the means to potentially stabilize these poorly

solvated states that would be expected to speed up the reaction. The results indicate that smaller size molecules with a higher concentration have a higher packing density by occupying cavities at the dimerization interface between the CLC subunits in the system. Finally, I developed a bulk Förster resonance energy transfer assay for measuring changes in subunit exchange in liposomes upon addition of small lipoidal molecules, using the detergent beta-octyl glucoside (β -OG) as a test reagent. These studies present an outline for future screening of differential lipid solvation of cavity volumes and its role in binding kinetics in membranes.

5.3 Introduction

Although protein association equilibrium has been vastly studied in water, questions remain about how membrane proteins assemble and operate within the oily solvent environment of the membrane. However, recent developments in the field provide the potential for understanding the molecular basis of these reactions. The Robertson Laboratory has developed approaches for quantifying the equilibrium affinities of membrane protein oligomers in membranes, a physical model for protein association and folding (1-3). Previously, the Robertson Laboratory revealed that the kinetics of the dissociation in CLC-ec1 were extremely slow at room temperature as the samples took weeks to converge with the equilibrium end-points using single molecule photobleaching technique (1, 3). Several years later, they verified that CLC-ec1 needs several weeks to reach equilibrium at room temperature using bulk Förster resonance energy transfer (FRET) assays (4). This slow kinetics in membrane proteins was surprising, and it has been a mystery why kinetics of the membrane protein complexes and assemblies is extremely stable as it seems to be slower than most biological reactions. For comparison, in 1995, Chilkoti et al. (5) reported the dissociation rate constant of a well-known kinetically stable complex of

streptavidin and biotin showing $k_{off} = 5.4 \times 10^{-6}$ (s⁻¹) which takes 4.3 days to reach equilibrium using Isothermal Titration Calorimetry (ITC). There was another study that indicated the slow membrane association kinetics of diacylglycerol kinase (DGK) trimers using the steric-trapping studies showing unchanged DGK activities and subunit compositions remaining over the 2 days incubation period at 37°C (6). From these previous data, we ask a question: why does this membrane protein exhibit much slower kinetics, even when the complex is overall less stable, and especially considering that most of the binding interface is hydrophobic, and the oily environment of the membrane is expected to facilitate dissociation?

It has been shown that the direct reconstitution of samples of CLC-ec1 at 0.1-0.0001 µg/mg lipids appears to accelerate the dimerization reaction by presenting equilibrium distributions right after the dialysis procedure (3). This was surprising to us as we have previously observed that it takes several weeks to reach dimerization equilibrium once the protein is embedded in the membrane (3, 4). We hypothesize that the dimerization reaction involves a high-energy transition state that requires the formation of a vacuum cavity in between the two subunits inaccessible to the surrounding solvent (**Fig. 1**). With this, we speculate that the reconstituted samples somehow reduce these barriers since their initial steps involve a mixture of lipid/detergent micelles that fill these cavities or facilitate lipid solvent exchange, reflecting the final self-assembled distribution in the membrane.

To examine this further, we carry out coarse-grained MD simulations of CLC-ec1 in states that are close to the dimer, but with slight separations between each subunit and examine lipid packing in between the two surfaces. In addition, we simulate conditions of mixed lipid bilayers containing small sized molecules, benzene and lysophosphatidylcholine, and examine whether these change the density of non-polar molecules between the dimerization interfaces to potentially

reduce energetic barriers and accelerate kinetics. We use the coarse-grained Martini force field and present analysis of volume cavities using a self-built Python script combined with an MDAnalysis library package for individual atom selection (7). The results from this investigation will provide a quantitative analysis offering insight into why membrane protein complexes appear to be kinetically trapped in lipid bilayers.

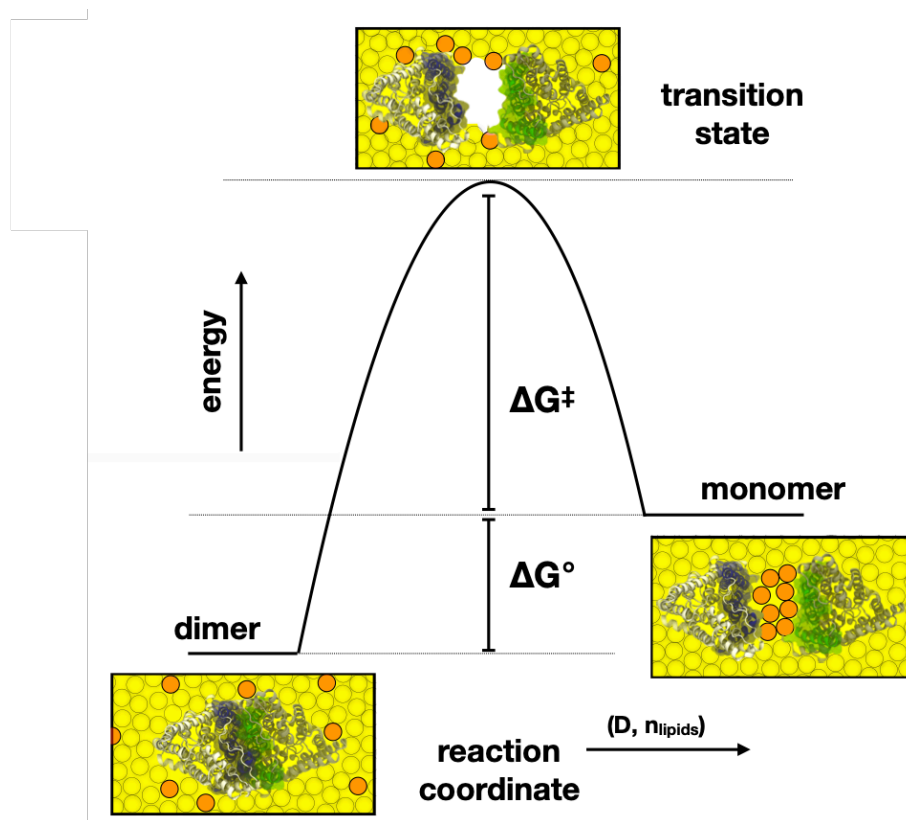


Figure 1. Hypothetical energy landscape of CLC-ec1 dimerization. For dimerization, all the lipids are squeezed out and two subunits come into contact. For dissociation, both subunits are pulled apart and lipids come in to solvate the subunits. In both of ways, we hypothesize that there is a transition state where there is a gap in between the two subunits. The transition energy state could be a very high energy state because it would lose all protein-protein, protein-lipid interactions by creating this cavity in between and it will deplete the volume of the surrounding lipids, and the entropy of the lipids will decrease.

5.4 Materials and Methods

The simulation methods have been described earlier from Ozturk & Bernhardt et al. (8). Brief description on the method of the simulation is shown below following the procedures introduced by Ozturk & Bernhardt et al. previously (8). In addition, experimental methods for bulk FRET experiment have been described from Chadda et al. (1) and Chadda & Lee et al. (4).

5.4.1 Building the coarse-grained structural model of CLC-ec1 protomer

From the crystal structure (1OTS in the Protein Data Bank (PDB)), the initial atomic coordinates of wild-type CLC-ec1 dimer (residues 30 - 458) were obtained (9). Using the modified version of the Martinize script, a coarse-grained representation of the protein structure was built (10). The residue E113 from two subunits and the residue D417 from one subunit were protonated (11). The secondary structure of individual protomers was kept stable using elastic networks that are set with a force constant of 500 kJ/mole/nm² and an upper (lower) distance cut-off of 0.9 (0.5) nm combined with Martini 2.2 (12) force field parameters. The elastic network was created for each protomer separately, without any inter-subunit elastic bonds. The constructed CLC-ec1 dimer based on the crystal structure (PDB ID: 1OTS), was positioned in a manner where the dimerization interface aligns perpendicularly to the *x*-axis, while the bilayer normal runs parallel to the *z*-axis.

5.4.2 Equilibration of the POPC bilayer on a coarse-grained system

Insane (INSert membrANE) script was used to embed the coarse-grained protein models into a pure 1-palmitoyl-2-oleoyl-sn-glycero-3-phosphocholine (POPC) lipid bilayer, solvated with 0.15 M NaCl and water (90% regular water and 10% antifreeze water). The resulting simulation system was 25 nm × 15 nm × 10 nm (13). Interactions between the beads in the system were calculated using Martini 2 force field parameters for lipid, water and ion beads and Martini 2.2 for

protein beads (14), and the system was energy-minimized and equilibrated with the following steps as described previously (15). The initial energy minimization was carried out to remove the initial steric clashes in the systems using a soft-core potential followed by next minimization step using the regular 12-6 Lennard-Jones potential. Initial equilibration was done while restraining the positions of the protein's backbone beads using a harmonic potential with a force constant of 1000 kJ/mole/nm² for 10 ps, followed by 500 kJ/mole/nm² for 3 ns since increasing the number of minimization steps might result in large gaps between the protein and lipid beads, as lipid molecules tend to attract each other more rapidly than the proteins do. The time step was continuously increased from 2 fs to 20 fs. 1 bar and 310 K were used for the pressure and temperature with the semi-isotropic Berendsen barostat (16) along with the velocity-rescaling algorithm (17). Once all the steps are completed, 20 μ s-long coarse-grained MD simulations were run using GROMACS (2021.5). In the production step, the system was switched to the Parinello-Rahman barostat (18) which was suggested by de Jong et al. (15).

5.4.3 Applying restraints for the coarse-grained CLC-ec1-membrane simulation systems

For the coarse-grained simulation, the orientational restraints were initially applied to make sure that two CLC-ec1 subunits remain consistently facing each other while allowing the proteins to wobble throughout the simulation. The harmonic restraints with a force constant 2000 - 7000 kJ/mole/nm² were used on the collective variables using Plumed 2 (19). Next, the positional restraints were applied to maintain two monomers at the center of the simulation box. Finally, inter-subunit distance restraints were set at -4.3 nm for 8 Å, -4.7 nm for 12 Å, -5.1 nm for 16 Å, -5.5 nm for 20 Å, -5.9 nm for 24 Å respectively.

5.4.4 Analysis of dynamic behavior of solvent exchange

With a structure and a trajectory file, analysis of dynamic behavior of solvent exchange in CLC-ec1 100% POPC, 10% PPC & 90% POPC, 10% benzene & 90% POPC in 16 Å separation system were carried out to investigate if the lipids, non-polar molecules come in and out of the dimerization interface over the 10 μs of simulation time. Python script was built for this analysis. The script uses the MDAnalysis library (20) combined with “atomselect” command to select atoms (POPC-GL2, PPC-GL2, benzene-R2) included in the box within the average x , y coordinates. Individual atoms selected at the beginning ($t = 0$) were analyzed over the 10 μs simulation period and checked if they are outside or inside the box. If the bead is outside of the box at least once over the simulation, the bead is considered as out of the box. For box definition in this analysis, minimum and maximum x coordinates were obtained from the average x coordinate from M415, and minimum and maximum y coordinates were obtained from the average y coordinate from F438 over the entire simulation for box definition roughly around the dimerization interface.

5.4.5 Angle analysis between subunits with different restraints

3 residues (L177, L258, F438) at $t = 0$ from CLC-ec1 with same x coordinate values were selected to create a plane for each subunit ($x = 11.2$ nm, $x = 13.9$ nm). A smaller angle between the planes is measured by the angle between the normal vectors of each plane. Analyses were done with 2000, 3000, 4000, 5000, 6000, and 7000 kJ/mole/nm² restraints over 20 μs simulation time.

5.4.6 Analysis of solvent inaccessible cavity volume between the dimerization interface

To make sure that the systems are analyzed where the dynamic is in equilibrium, the frame range was selected for analysis where the number of beads was within the 10% range of average

of last 1 μ s. Solvent inaccessible cavity volume was individually calculated at selected frames from $(x_{max} \times x_{min} \times y_{max} \times y_{min} \times z_{max} \times z_{min} - \text{the volume of the protein beads within the box})$. The number of beads was only considered in the selected frame range. The density was calculated from the total number of beads (POPC-GL2 or POPC-GL2 + PPC-GL2 or POPC-GL2 + benzene-R2) divided by the solvent inaccessible box volume.

5.5 Results

The coarse-grained systems were set up with 100% POPC, 90% POPC & 10% PPC, 90% POPC & 10% benzene, 70% POPC & 30% PPC, 70% POPC & 30% benzene with 8 – 24 Å separation. We use PPC which is one kind of lysolipids with C16:0 palmitic acid - C18:0 stearoyl tails. Therefore, PPC shares the same head groups and linker with a POPC lipid, but it has only one acyl tail instead of two. PPC is a great option for this study as we can only consider the density from the size of the molecules without the affect caused from the head groups. Benzene is a molecule that only contains 3 coarse-grained beads with a ring shape, and this is significantly smaller molecule compared to POPC that has 12 coarse-grained beads in one molecule. Also,

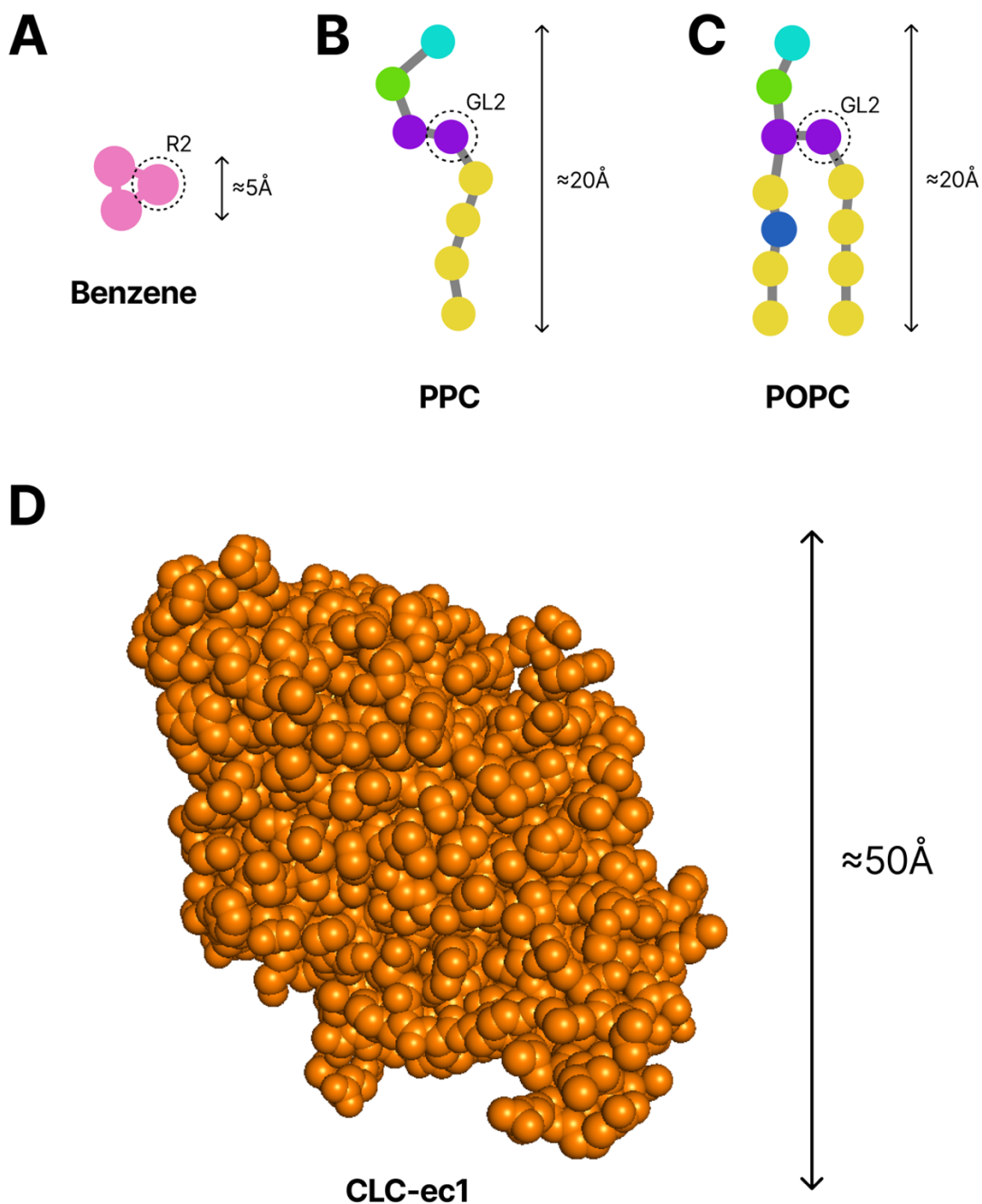


Figure 2. Martini topologies used for coarse-grained MD simulation Benzene and PPC are selected as surfactant molecules for the coarse-grained MD simulation. The figure shows martinized topologies of (A) Benzene (B) PPC (C) POPC (D) CLC-ec1 showing the side of dimerization interface. Lipid head groups are represented with cyan (choline) and green (phosphate), and linker is represented with purple (glycerol). Carbon saturated chain is represented with yellow, and 1-2 cis double bonds are represented with blue. Dotted circle indicates the position of R2 and GL2 beads that were selected for the simulation. Dimensions are represented on the right side of the figure for each molecule.

5.5.1 Positional analysis of CLC-ec1 subunit during the simulation

To quantify solvent density changes in between the CLC subunits, we wanted to first check whether the protein orientation was similar in the different systems with similar inter-subunit volumes. It is crucial to investigate how individual proteins move and check if the angle changes affect the number of proteins in box at the beginning stage of this analysis. The number of protein beads inside the box should remain the same over the simulation. Therefore, we investigated movement of individual proteins whether there is any change in direction of protein on the two different subunits over the simulation and if that affects the number of protein beads in box. If the angle between the protomers stays the same, the number of protein beads inside the box should remain the same over the simulation. First, the coordinates from helices Q and I were selected for y_{max} , y_{min} as they are on the external side, and x_{max} , x_{min} , z_{max} , z_{min} were selected from helices H and P for box definition between the CLC subunits, and the box was defined by x_{max} (M415), x_{min} (M415), y_{max} (F438), y_{min} (F438), z_{max} (T416), and z_{min} (I201) for the angle analysis. Next, an angle between two planes when 3 residues (L177, L258, F438) with the same x coordinate values were selected to create a parallel plane for each subunit over the entire simulation time (**Fig. 3A, 1B**). The angle between the planes was measured by the angle between the normal vectors of each plane. (**Fig. 3C**). Systems with 2000, 3000, 4000, 5000, 6000, and 7000 kJ/mole/nm² restraints over 20 μ s simulation time on a 4 Å and 8 Å CLC-ec1 100% POPC system were analyzed. The data shows that the angle between two planes changes over the course of the simulation (**Fig. 3D**). It was also found that the number of protein beads in the box changes as the angle between the two planes increases (**Fig. 3D**). We observed that the angle between the subunits changes over the simulation and the number of protein beads in box changes corresponding to the angle between the two planes defined.

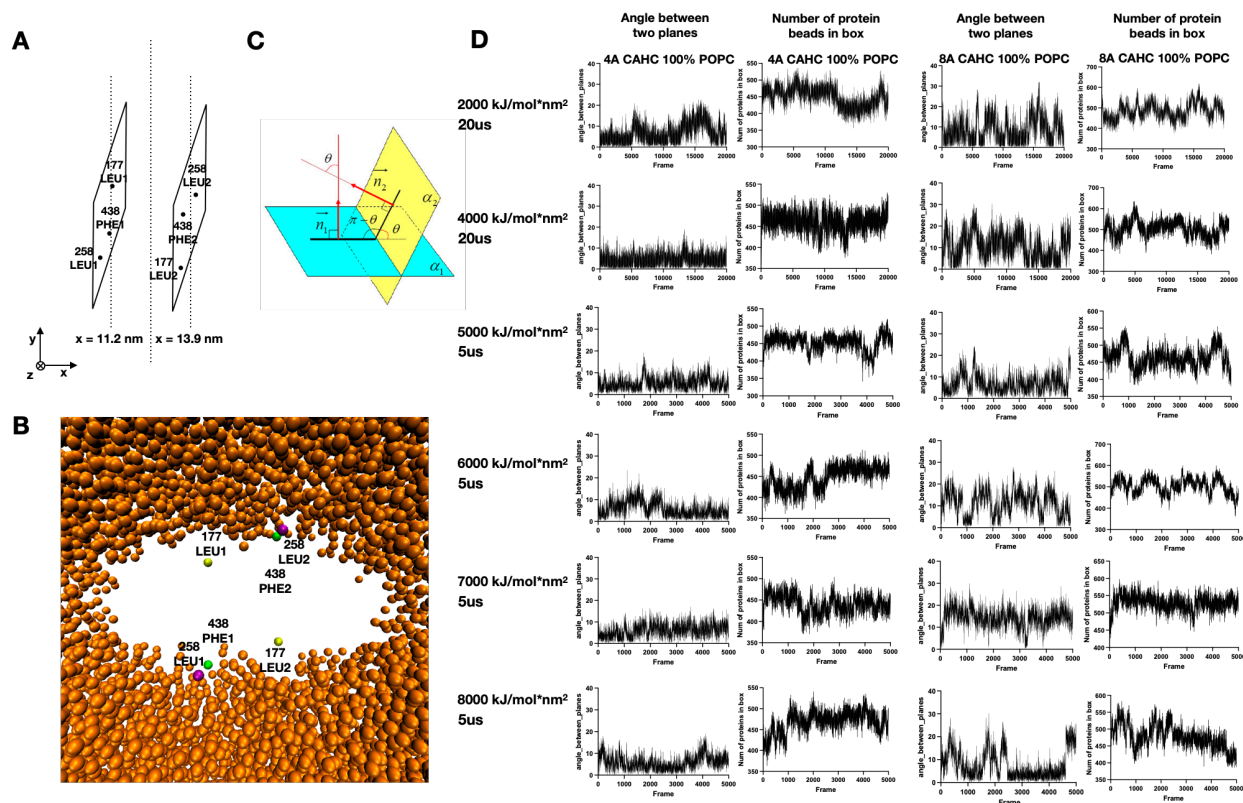


Figure 3. Angle analysis between subunits in different simulations (A) 3 residues (L177, L258, F438) with the same x coordinate values were selected to create a plane for each subunit. ($x = 11.2$ nm, $x = 13.9$ nm) (B) Actual position of selected residues on the system (C) Definition of the angle that is measured. Angle between the planes is measured by the angle between the normal vectors of each plane (D) Angle between two planes and the number of proteins in a box on 4 Å CLC-ec1 100% POPC system with different restraints values $\kappa = 2000, 4000, 5000, 6000,$ and 7000 kJ/mole/nm².

This indicates that it is necessary to define the box between the dimerization interfaces with the residues that can be included always over the entire simulation.

Before measuring the density between the subunits of CLC-ec1, we needed to make sure that residues contacting with the other part of the subunit are all included in the box during the entire simulation. For the box definition between the dimerization interfaces, the box was defined so that residues contacting with the other part of the subunit and H, I, P, and Q helices (191, 193 -

202, 215 - 234, 243, 246, 249, 252, 403, 405 - 420, 422 - 434) can be included in the box all the time over the simulation (**Fig. 4**). For x_{max} , x_{min} , backbone residue N318, S329, G108, and G146 were selected, and the center of mass was calculated for x_{max} , x_{min} value. For y_{max} , y_{min} , backbone residue L378, F379, P380, Q381 were selected, and the center of mass was calculated for maximum, minimum value. Finally, y_{max} was obtained from the maximum of the center of mass + 1 (nm), and y_{min} was obtained from the minimum of the center of mass - 1 (nm). For z_{max} , backbone residue G326, E377, P380, D73 were selected, and z_{max} was calculated from the center of mass + 1 nm. For z_{min} , backbone residue D171, Q456, P121, and D178 were selected, and z_{min} was calculated from the center of mass - 1 nm. Each residue (191, 193 - 202, 215 - 234, 243, 246, 249, 252, 403, 405 - 420, 422 - 434) was analyzed individually to make sure that all the residues are included in the defined box over the 20 μ s simulation time using Python script using the MDAnalysis package. Data shows the residues in the 4 Å CLC-ec1 100% POPC system, and we found that they are all included in the box over the 20 μ s entire simulation.

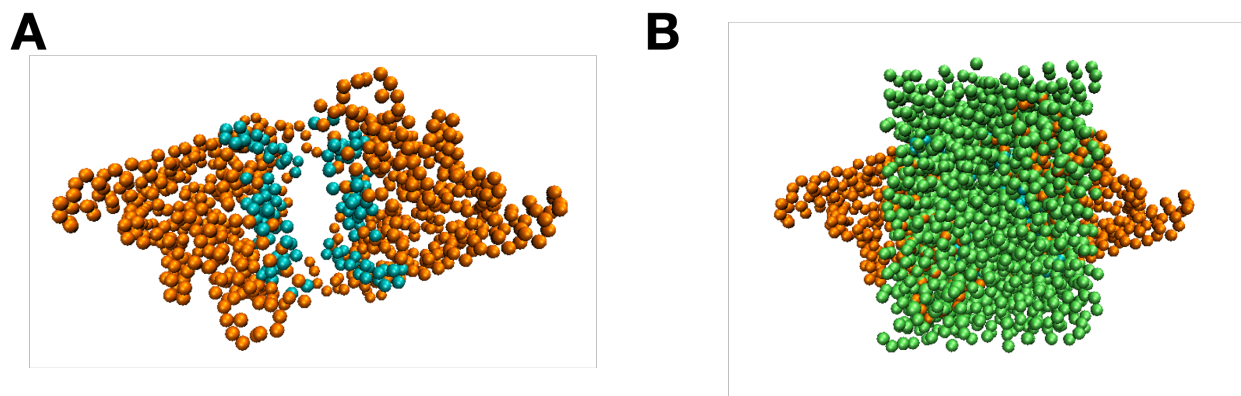


Figure 4. Box definition between the dimerization interface (A) Coarse-grained CLC-ec1 proteins with 8 Å separation. Residues contacting with other part of subunit and H, I, P, and Q helices (191, 193 - 202, 215 - 234, 243, 246, 249, 252, 403, 405 - 420, 422 - 434) are shown (Cyan). (B) Box was defined to include all the residues over the entire 20 μ s simulation. For x_{max} , x_{min} , backbone residue N318, S329, G108, G146 were selected, and the center of mass was calculated for x_{max} , x_{min} value. For y_{max} , y_{min} , backbone residue L378, F379, P380, Q381 were selected, and the center of mass was calculated for maximum, minimum value. Finally, y_{max} was obtained from maximum of the center of mass + 1 nm, and y_{min} was obtained from minimum of the center of mass - 1 nm. For z_{max} , backbone residue G326, E377, P380, D73 were selected, and z_{max} was calculated from the center of mass + 1 nm. For z_{min} , backbone residue D171, Q456, P121, D178 were selected, and z_{min} was calculated from the center of mass - 1 nm.

5.5.2 Evidence of dynamic lipid exchange between CLC subunits

Next, we investigated whether lipids and non-polar molecules come in and out of the dimerization interface over the time course of the simulation to make sure that our system is a dynamic system. Figure 5 shows a trajectory of the beads selected in the defined box on the CLC-ec1 with a 16 Å inter-subunit distance system over 20 μs the entire simulation time. For this analysis, the box was defined from x_{max} , x_{min} , and y_{max} , y_{min} , from the residues included in the H, I, P, and Q helices for simplicity and the entire z -range to capture the beads in the lipid headgroup. We specifically chose the atoms using a self-built Python script combined with the MDAnalysis Python library package. “atomselection” commands were used to specifically select the beads that we need. We observed that 100% of 10 POPC (GL2) beads inside the box at $t = 0$ was located at least once over the entire simulation in the 100% system. On the other hand, we also selected all POPC (GL2) beads outside of the box to check if they come inside the box. In this case, we observed that 61.5% of all POPC (GL2) beads outside of the box entered the box. To verify that this happens in different systems, we checked with 10% PPC & 90% POPC and 10% benzene & 90% POPC with the same inter-subunit separation. First, 100% of POPC (GL2) beads inside the box in 10% PPC & 90% POPC system went outside of the box and 66.0% of POPC (GL2) beads outside of the box entered the box. In the case of PPC (GL2), 100% of PPC (GL2) beads inside the box and 88.4% of PPC (GL2) beads outside the box entered the box. Next, in the 10% benzene and 90% POPC system, 100% of POPC (GL2) beads inside the box went outside, and 63.5% of POPC (GL2) outside of the box entered the box. Lastly, 100% of benzene (R2) beads inside the box came out from the box and 98.1% of benzene (R2) beads went inside of the box. All the selected beads inside the box went outside of the box, and most of the selected beads outside

of the box enter the box showing that it is a dynamic system where POPC and non-polar lipid beads exchanges happen.

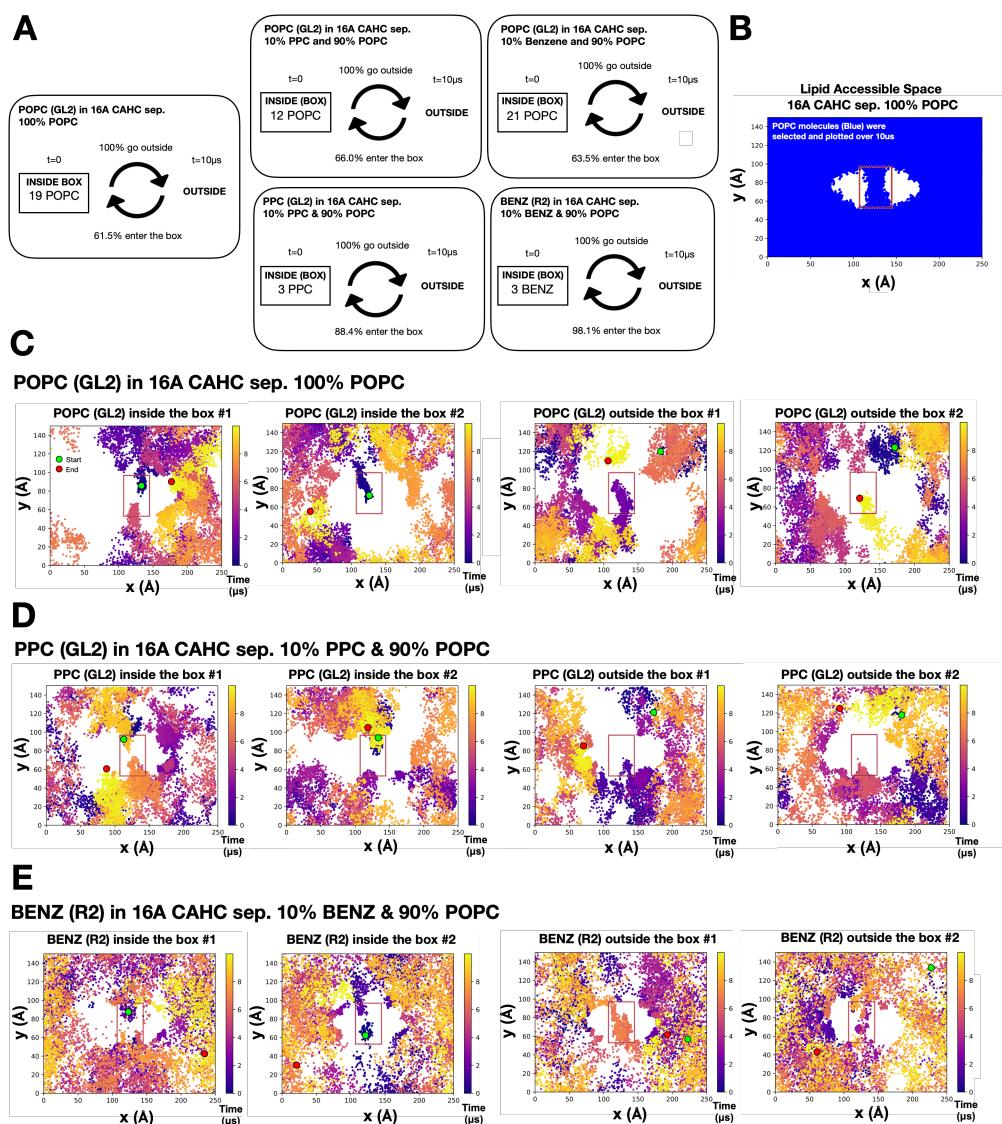


Figure 5. Analysis of dynamic behavior of solvent exchange in CAHC 100% POPC, 10% PPC & 90% POPC, 10% benzene & 90% POPC in 16 Å separation system (A) Summary of dynamic behavior analysis representing percentage of POPC (GL2), PPC (GL2), BENZ (R2) beads selected at the beginning of going outside from inside the box or coming inside the box from outside. (B) x - y plane representing lipid accessible space. POPC beads (blue) are selected and plotted over 10 μ s (C) Trajectory of selected beads inside the box over the entire simulation. The green dot is the position of the bead at $t = 0$, and the red dot is the position of the bead at $t = 10$ μ s. The gradient color bar indicates the simulation time (μ s). The plots show the trajectories of representative two separate beads for POPC (GL2) beads in 100% POPC system (D) PPC (GL2) beads in 10% PPC & 90% POPC system (E) benzene (R2) beads in 10% benzene & 90% POPC system. Minimum and maximum x coordinates were obtained from the average coordinate from M415, and minimum and maximum y coordinates were obtained from the average coordinate from F438 over the entire simulation for box definition roughly around the dimerization interface. The analysis shows that lipids, non-polar molecules come in and out of the dimerization interface over the time course of the simulation.

5.5.3 Density analysis of CLC-ec1 subunit in mixed lipid bilayers containing small molecules

Having verified a box definition where the dimerization surface is always included, and dynamic lipid exchange, we can now examine whether adding small molecules into the system really decrease the density between the dimerization helices. If there is a change in lipid density with different solvent composition, this might yield differences in energetics of partially solvated states which may translate to changes in kinetics. Therefore, we next examined how the packing between the dimerization interface changes depending on the type of small molecules and inter-subunit distances. We analyzed the packing information on the 100% POPC, 10% PPC & 90% POPC, 10% benzene & 90% POPC, 30% PPC & 70% POPC, 30% benzene & 70% POPC system with the 8 – 24 Å separation. Packing information was calculated from the number of beads divided by the volume within the 10% range of the average of the last 1 μ s where the system is in dynamic equilibrium (**Fig. 6**). We observed the highest density in 30% benzene & 70% POPC and the lowest density in 100% POPC indicating that the small molecule systems have increased packing (**Fig. 7**).

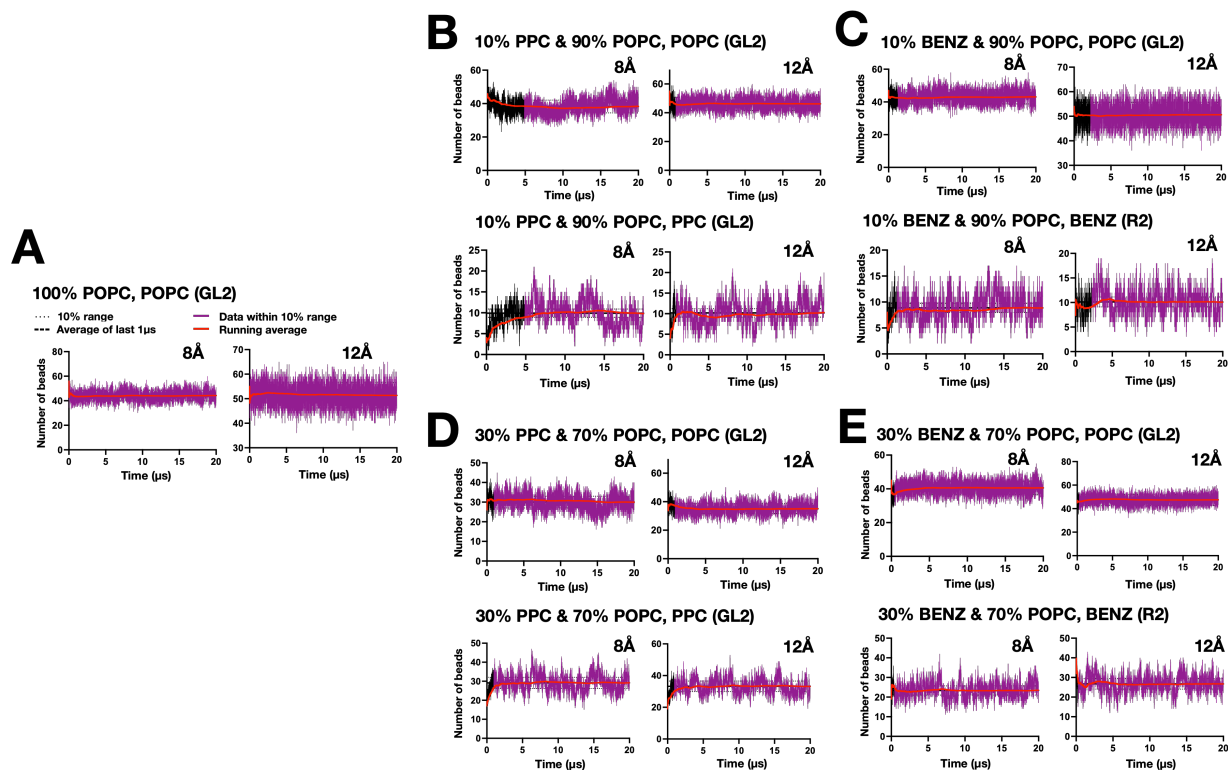


Figure 6. Number of beads between the dimerization interface Number of beads (POPC (GL2), PPC(GL2), BENZ(R2)) included in the defined box with an inter-subunit distance at 8 Å and 12 Å as a function of time in different systems: (A) 100% POPC (B) 10% PPC & 90% POPC (C) 10% BENZ & 90% POPC (D) 30% PPC & 70% POPC (E) 30% BENZ & 70% POPC. Red solid line represents the running average of the traces. Purple solid line shows the data points within 10% range of average indicating the dynamic equilibrium of the system.

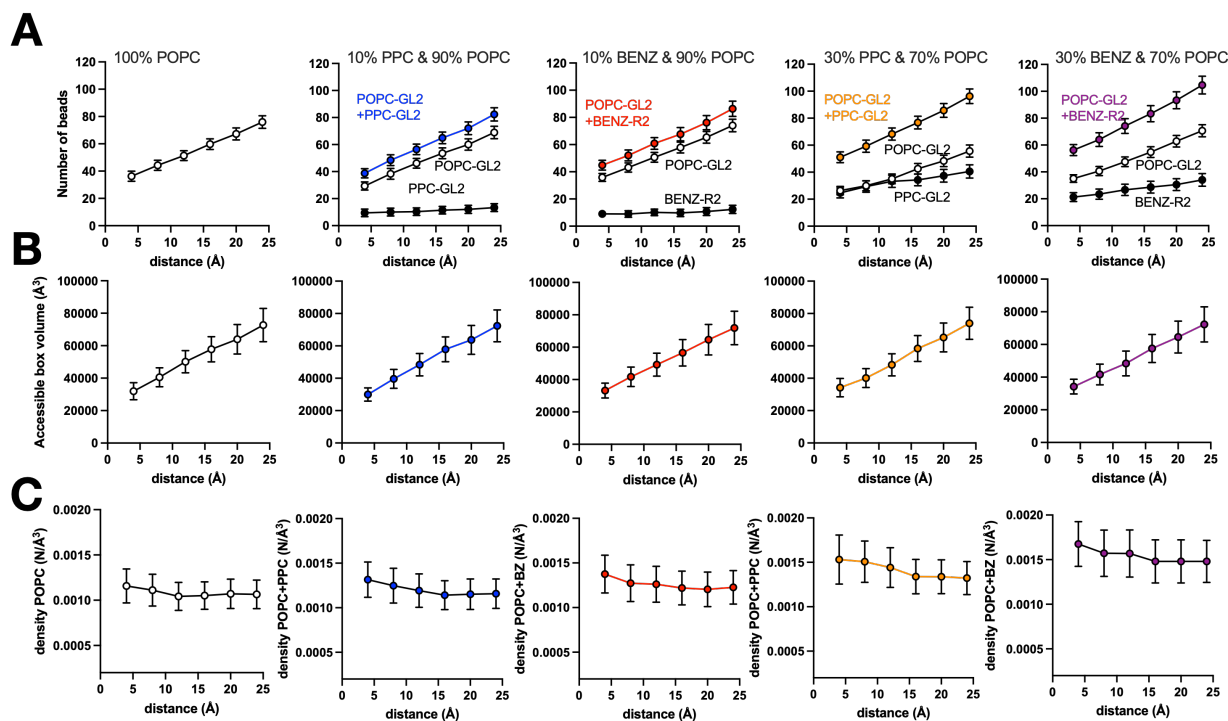


Figure 7. Density between the dimerization interface (A) Number of beads between the dimerization interface at different inter-subunit distances in different systems (100% POPC, 10% PPC & 90% POPC, 10% BENZ & 90% POPC, 30% PPC & 70% POPC, 30% BENZ & 70% POPC). POPC (GL2), PPC (GL2) BENZ (R2) beads were counted in the number of beads. (B) Accessible box volume at different inter-subunit distances. Accessible box volume was calculated from the entire defined box volume subtracted from the volume of the protein beads included in box (C) Density at different inter-subunit distances. Density was calculated from the number of beads divided by the accessible box volume.

5.5.4 Analysis of subunit exchange kinetics on the CLC-ec1 with small molecule β -OG using bulk FRET measurement

After verifying that the solvent density between the dimerization interface increases as the concentration of small molecules increases, we moved onto experimental studies using bulk FRET measurements to examine whether addition of small lipoidal molecules impact the subunit-exchange kinetics. For this experiment, β -OG was titrated to the pauci-lamellar (PLV) states of the CLC-ec1 WT $_{\text{Cy3+Cy3}^{\text{fused}}}$ sample in EPL membrane with a concentration ratio (0 - 18 mol%), and the measurement was carried out at 37 °C. FRET traces were analyzed from the one-phase association fitting to calculate the subunit exchange kinetics (k_{obs}) (**Fig. 8A**). The normalized FRET signal shows that there appears to be a slight acceleration in kinetics with 18 mol% of β -OG, but the results are not yet statistically significant (**Fig. 8B**). While further work is required to examine this, the methodology is established for high-throughput screening of molecules that partition into membranes for their impact on kinetic stability of oligomeric complexes in membranes.

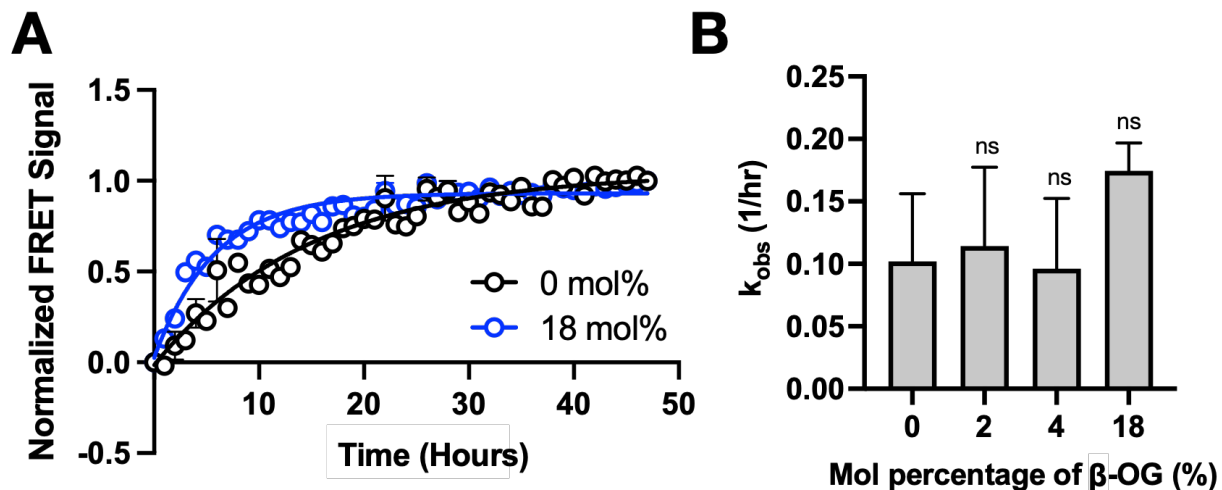


Figure 8. Subunit exchange FRET experiment with titration of β -OG (A) Normalized FRET signal as a function of time with different concentrations of β -OG measured at 37 °C. Data is represented from $n = 2$. 0 mol% of β -OG is represented with black and 18 mol% of β -OG is represented with blue. (B) Subunit exchange kinetics (k_{obs}) at different mol percentage of β -OG. Statistical tests were carried out using the unpaired parametric student's t-test with the k_{obs} at 0 mol%.

5.6 Discussion

In our study, we found that the systems with smaller molecules yield increases in solvent density at the dimerization interface in POPC lipid bilayer from the coarse-grained simulations. We also confirmed that the coarse-grained systems that we built with POPC and non-polar molecules are dynamic systems where the lipids and lipoidal molecules exchange in and out from the volume defined between the two subunits (**Fig. 5**).

We originally hypothesized that introducing small molecules would lead to increase in dimerization kinetics as the cavity volume will decrease by decreasing the transition energy state (**Fig. 1**). While our simulation and experimental findings show some indication of this, this requires further investigation to determine whether this hypothesis is supported. The simulation data would be more solid if the density analysis could be compared to changes in the bulk membrane for the same volume that is defined by the box between the dimerization interface to clearly verify the increase in density between the dimerization interface. In addition, even though our experimental approach we found some evidence of β -OG speeding up the subunit-exchange, this happened only at the highest concentration tested and the results were not significant. Therefore, it is too early to conclude that the small molecule speeds up the kinetics as the data from 0-5 mol% is still unclear. We need more replicates to clearly conclude that small molecule is affecting the kinetics. Furthermore, it would be more beneficial if we conduct kinetic experiments with benzene and PPC lysolipids which we simulated.

As a final step of this project, we want to correlate the calculated cavity volume with the experimental subunit-exchange kinetics values. From the cavity volume from our coarse-grained molecular dynamic simulations, the integral cavity volume can be calculated for different types of molecules, and the integrated values can be correlate with the observed rate constant that is

measured from the FRET measurement. This will allow us to determine if the kinetics depends on the cavity volume that may be formed on the dimerization reaction pathway.

5.7 Conclusion

Here we report the method of calculating the cavity volume in between the CLC-ec1 subunits at different inter-subunit distances with different types of small molecules (benzene, PPC) using coarse-grained molecular dynamic simulation by establishing the system to calculate the cavity volume. First, we found that the CLC-ec1 subunits do not keep the same movement with each other over the course of simulation while testing restraint strengths from 2000 - 7000 kJ/mole/nm², and this should be important factor we need to consider when identifying the packing density between the subunits. In addition, we observed that the simulated system is a dynamic system where solvents can enter the cavity back and forth. With this, our analysis demonstrated that cavity between the CLC subunits is more packed with small size molecules with higher concentrations in the system providing a premise that small lipoidal molecules may accelerate reaction kinetics by improving solvation along the reaction pathway.

References

1. R. Chadda *et al.*, The dimerization equilibrium of a ClC Cl(-)/H(+) antiporter in lipid bilayers. *Elife* **5** (2016).
2. R. Chadda, J. L. Robertson, Measuring Membrane Protein Dimerization Equilibrium in Lipid Bilayers by Single-Molecule Fluorescence Microscopy. *Methods Enzymol* **581**, 53-82 (2016).
3. R. Chadda, L. Cliff, M. Brimberry, J. L. Robertson, A model-free method for measuring dimerization free energies of CLC-ec1 in lipid bilayers. *J Gen Physiol* **150**, 355-365 (2018).
4. R. Chadda *et al.*, A thermodynamic analysis of CLC transporter dimerization in lipid bilayers. *Proc Natl Acad Sci U S A* **120**, e2305100120 (2023).
5. A. Chilkoti, P. S. Stayton, Molecular-Origins of the Slow Streptavidin-Biotin Dissociation Kinetics. *Journal of the American Chemical Society* **117**, 10622-10628 (1995).
6. R. E. Jefferson, T. M. Blois, J. U. Bowie, Membrane proteins can have high kinetic stability. *J Am Chem Soc* **135**, 15183-15190 (2013).
7. N. Michaud-Agrawal, E. J. Denning, T. B. Woolf, O. Beckstein, Software News and Updates MDAnalysis: A Toolkit for the Analysis of Molecular Dynamics Simulations. *J Comput Chem* **32**, 2319-2327 (2011).
8. T. N. Ozturk *et al.*, Mitigation of membrane morphology defects explain stability and orientational specificity of CLC dimers. *bioRxiv* 10.1101/2023.03.16.533024, 2023.2003.2016.533024 (2023).
9. R. Dutzler, E. B. Campbell, R. MacKinnon, Gating the selectivity filter in ClC chloride channels. *Science* **300**, 108-112 (2003).
10. D. H. de Jong *et al.*, Improved Parameters for the Martini Coarse-Grained Protein Force Field. *J Chem Theory Comput* **9**, 687-697 (2013).
11. J. D. Faraldo-Gomez, B. Roux, Electrostatics of ion stabilization in a ClC chloride channel homologue from Escherichia coli. *Journal of Molecular Biology* **339**, 981-1000 (2004).
12. L. Monticelli *et al.*, The MARTINI Coarse-Grained Force Field: Extension to Proteins. *J Chem Theory Comput* **4**, 819-834 (2008).
13. T. A. Wassenaar, H. I. Ingolfsson, R. A. Bockmann, D. P. Tieleman, S. J. Marrink, Computational Lipidomics with insane: A Versatile Tool for Generating Custom Membranes for Molecular Simulations. *J Chem Theory Comput* **11**, 2144-2155 (2015).

14. S. J. Marrink, H. J. Risselada, S. Yefimov, D. P. Tieleman, A. H. de Vries, The MARTINI force field: coarse grained model for biomolecular simulations. *J Phys Chem B* **111**, 7812-7824 (2007).
15. D. H. de Jong, S. Baoukina, H. I. Ingolfsson, S. J. Marrink, Martini straight: Boosting performance using a shorter cutoff and GPUs. *Comput Phys Commun* **199**, 1-7 (2016).
16. H. J. C. Berendsen, J. P. M. Postma, W. F. Vangunsteren, A. Dinola, J. R. Haak, Molecular-Dynamics with Coupling to an External Bath. *J Chem Phys* **81**, 3684-3690 (1984).
17. G. Bussi, D. Donadio, M. Parrinello, Canonical sampling through velocity rescaling. *J Chem Phys* **126** (2007).
18. M. Parrinello, A. Rahman, Polymorphic Transitions in Single-Crystals - a New Molecular-Dynamics Method. *J Appl Phys* **52**, 7182-7190 (1981).
19. G. A. Tribello, M. Bonomi, D. Branduardi, C. Camilloni, G. Bussi, PLUMED 2: New feathers for an old bird. *Comput Phys Commun* **185**, 604-613 (2014).
20. N. Michaud-Agrawal, E. J. Denning, T. B. Woolf, O. Beckstein, MDAnalysis: a toolkit for the analysis of molecular dynamics simulations. *J Comput Chem* **32**, 2319-2327 (2011).

Chapter 6: Connecting CLC-ec1 Dimerization with Functional Activity

6.1 Preface to the chapter

This chapter describes ongoing work to investigate the link between dimerization and different functional states of CLC channels and transporters. It contains results collected by me, Taeho Lee, together with Robyn Mahoney-Kruszka.

6.2 Abstract

So far, structural studies of native CLC channels and transporters have always revealed the protein in a homodimeric form. However, the reason for this dimeric assembly remains unclear, as previous experiments show that isolated subunit is the minimal requirement for transport function. While this shows that dimerization is not required for function, we form the hypothesis that dimerization offers a means of coupling subunits together to regulate function. In turn, this implies that functional activity may be linked to the dimer structure and stability, and vice versa. To investigate this further, we first examined whether the dimerization reaction depends on pH, a known regulator of CLC-ec1 transport with acidic conditions increasing activity. Subunit exchange of WT CLC-ec1 in membranes was measured by Förster Resonance Energy Transfer (FRET) at pH 3.5-7.5, showing no dynamic exchange at pH 6.5 & 7.5 conditions known to decrease function. This means that the protein is effectively locked in the dimeric form at alkaline conditions, whereas pH 3.5 leads to rapid monomer formation and eventual aggregation of the protein. In a second investigation, we examined the effect of ‘channelizing’ CLC-ec1 by removing the external protonatable residue (E148A) and the residue that coordinates chloride in the central

site (Y445S). A similar construct, E148A/Y445A, has been shown to form an aqueous path along the membrane increasing the chloride transport rate 20-fold. FRET measurements of subunit exchange show that the reaction kinetics of E148A/Y445S are comparable to WT, and single molecule photobleaching analysis reports similar equilibrium constants. Therefore, our results demonstrate that the CLC dimer assembly is strongly linked to pH, with loss of transport function associated with locking the protein in a non-dissociable dimeric state, suggesting a difference in the dimeric state at pH 4.5 vs. pH 7.5. On the other hand, changing the transport mechanism by channelizing the ion binding pathway leads to no changes in dimerization stability or kinetics. This suggests that the subunits interact with each other in a similar manner despite significant changes along the internal transport pathway.

6.3 Introduction

Membrane transport proteins often exist in oligomeric structures and at a higher propensity than their soluble counterparts (1). In some cases, the assembled structure is clearly required for the protein's function. For example, the tetrameric potassium channel where the subunits come together to form the ion permeation pathway along the central axis of the oligomer (2). This type of assembly is common to many types of ion channels – TRP channels, connexins, pannexins, swell-activated channels, nicotinic acetylcholine receptors, NMDA channels.

However, there are many cases where the role of oligomerization is not immediately apparent, as is the case for the many proteins where each subunit contains a seemingly independent pore or transport pathway. For example, the LeuT-fold amino acid transporters, which appear as monomers, dimers and trimers throughout the structural database (3-5). Take the example of Aquaporin and FocA, which are water and formate channels respectively, assembled in tetrameric

and pentameric arrangements (6). In these cases, the role of oligomerization is not clear, which leads to two possibilities. It could be that the function of the monomer requires the higher-order assembly, or it is possible that each subunit has the capacity to function on its own, but that the oligomeric assembly confers the ability to regulate the overall function. For example, trimerization of the LeuT-fold betaine transporter BetP is required for osmoregulation (7), while other homologous transporters of the LeuT fold function as monomers (3). Just as is the case in cooperative mechanisms of oligomeric enzymes or binding proteins, such as hemoglobin, this introduces the ability for positive or negative cooperativity. Function can now be enhanced or shut off due to a stimulus, enabling switch like regulatory function to the transport behaviors.

The CLC family of ion channels and secondary active transporters presents an interesting question of the role of oligomerization in membrane transport. Amongst the 87 structures solved (8), the only naturally observed structure has been the dimeric complex, yet, the monomer is fully functional (9) and the two pores appear to behave in an independent manner (10). Why then have CLCs evolved to be dimer complexes despite the monomer being the minimal functional unit? As dimerization is not required for function, we hypothesize that dimerization in CLCs introduces the ability to regulate function in response to an environmental stimulus. In a broad sense, this is a mechanism where dimerization shifts the probability distributions of the overall conformational energy landscape of each subunit. For example, if conformational dynamics are required for something like transport, then dimerization has the potential to energetically constrain the functional conformations. In general, the function of CLCs have been shown to be susceptible to pH, voltage, and ionic concentration. They also exist in distinct functional forms, ion channels and secondary active transporters, despite having an overwhelmingly similar subunit structure. Several studies, including a recent structural investigation, have demonstrated that alternate dimeric forms

exist for both channels and transporter types. Finally, eukaryotic CLCs have additional cytosolic cystathionine- β -synthase (CBS) domains that dimerize and are also the site of many disease-causing mutations. Altogether, these findings suggest that there may be a link between dimerization and regulation of function. We hypothesize that the dimerization presents a mechanism for regulating the functional behavior of each subunit, and that we will be able to observe this connection through a change in the dimerization reaction under different functional conditions. For example, thermodynamic stability and subunit exchange kinetics might be stabilized for dimerization, thereby preventing dynamics to enable transport. Therefore, in this study, we investigate whether the nature of the dimer state, its stability and propensity to undergo and dynamic equilibrium reaction, depends on the different functional states of CLC-ec1.

In a first step towards understanding why CLCs have evolved to be dimeric, we start by examining whether different functional conditions of CLC-ec1 are linked to the dimerization reaction or stability. First, we titrated the environmental pH, where increases are known to decrease transport function (11), and study how this impacts dynamic nature of the dimerization reaction, by examining subunit-exchange kinetics using bulk FRET assays. Next, we examined whether there is a difference in the dimerization reaction between a CLC-ec1 construct that acts as a transporter compared to a channelized variant, examining both subunit exchange dynamics and thermodynamic stability at pH 4.5. Altogether, these two cases show examples of how functional regulation is, and is not linked to changes in dimerization, providing a foundation for future investigating into the role of oligomerization in CLCs.

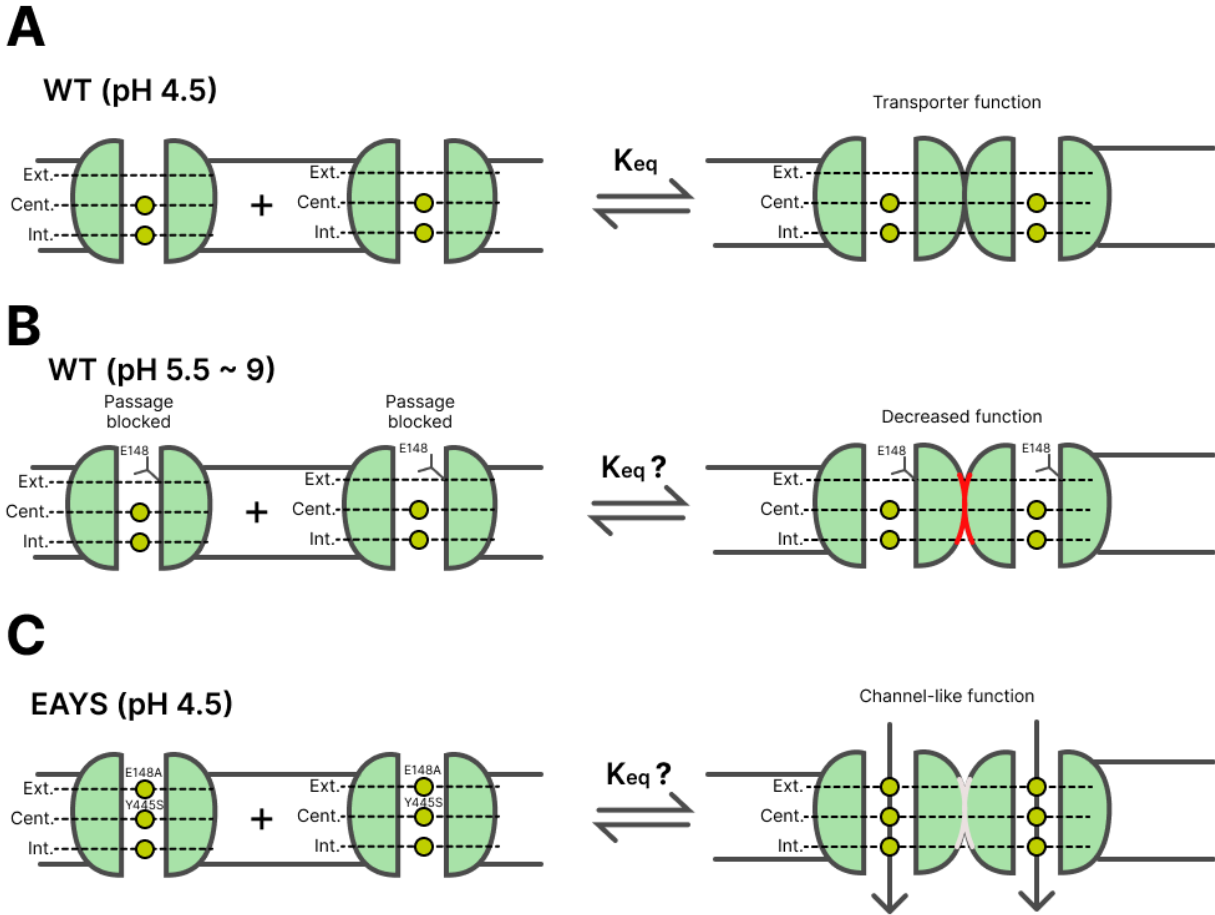


Figure 1. Hypothetical cartoon of dimerization reaction. (A) Dimerization reaction of transporter version (WT) CLC-ec1 at pH 4.5 (B) Hypothetical dimerization reaction of WT CLC-ec1 in the range from pH 5.5 to 9 which is known to decrease the functional activity and change the orientation of E148 at the external proton binding site (11, 12). We hypothesize that dimerization is locked at higher pH, and it will have higher thermodynamic stability by blocking the transport function (C) Hypothetical dimerization reaction of channel-like version (EAYS) CLC-ec1 at pH 4.5. There are mutations at E148A and at Y445S in the proton binding site and the central barrier of the pore, respectively. By mutating the external and central residues in the pore, CLC-ec1 shows a channel like functional activity (13). We hypothesize channel-like version of CLC (EAYS) will have less thermodynamic stability by letting dynamics to enable transport.

6.4 Materials and Methods

6.4.1 Protein purification

The CLC-ec1 constructs used in this study: C85A/H234C (WT), C85A/H234C/R230C/L249C (RCLC), C85A/H234C/E148A/Y445S (EAYS), and C85A/H234C/E148A/Y445S/R230C/L249C (EAYS/RCLC) were made by QuickChange (Agilent, Santa Clara, CA) and sequenced. They were expressed and purified with the methods previously used (14, 15). To briefly summarize the methods, BL21-AI *E. coli* cells were transformed with the expression plasmid, lysed using sonication, and the protein was extracted from membrane fragments using a solution containing 2% n-Decyl- β -D-Maltopyranoside (DM) and 5 mM TCEP to ensure that the cysteine residue introduced at residue 234 (H234C) remained in a reduced state for maleimide labeling. After removing cellular debris by centrifugation, the protein was purified using TALON cobalt affinity resin followed by size exclusion chromatography. The purified protein was then stored in a buffer containing 150 mM NaCl, 20 mM MOPS pH 7.0, and 5 mM analytical-grade DM, for future fluorophore labeling and reconstitution into liposomes. The molar extinction coefficients for the two types of proteins were also reported; the WT protein has an extinction coefficient of 46,020 M⁻¹ cm⁻¹ and a molecular weight of 52,000 g/mol, while the RCLC protein has an extinction coefficient of 49,630 M⁻¹ cm⁻¹ and a molecular weight of 49,630 g/mol. EAYS protein has an extinction coefficient 44,920 M⁻¹ cm⁻¹, molecular weight of 52,023 g/mol. EAYS protein has an extinction coefficient 44,920 M⁻¹ cm⁻¹, molecular weight of 52,023 g/mol. EAYS/RCLC protein has an extinction coefficient 44,920 M⁻¹ cm⁻¹, molecular weight of 51,960 g/mol.

6.4.2 Preparation of lipids

Lipid micelles solubilized with detergent were prepared according to a method described previously (14). In summary, a specific quantity of *E. coli* polar lipid extract (EPL; Avanti Polar Lipids Inc., Alabaster, AL) dissolved in chloroform (stock concentration of 25 mg/mL) was placed in a glass vial. The chloroform was removed by evaporating it under a continuous stream of Ultra High Purity N₂ gas (Airgas) filtered through a 0.22 µm filter. The lipids were then washed with pentane and dried by rotating the vial for approximately 10-12 minutes. This process resulted in a thin lipid film along the walls and bottom of the vial. The washing step was repeated twice, and then the lipid film was resuspended in 1x Dialysis Buffer (DB: 300 mM KCl, 20 mM citrate pH 4.5, adjusted with NaOH) to achieve a final concentration of 20 mg/mL. Subsequently, 35 mM of CHAPS detergent was added to the mixture. To solubilize the lipid/detergent combination, a cup-horn sonicator (Qsonica) was employed until the sample attained a uniform translucent appearance.

6.4.3 Protein labeling and reconstitution

Protein labeling and reconstitution methods were described in the previous literature (16). After undergoing size-exclusion chromatography to purify proteins, 10 µM protein was reacted with either 50 µM of Cy3- or 50 µM of Cy5-, or a 1:10 mixture of Cy3- and Cy5- (Cy3/5) maleimide in DMSO (Lumiprobe Corporation, Hunt Valley, MD). The reaction lasted for 10 minutes, then quenched by addition of 5 mM cysteine from a 100 mM cysteine stock in SEB. The pH of the solution adjusted to 7.0. To eliminate any unbound dye, the protein was rebound to a 0.2 mL cobalt affinity column (Talon), and extensively washed with 10-15 CV of cobalt column wash buffer (CoWB: 100 mM NaCl, 20 mM Tris, 5 mM DM, pH 7.5). Elution of the protein-dye complexes was achieved by using CoWB supplemented with 400 mM imidazole at pH 7.5. As a final step, the eluted sample underwent imidazole removal by passing it through a 3 mL Sephadex

G-50 size exclusion column (Sigma-Aldrich). The labeling yield was calculated by placing the sample in a 1 cm quartz cuvette in a Nanodrop 2000c UV-VIS spectrophotometer and measuring the absorbance spectrum from 190 to 840 nm. The protein concentration in the presence of Cy5 (or Cyanine 5) was calculated as follows:

$$[protein_{Cy5}] = \frac{A_{280} - (A_{Cy5,max} \times CF_{Cy5,280})}{\epsilon_{protein}} \quad (1)$$

where A_{280} is the absorbance at 280 nm, $A_{Cy5,max}$ is the peak absorbance of Cy5 \approx 653 nm, $CF_{Cy5,280} = 0.017$ ($CF_{Cy5,280} = 0.05$ for Cyanine 5), is the correction factor for the absorbance of Cy5 at 280 nm, and $\epsilon_{protein}$ is the extinction coefficient for the protein at 280 nm. The subunit labeling yield, P_{Cy5} , is calculated as:

$$P_{Cy5} = \frac{A_{Cy5,max}}{[protein_{Cy5}] \times \epsilon_{Cy5}} \quad (2)$$

where, $\epsilon_{Cy5} = 2.5 \times 10^5 \text{ M}^{-1} \text{ cm}^{-1}$ is the extinction coefficient for Cy5 at 653 nm. For the Förster Resonance Energy Transfer (FRET) studies, protein was labeled with Cy3-maleimide (Lumiprobe) or simultaneously co-labeled with Cy3- and Cy5-maleimide. For Cy3-labeling alone, the same procedure was followed, except that the quantification is corrected for Cy3 contribution at 280 nm. Thus, the protein concentration in the presence of Cy3 is calculated as:

$$[protein_{Cy3}] = \frac{A_{280} - (A_{Cy3,max} \times CF_{Cy3,280})}{\epsilon_{protein}} \quad (3)$$

where $A_{Cy3,max}$ is the peak absorbance of Cy3 ≈ 555 nm, and $CF_{Cy3,280} = 0.08$ is the correction factor for the absorbance of Cy3 at 280 nm. The subunit labeling yield, P_{Cy3} , is calculated as:

$$P_{Cy3} = \frac{A_{Cy3,max}}{[protein_{Cy3}] \times \epsilon_{Cy3}} \quad (4)$$

where, $\epsilon_{Cy3} = 1.5 \times 10^5 \text{ M}^{-1} \text{ cm}^{-1}$ is the extinction coefficient for Cy3 at 555 nm. For labeling of Cy3 and Cy5 simultaneously, there are two correction factors to consider, Cy3 and Cy5 absorbance at 280, as well as the contribution of Cy5 absorbance in the Cy3 peak. Thus, the protein concentration in the presence of Cy3 and Cy5 is calculated as:

$$[protein_{Cy3/Cy5}] \quad (5)$$

$$= \frac{A_{280} - ((A_{Cy3,max} - (A_{Cy5,max} \times CF_{Cy5,555})) \times CF_{Cy3,280}) - (A_{Cy5,max} \times CF_{Cy5,280})}{\epsilon_{protein}}$$

where $CF_{Cy3,555} = 0.08$ is the correction factor for the absorbance of Cy5 around the Cy3 peak.

The subunit labeling yield of Cy3 in the presence of Cy5, $P_{Cy3/Cy5}$, is calculated as:

$$P_{Cy3/Cy5} = \frac{(A_{Cy3,max} - (A_{Cy5,max} \times CF_{Cy5,555}))}{[protein_{Cy3/Cy5}] \times \epsilon_{Cy3}} \quad (6)$$

and the subunit labeling yield of Cy5 in the presence of Cy3, $P_{Cy5/Cy3}$, is calculated as:

$$P_{Cy5/Cy3} = \frac{A_{Cy5,max}}{[protein_{Cy3/Cy5}] \times \epsilon_{Cy5}} \quad (7)$$

Altogether, we obtained the following Cy5, Cy3, and co-labeled Cy3/5 labeling yields for WT CLC-ec1: $P_{Cy5} = 0.70 \pm 0.02$ (n = 16), $P_{Cy3} = 0.70 \pm 0.01$ (n = 14), $P_{Cy5}/P_{Cy3} = 4.8 \pm 0.2$ (n = 14) ($P_{Cy3} = 0.12 \pm 0.00$, $P_{Cy5} = 0.56 \pm 0.02$, respectively). For RCLC CLC-ec1, we obtained the following Cy5, Cy3, and co-labeled Cy3/5 labeling yields: $P_{Cy5} = 0.63 \pm 0.11$ (n = 2), $P_{Cy3} = 0.72 \pm 0.01$ (n = 2), $P_{Cy5}/P_{Cy3} = 5.2 \pm 0.2$ (n = 2) ($P_{Cy3} = 0.12 \pm 0.00$, $P_{Cy5} = 0.64 \pm 0.01$, respectively). For EAYS CLC-ec1, we obtained the following Cy5, Cy3, and co-labeled Cy3/5 labeling yields: $P_{Cy5} = 0.67 \pm 0.02$ (n = 12), $P_{Cy3} = 0.74 \pm 0.02$ (n = 8), $P_{Cy5}/P_{Cy3} = 4.4 \pm 0.3$ (n = 8) ($P_{Cy3} = 0.13 \pm 0.01$, $P_{Cy5} = 0.57 \pm 0.03$, respectively). Finally, for EAYS/RCLC CLC-ec1, we obtained the following Cy5, Cy3, and co-labeled Cy3/5 labeling yields: $P_{Cy5} = 0.68 \pm 0.11$ (n = 6), $P_{Cy3} = 0.65 \pm 0.05$ (n = 5), $P_{Cy5}/P_{Cy3} = 5.4 \pm 0.3$ (n = 5) ($P_{Cy3} = 0.11 \pm 0.01$, $P_{Cy5} = 0.61 \pm 0.04$, respectively).

For bulk FRET experiments, co-labeled samples were prepared by reconstituting the proteins at a concentration of 1 $\mu\text{g}/\text{mg}$, $\chi = 10^{-5}$ subunits/lipid in EPL/CHAPS micelles. Subsequently, these samples were dialyzed in dialysis buffer in the absence of light at a temperature of 4 $^{\circ}\text{C}$. The ratio of the sample volume to the dialysis buffer volume was maintained at 1000-fold, with 5 buffer changes over a period of 48-72 hours. For the WT_{Cy3} + WT_{Cy5} fusion experiments using proteoliposomes, the same concentration sample of 1 $\mu\text{g}/\text{mg}$, $\chi = 10^{-5}$ subunits/lipid in EPL/CHAPS micelles was used. However, separate volumes were prepared for WT_{Cy3} and WT_{Cy5} liposomes, corresponding to a final acceptor to donor ratio that matches the co-labeled P_{Cy5}/P_{Cy3} ratio. For example, if the P_{Cy5}/P_{Cy3} ratio was 6 for the co-labeled sample, and the independently labeled samples had $P_{Cy3} = 0.80$ and $P_{Cy5} = 0.65$, then 100 μL of WT_{Cy3} liposomes and 747 μL of WT_{Cy5} liposomes were prepared and dialyzed separately. After dialysis, the full

volumes of each sample were mixed for the "fused" samples followed by freeze-thaw. This approach ensured that the resulting fused samples had a P_{Cy5}/P_{Cy3} ratio of approximately 6, regardless of any variation in lipid concentration during dialysis. The proteoliposomes were retrieved from the dialysis process to make pauci-lamellar vesicles (PLVs) through freeze-thaw cycles. They were then gone through freeze/thaw cycles, alternating temperatures between -80 °C and room temperature. Each cycle includes freezing at -80 °C for 15 minutes followed by thawing at room temperature for 20 minutes. This freeze-thaw process was repeated twice, and the samples were stored at -80 °C until further use. In this paper, "Room Temperature" refers to the ambient temperature of the laboratory, around 22 °C.

WT-Cy5 and EAYS-Cy5 protein was prepared with 20 mg/mL EPL/CHAPS micelles at 0.0001, 0.001, 0.01, and 0.1 $\mu\text{g}/\text{mg}$, corresponding to $\chi = 10^{-9}$, 10^{-8} , 10^{-7} and 10^{-6} subunit/lipid mole ratio for the single-molecule photobleaching experiment.

6.4.4 pH titrations

We use two different approaches to adjust pH of our samples either prepared at the final pH or shifted to the final pH. First, Cy5 labeled and Cy3 labeled samples were dialyzed in 1x dialysis buffer (KCl 300 mM, Citrate 20 mM, MES 10 mM, HEPES 20 mM) at pH 3.5, 4.5, 5.5, 6.5, 7.5 individually to prepare at the final pH. On the other hand, Cy5 labeled and Cy3 labeled samples were dialyzed in 1x dialysis buffer (KCl 300 mM, Citrate 20 mM, MES 10 mM, HEPES 20 mM) after reconstitution at pH 4.5 before shifting the pH to the final pH. Samples were taken out after 5-6 cycles of dialysis and mixed. H_2SO_4 was added to buffer to make pH 3.5, NaOH was added to the buffer to make pH 5.5, 6.5, 7.5 samples. Finally, samples are freeze/thawed 3 times for bulk FRET experiment and chloride transport function experiment.

6.4.5 Bulk FRET measurements in pauci-lamellar vesicles

FRET was measured for proteoliposomes that were fused or co-labeled in the state of pauci-lamellar vesicles (PLV). This assessment was conducted using a TECAN Spark microplate readers equipped with filter based QuadX monochromator based fusion optics. Samples were excited at 534 nm with bandwidth 5.0nm, and spectra was collected from 553 - 740 nm, with bandwidth 7.5 nm with step size 4. Generally, 0.1 μ L of PLVs were injected into each well, and the fluorescent intensity was measured, and the ratiometric FRET signal was calculated as follows:

$$FRET\ signal = \frac{I_{Cy5,max}}{I_{Cy3,max} + I_{Cy5,max}} \quad (8)$$

For this bulk FRET study, WT_{Cy3/Cy5}, WT_{Cy3+Cy5^{fused}}, RCLC_{Cy3/Cy5}, RCLC_{Cy3+Cy5^{fused}}, EAYS_{Cy3+Cy5^{fused}}, EAYS/RCLC_{Cy3/Cy5}, EAYS/RCLC_{Cy3+Cy5^{fused}} were prepared at 1 μ g/mg, $\chi = 10^{-5}$ subunits/lipid in EPL, in the PLV state. Initial FRET data points were collected at 22 °C before freeze/thaw cycle followed by post 3x freeze/thaw. After that, the samples were incubated at 37 °C in the benchtop incubator, in the dark, and the FRET data was collected every hour. Before fitting the data, the FRET signals were normalized by setting the first time point value of WT_{Cy3+Cy5^{fused}} or EAYS_{Cy3+Cy5^{fused}} to 0 where the samples have been measured right after the freeze-thaw procedure, and the first time point value of WT_{Cy3/Cy5} and EAYS_{Cy3/Cy5} end-point control sample to 1. To fit the time invariant traces such as RCLC_{Cy3/Cy5}, EAYS-RCLC_{Cy3/Cy5}, RCLC_{Cy3+Cy5^{fused}}, EAYS-RCLC_{Cy3+Cy5^{fused}}, WT_{Cy3/Cy5}, and EAYS_{Cy3/Cy5} traces, the data was fit to a horizontal line, *Norm. FRET signal* = *b*, where *b* represents the average value of the data points. In order to investigate the subunit exchange kinetic stability of the WT_{Cy3+Cy5^{fused}} or EAYS_{Cy3+Cy5^{fused}} samples, the time-course FRET signal was fit to one-phase association equation, *Norm. FRET signal* = *Y*₀ * (*Plateau* - *Y*₀) * (1 - *e*^{-*kt*}), with the initial value, *Y*₀, set to 0.

6.4.6 Single-molecule subunit capture photobleaching experiment

The specifics of this technique have been previously explained (14, 17). In the current study, EAYS CLC-ec1 is labeled with Cy5 and reconstituted from $\chi = 10^{-9}$ to 10^{-6} subunits/lipid which corresponds to 0.0001 – 0.1 $\mu\text{g}/\text{mg}$ of protein per lipid. The reconstituted proteoliposomes are freeze-thawed (FT) to create large pauci-lamellar vesicles (PLVs) where subunits can exchange and reaction can occur. The way the subunits are distributed among the vesicles follows a distribution that is similar to the Poisson distribution and is influenced by the pre-existing distribution of oligomers in the larger membranes. Here we quantify the photobleaching probability distributions of Cy5 attached subunits per liposome by conducting single-molecule photobleaching experiment using total internal reflection fluorescence microscope (TIRF). MATLAB based analysis program was used to analyze the image taken from the microscope (18). It auto-selects fluorescent spots by threshold intensity in the 4 x 4 pixel area around the peak intensity, and the integrated intensity of each selected spot was analyzed intensity over time. The photobleaching step of each spot was manually counted using 200~300 spots. With the photobleaching distributions at each density, the fraction of dimer, F_{Dimer} , is calculated. Experimental photobleaching distributions of ideal monomer control (P_M), IWIW, in EPL and experimental photobleaching distributions of ideal dimer control (P_D), RCLC, in EPL were used for least squared analysis to estimate the value of F_{Dimer} . Finally, F_{Dimer} vs χ^* was fit to calculate the equilibrium constant and the free energy of the system with $\chi^\circ = 1$ subunit/lipid standard state. To calculate the equilibrium constant (K_{eq}) for each sample, previously introduced bootstrap fitting analysis method (16) was used with a written script in MATLAB. The analysis was carried out on the entire F_{Dimer} , vs. χ^* data set, randomly selecting 8 data points out of total 12 data points to fit to the dimerization isotherm:

$$F_{Dimer} = \frac{1 + 4\chi^*K_{eq} - \sqrt{1 + 8\chi^*K_{eq}}}{4\chi^*K_{eq}} \quad (9)$$

6.5 Results

6.5.1 CLC-ec1 dimerization is linked to pH

Previously, it has been shown that CLC-ec1 is a pH regulated chloride transporter (19), where the unitary transport activity increases under acidic conditions. Maximal activity is observed around pH 4.5, while chloride transport is reduced as pH increases towards neutral conditions, around pH ~7.5 (11). The actual mechanism of pH regulation of function is not clearly known, as residues involved have not been identified because of a lack of sided reconstitution studies. However, there still have been several studies reported to identify the mechanism of pH regulation of function. The study reports a conformational change in the orientation of Glu_{ex} (E148) at different pH range from 5.5 to 9 based on the crystallographic structure of CLC-ec1 (12). A conserved glutamate residue, Glu_{ex} (E148) is known as an external intermediate proton binding site, and it blocks the passage of ions through the extracellular side of the pathway (20, 21). Another study report that when the E148A mutation is present, the pH sensitivity of the currents is completely eliminated and they become almost exclusively selective to Cl⁻ (22). This suggests that CLC-ec1 function could be regulated by the pH environment.

To examine the relationship between dimerization and function, we carried out an experiment by testing whether dynamic subunit exchange occurs under the different pH conditions (**Fig. 2**). This experiment was introduced previously by examining the subunit exchange at different temperatures in a van 't Hoff analysis of the in-membrane binding (16). Here, samples were examined in two ways, either prepared at the final pH or shifted to the final pH. The results

demonstrate a dependency of the heterodimeric FRET signal on pH, and a reduction in exchange capacity as the pH is increased to 7.5, alongside a decrease in transport function. At pH 3.5, WT co-labeled sample shows sudden drop of the signal which could indicate the dissociation of the subunits at the beginning. Both WT fused and co-labeled sample showed increase in FRET signal surpassing the value 1 suggesting the protein aggregation. At pH 4.5, we observed FRET signal converging to the dimerization equilibrium endpoint as it was previously reported (16). At pH 5.5, WT co-labeled sample showed slightly increase FRET signal compared to the signal at pH 4.5. We observed the signal convergence for both WT co-labeled and fused sample, but it shows there is a small amount of proteins aggregating. From pH 6.5 and above, we do not observe any subunit exchange reaction happening which could potentially indicate the construct of a locked-in dimer. With this, we conclude that the pH which corresponds to a loss in transport function, kinetically trap the dimer state, at least on the observed timescale. This suggests either a different conformation of the dimer at high pH that is much more stable, or the dimer provides a way of locking in the complex, perhaps preventing the conformational changes required for transport. In any case, these results show a clear link between the propensity to participate in a dimerization equilibrium reaction and the conditions that regulate functional activity. Since subunit exchange was not observed across the pH range studied, we limited the investigation here and did not carry out further examination of the stability.

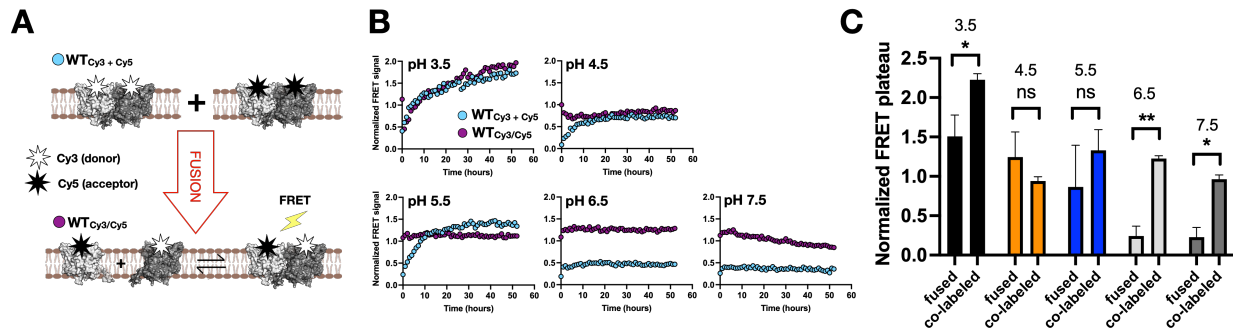


Figure 2. CLC dimerization is strongly linked to environmental pH. (A) Cartoon representing the subunit exchange reaction. (B) Representative traces of time-dependent normalized FRET data of CLC-ec1 (co-labeled, fused) from pH 3.5 to pH 7.5 at 37 °C. (C) Summary of normalized plateau data and time constants ($n = 2-6$). The FRET signal = $I_{665nm}/(I_{565nm} + I_{665nm})$ shows a significant difference between fused and co-labeled in the end of FRET experiment for WT pH 3.5 (*, $p = 0.04$), pH 4.5 (ns, $p = 0.4714$), pH 5.5 (ns, $p = 0.44$), pH 6.5 (**, $p = 0.009$) and pH 7.5 (*, $p = 0.03$).

6.5.2 CLC-ec1 dimerization is independent of channel-like activity

The broader CLC superfamily contains both ion channels and transporters, reflecting two distinct mechanisms of membrane transport. An ion channel mechanism requires an aqueously accessible pathway where ions can diffuse down its electrochemical gradient. On the other hand, a transporter provides alternate access to each side of the membrane, without a continuous pathway that would otherwise dissipate chemical gradients, including those needed to drive uphill transport. A general assumption is that transporters employ conformational changes during the translocation step, while channels conformations are disfavored during the permeating conductive state. This inherent difference in conformational flexibility as part of the functional mechanism, suggests that CLCs may reflect different dimerization assemblies to yield channel or transporter function. For instance, if the role of the dimer is to conformationally restrain each individual subunit, then we would expect that the transport-competent CLC-ec1 under activating conditions may be less stable than the channel variant of CLC-ec1.

To investigate this, we first needed to identify a CLC construct that could exhibit both transporter and channel-like properties. For this, we turned to previous results on the channelization of CLC-ec1 (13). In this study, key residues along the chloride transport pathway were substituted to smaller side-chains, namely E148A at the external site gate, and Y445S, the coordinating central site. A structure of a similar double mutant E148A/Y445A revealed a continuous water accessible pathway through each subunit that is large enough to accommodate a chloride ion and exhibited an increase in the chloride efflux rate > 20 -fold, to $\sim 35,000 \text{ Cl}^- \text{ ions s}^{-1}$. The double mutant E148A/Y445S (EAYS) showed even higher efflux rates, and reduced coupling to proton movement, indicating that it is a channel-like version of CLC-ec1 (13). With this, we investigated whether the channelized version of CLC-ec1, EAYS, still participates in a dynamic dimerization reaction by examining subunit exchange by bulk FRET studies. Addition of two exposed cysteines at the dimerization interface, R230C and L249C (RCLC) allow for spontaneous covalent disulfide formation (23), locking the protein in the dimeric state. Examining the changes in the FRET signal of RCLC and EAYS-RCLC, fused (Cy3+Cy5) and co-labeled (Cy3/5) samples after freeze/thaw fusion of membranes shows the FRET signals but no time dependency that would indicate subunit swapping (**Fig. 3A**). However, EAYS exhibits dynamic subunit exchange within the same subunit exchange range observed for WT CLC-ec1 (**Fig. 3A**), converging to the dimerization equilibrium endpoint. By fitting the traces with one-phase association functions, we observed that the subunit exchange kinetics for both WT and EAYS are not significantly different (**Fig. 3C**).

With evidence of dynamic subunit assembly in the membrane, we carried out a study of the equilibrium dimerization reaction by single-molecule subunit capture where samples are in the equilibrium state (**Fig. 3D**). We observed no change in both thermodynamic and kinetic stability

between channel version of CLC-ec1 (EAYS) and the transporter version of CLC-ec1 (WT). WT CLC had a stability with $K_D = 2.3 \pm 1.4 \times 10^{-10}$ subunits/lipid and $\Delta G^{\circ}_{WT \text{ in EPL}} = -13.1 \pm 0.3$ kcal/mole, also EAYS CLC had a stability with $K_D = 2.4 \pm 1.2 \times 10^{-10}$ subunits/lipid and $\Delta G^{\circ}_{EAYS \text{ in EPL}} = -13.1 \pm 0.3$ kcal/mole. For the subunit exchange kinetic stability, WT CLC had a $t_{1/2} = 18.7 \pm 1.5$ h, and EAYS CLC had $t_{1/2} = 18.8 \pm 7.4$ h. Therefore, there were no observable differences in subunit exchange kinetics or equilibrium stability of the transporting or channelized version of the protein under activating pH conditions.

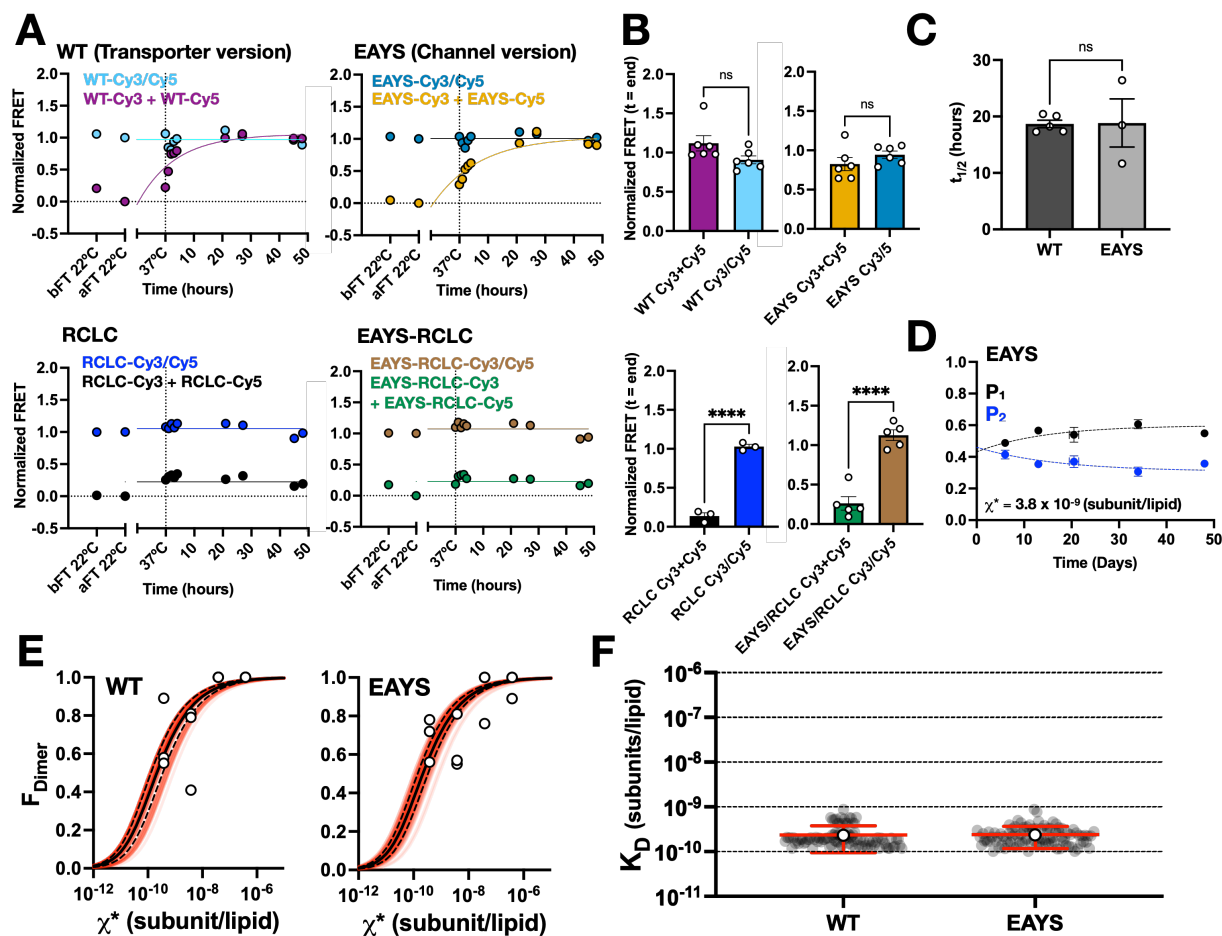


Figure 3. A stability of channel version of CLC-ec1 is independent of activating condition. (A) Time-dependent normalized subunit exchange FRET data of transporter version CLC-ec1 (WT) and channel version of CLC-ec1 (EAYS) at pH 4.5. (B) Endpoint normalized FRET signals, defined from the plateau value for the exponential fit to show convergence of the signal (C) $t_{1/2}$ for WT and EAYS calculated from the one-phase association fitting from Cy3+Cy5 traces (D) Photobleaching probability distributions (P₁ and P₂) of EAYS as a function of time, showing the equilibration after 48 days of incubation (E) Equilibrium dimerization isotherms from subunit capture photobleaching analysis. Data (WT: n=3, EAYS: n=3) represent independently prepared samples with WT (Left) and EAYS (Right) after incubation at RT for 3-5 days and 48 days respectively. Red lines indicate bootstrap fitting of the experimental data to the equilibrium dimerization isotherm in MATLAB, with 12 data points (67% of total) selected at random from a total set of 15, iterated 100 times and limits = $\{10^{-10}, 10^{-5}\}$. Black line indicates direct non-linear fitting of all experimental data to the dimerization isotherm with GraphPad Prism. (F) Comparison of K_D between transporter version (WT) and channel version (EAYS) of CLC-ec1 obtained from the bootstrapping analysis.

6.6 Discussion

CLC has been demonstrated to have independently functioning subunits raising the question of why they appear to have evolved so reliably in the dimer form. While we have not examined all structures experimentally, really only a glaringly small subset, every native CLC structure determined so far has been as a dimer assembly. In addition, previous stability studies indicate that the thermodynamic affinity is so strong that the protein would be found in a dimeric form in most biological situations. Furthermore, we see that all eukaryotic CLCs have cytosolic dimerization domains, further emphasizing that dimerization is important for these proteins on some level.

Altogether, the results from this study demonstrate that dimerization is strongly impacted by pH but not by different functional mechanisms, i.e., channel vs. transporter. For the pH regulation, the changes we observe imply that there are structural differences in the dimer complex that preclude the dimerization or kinetically trap the subunits together. At activating pH, the dimer is stable but is dynamic, with subunits capable of associating and dissociating. The fact that RCLC is still a functional transporter at pH 4.5, but the dimerization is locked at pH 7.5, suggests that there are different factors at play. It would be beneficial to further investigate the major player in pH sensitivity changes, for instance specific residues that might become protonated as the pH is reduced. In addition, in order to determine what locks the subunit into an inactive form, future structural studies would be useful.

The study of the channelized form of CLC also reveals that the transport vs. channel-like mechanism does not appear to be inherently linked to dimerization. This is interesting as one might consider that the transport and channel mechanisms correspond to differences in subunit dynamics. Still, CLC-ec1 is a transporter that is notorious for its limited conformational changes, and so it is

possible that the channelized EAYS construct still maintains similar conformational changes. To expand on these studies further, it would be beneficial to investigate whether the EAYS CLC-ec1 channel construct maintains the pH regulatory behavior that was observed in the wild-type transporter. Observing changes in subunit exchange kinetics and dimer stability in EAYS construct at different pH from 4.5 to 7.5 would offer the ability to dissect pH titrated residues that define dynamic dimerization from the residues that are involved in the transport mechanism.

6.7 Conclusion

This study demonstrates that CLC dimerization strongly linked to the pH from our FRET subunit exchange experiment. We observe that the subunits become an inactive state showing pH sensitivity in subunit exchange. Finally, we find that the kinetic and thermodynamic stabilities of CLC-ec1 are independent of activating condition, showing that activating condition is not a main reason for CLC-ec1 dimerization.

References

1. A. A. Aleksandrova, E. Sarti, L. R. Forrest, MemSTATS: A Benchmark Set of Membrane Protein Symmetries and Pseudosymmetries. *J Mol Biol* **432**, 597-604 (2020).
2. D. A. Doyle *et al.*, The structure of the potassium channel: molecular basis of K⁺ conduction and selectivity. *Science* **280**, 69-77 (1998).
3. K. N. Kazmier (2013) Revealing the Mechanistic Diversity of the LeuT Fold: A Comparative Analysis of the Leucine Transporter and the Hydantoin Transporter using Electron Paramagnetic Resonance Spectroscopy.
4. L. Ponzoni, S. Zhang, M. H. Cheng, I. Bahar, Shared dynamics of LeuT superfamily members and allosteric differentiation by structural irregularities and multimerization. *Philos Trans R Soc Lond B Biol Sci* **373** (2018).
5. C. Perez, C. Koshy, O. Yildiz, C. Ziegler, Alternating-access mechanism in conformationally asymmetric trimers of the betaine transporter BetP. *Nature* **490**, 126-130 (2012).
6. Y. Wang *et al.*, Structure of the formate transporter FocA reveals a pentameric aquaporin-like channel. *Nature* **462**, 467-472 (2009).
7. C. Perez, K. Khafizov, L. R. Forrest, R. Kramer, C. Ziegler, The role of trimerization in the osmoregulated betaine transporter BetP. *EMBO Rep* **12**, 804-810 (2011).
8. T. J. Jentsch, M. Pusch, CLC Chloride Channels and Transporters: Structure, Function, Physiology, and Disease. *Physiol Rev* **98**, 1493-1590 (2018).
9. J. L. Robertson, L. Kolmakova-Partensky, C. Miller, Design, function and structure of a monomeric CLC transporter. *Nature* **468**, 844-847 (2010).
10. M. Maduke, C. Miller, J. A. Mindell, A decade of CLC chloride channels: structure, mechanism, and many unsettled questions. *Annu Rev Biophys Biomol Struct* **29**, 411-438 (2000).
11. H. H. Lim, C. Miller, Intracellular proton-transfer mutants in a CLC Cl⁻/H⁺ exchanger. *J Gen Physiol* **133**, 131-138 (2009).
12. T. S. Chavan *et al.*, A CLC-ec1 mutant reveals global conformational change and suggests a unifying mechanism for the CLC Cl⁻/H⁺ transport cycle. *Elife* **9** (2020).
13. H. Jayaram, A. Accardi, F. Wu, C. Williams, C. Miller, Ion permeation through a Cl⁻-selective channel designed from a CLC Cl⁻/H⁺ exchanger. *P Natl Acad Sci USA* **105**, 11194-11199 (2008).

14. R. Chadda *et al.*, The dimerization equilibrium of a CLC Cl(-)/H(+) antiporter in lipid bilayers. *Elife* **5** (2016).
15. R. Chadda, L. Cliff, M. Brimberry, J. L. Robertson, A model-free method for measuring dimerization free energies of CLC-ec1 in lipid bilayers. *J Gen Physiol* **150**, 355-365 (2018).
16. R. Chadda *et al.*, A thermodynamic analysis of CLC transporter dimerization in lipid bilayers. *Proc Natl Acad Sci U S A* **120**, e2305100120 (2023).
17. R. Chadda, J. L. Robertson, Measuring Membrane Protein Dimerization Equilibrium in Lipid Bilayers by Single-Molecule Fluorescence Microscopy. *Methods Enzymol* **581**, 53-82 (2016).
18. L. J. Friedman, J. Gelles, Multi-wavelength single-molecule fluorescence analysis of transcription mechanisms. *Methods* **86**, 27-36 (2015).
19. Z. Yue, A. Bernardi, C. H. Li, A. V. Mironenko, J. M. J. Swanson, Toward a Multipathway Perspective: pH-Dependent Kinetic Selection of Competing Pathways and the Role of the Internal Glutamate in Cl-/H+ Antiporters. *Journal of Physical Chemistry B* **125**, 7975-7984 (2021).
20. R. Dutzler, E. B. Campbell, M. Cadene, B. T. Chait, R. MacKinnon, X-ray structure of a CLC chloride channel at 3.0 Å reveals the molecular basis of anion selectivity. *Nature* **415**, 287-294 (2002).
21. R. Dutzler, E. B. Campbell, R. MacKinnon, Gating the selectivity filter in CLC chloride channels. *Science* **300**, 108-112 (2003).
22. A. Accardi, L. Kolmakova-Partensky, C. Williams, C. Miller, Ionic currents mediated by a prokaryotic homologue of CLC Cl- channels. *J Gen Physiol* **123**, 109-119 (2004).
23. W. Nguitragool, C. Miller, CLC Cl/H+ transporters constrained by covalent cross-linking. *Proc Natl Acad Sci U S A* **104**, 20659-20665 (2007).

Chapter 7: Impact of this Work on Understanding Membrane Protein Folding in Membranes and Future Directions for the Field

7.1 Broad Impact of Dynamic CLC-ec1 Dimerization in Membranes

The work presented in this thesis shows that thermodynamic and kinetic analyses of large membrane protein complex formation inside of the membrane is possible just as it has been carried out to study soluble proteins in the past. Numerous technical challenges had to be overcome to translate these studies to the membrane, thus this work marks a technological milestone quantitative analysis of membrane reactions possible. While CLC-ec1 represents a model system in our hands, it opens new possibilities that dynamic, reversible equilibrium of biologically relevant protein complexes occurs more widely in cellular membranes but has yet to be studied. In fact, CLC-ec1 does represent a biologically important transporter in *E. coli*, involved in the extreme acid resistance response (1) and it is homologous to the 9 different CLC variants expressed in our bodies (2). The fact that CLC-ec1 dimerization is reversible, thermodynamically driven and exhibits slow kinetics (3) may all be meaningful aspects of CLC assembly, function, and degradation. Therefore, this work in CLC-ec1 will build important bridges of understanding of the assembly of other CLC variants, and could further help understand the human CLC diseases such as osteopetrosis, Dent's disease, and retinal degeneration (4).

7.2 Thermodynamic Dissection of CLC-ec1 Dimerization in Membranes Uncovers a Generalizable Driving Force for Assembly in Membranes

The thermodynamic analysis of CLC-ec1 dimerization presented in Chapter 4 reveals that binding follows a non-linear van 't Hoff relationship in both *E. coli* polar lipids and the synthetic mimic, 2:1 POPE/POPG. The non-linearity indicates a large negative heat capacity change in the direction of dimerization of 1.7-2.0 kcal⁻¹ mol⁻¹ K⁻¹. This was a surprising result as this sort of negative, large heat capacity change has been observed for soluble protein assembly (5) and is largely attributed to the hydrophobic effect that arises from the favorable burial of non-polar groups from water (6, 7). Yet, the CLC-ec1 dimerization reaction only occurs in the membrane, where the two non-polar interfaces go from lipid solvated to buried states, and it was expected that not much water was involved, at least not the same amount that would participate in soluble protein association reactions. Here, the lipid and water act as solvent molecules, and so this raises the question of whether changes in lipid organization and binding networks could also add to the heat capacity changes reminiscent of the water dependent hydrophobic effect.

Another study examined the dimerization free energy of a synthetic transmembrane helix (AALALAA)₃ measured in C14 to C22 PC membranes across different temperatures (8, 9), and the group concludes that its dimerization shows linear temperature dependencies in C14 to C20 membranes. However, in longer C22 lipids, which are hydrophobically mismatched to the dimer state, the van 't Hoff plot becomes non-linear showing a heat capacity change of +0.6 kcal mol⁻¹ K⁻¹ in the dimerization reaction. Therefore, the heat capacity change in this case appears to arise in the context of the lipid bilayer and specifically the hydrophobic mismatch that is introduced.

In addition, previous studies of coarse-grained MD simulations of CLC-ec1 in lipid bilayers shows that the dimerization interface is also hydrophobically mismatched to the

surrounding PO lipid bilayer (10). As a result, the lipids solvating the binding surface in the monomeric state are tilted, resulting in an overall thinning of the membrane, and a general non-bilayer structure. Lipids also exhibit a decrease in packing with reduced density and more interactions with the other leaflet. Yet, in the dimer state, this protein interface becomes buried, and this defect is eliminated, with the surrounding protein-lipid interface being well matched to the surrounding membrane thickness. The CLC-ec1 dimerization interface is formed by four helices, and is much larger than that of the single-pass poly-ALA-LEU helix, and so it is reasonable to conceive that if transmembrane helix dimerization offers a heat capacity change of $0.6 \text{ kcal mol}^{-1} \text{ K}^{-1}$ (8, 9), then CLC-ec1 might exhibit four times this contribution, in the range of $2.4 \text{ kcal mol}^{-1} \text{ K}^{-1}$. Of course, this is a rough estimate that requires more understanding about the molecular changes in the lipid solvation in the case of the single-pass transmembrane helix complexes but places our values in a comparable range.

Another finding of the computational study was that there is water penetration of the acyl-chain into the interior of the bilayer because of the decrease in lipid density, causing the lipids to splay out to fill a non-bilayer defect (10). This could certainly add to the heat capacity change observed as it would reflect the true hydrophobic effect, from the perspective of water entering the hydrophobic core of the bilayer. Interestingly, the same study also examined differential lipid solvation by testing of titrations of short-chain di-lauryl (DL) lipids in both the experiments and molecular dynamics studies. They found that DL lipids destabilize dimerization by a mechanism of preferential solvation, and the simulations demonstrate that the DL lipid acts as a more energetically favorable solvent for the non-bilayer defect of the monomeric state. Analysis of water in the mixed DL/PO membranes shows that there is less water penetrating the hydrophobic core, indicating better packing of DL lipids in this region and rationalizes the energetic stabilization (10).

With our previous findings, the result could indicate that the water penetration into the membrane occurs in regions where there is a deformation and lipid tilting with longer chain lipids, leading to a large negative heat capacity change in the dimerization reaction. This would also allow us to investigate whether the heat capacity change is linked to water penetration or the lipid membrane solvent. If the heat capacity change is primarily contributed by water penetration into the membrane crevice, then I predict that future van 't Hoff studies on WT CLC-ec1 within a membrane with shorter lipid chain such as DL would convert these curves to more linear relationships.

7.3 Dependency of CLC-ec1 Dimer Stability on Lipid Composition

Another important finding that arose from the thermodynamic analysis of CLC-ec1 dimerization presented in Chapter 4 reveals that the EPL lipid environment has a stabilizing effect on the CLC-ec1 dimerization, with $K_{eq} = 5.3 \pm 1.9 \times 10^9$ lipids/subunit and $\Delta G^{\circ}_{EPL} = -13.1 \pm 0.3$ kcal/mole, compared to the previously reported 2:1 POPE/POPG, resulting in a stabilization of $\Delta\Delta G_{EPL-2:1\ POPE/POPG} = -2.3$ kcal/mole as presented in **Table S2** of Chapter 4. EPL is a native mimic of *E. coli* membrane, and it is a crude extract containing ~67% PE, 20% PG, and 10% cardiolipin. I hypothesize that stability of CLC-ec1 comes from the different composition in the membrane. Following the previous work showing that short-chain lipids, such as DL, can have a destabilizing effect on dimerization, this demonstrates a stabilizing effect can also be imposed by lipids. It would be informative to study the effect of bovine cardiolipin on thermodynamic and kinetic stabilities by titrating the cardiolipin in a similar manner that was previously introduced with DL lipids (10).

This will provide valuable insights into how different lipid structures affect the stability of the membrane protein.

7.4 Implications and Possible Mechanisms of Slow Kinetics of CLC-ec1 Assembly in Membranes

Another striking result that was previously observed (3) and reproduced in Chapter 4 by the subunit-exchange assays, is the incredibly slow kinetics for CLC dimerization in membranes (11). While we have not carried out a complete kinetic analysis of the reaction rates, what we observe in the subunit exchange from the bulk FRET assays is mainly the dissociation kinetics (12), but is also dependent on other variables such as the labeling ratio of the donor and acceptors (13). Therefore, future studies focusing on kinetic analysis on the WT CLC-ec1, allowing for dissection of dissociation and association reaction rate constants would be necessary to fully understand what is defining the slow kinetics.

Still, subunit-exchange provides access to the kinetic analysis at least on a qualitative level and provides a means of investigating what defines the anomalously slow behavior in membranes. To note, this is something that has been observed before for membrane protein complexes, notably described in a previous study. Jefferson et al. showed steric-trapping studies of diacylglycerol kinase (DGK) trimers reporting that DGK activities and subunit compositions remain unchanged over the 2 days incubation period at 37°C, representing slow subunit exchange kinetics (14). This suggests that slow kinetics for large membrane protein complex reactions might be the standard, further warranting a deeper investigation into what determines the speed of such reactions.

In Chapter 5, I begin to investigate this by developing a hypothesis that the slow speed of CLC-ec1 dissociation is related to high energy barriers provided by partial lipid solvation states, and the solvation/desolvation steps that define the transition from dissociated to associated forms.

This assumes that at some point, lipids must move into tight spaces to solvate the protein interface, but these states are challenging to access as the lipids are sterically and possible, entropically restricted. Thus, there will be states that are poorly solvated, losing protein and lipid interactions providing a series of higher energy states in between the two reaction endpoints. The first step in investigating this is to identify whether the density of lipids change in states that are potentially confining along the reaction pathway. Extending this hypothesis further, this raises a question “Do smaller lipids and non-polar molecules speed up the subunit-exchange kinetics by reducing the cavity volume on the transition energy state?”. Our findings in Chapter 5, presented in **Figure 5-7C**, we report that smaller size molecules with a higher concentration have a higher packing density by occupying cavities at the dimerization interface between the CLC subunits in the system. The result may indicate that the changes in cavity volume between the subunits leads to faster kinetics in dimerization, but we still do not have the clear answer. Here we ask, does the increased packing density really come from the smaller size molecules coming into the small cavity between the dimerization interface? Therefore, future studies would benefit from calculating the molecular packing density in the bulk environment with the same size box as in the dimerization to evaluate more specifically the effect of small molecules depending on the inter-subunit distances by comparing the densities. As we presented in **Figure 5-8**, even though we observed slight but not significant increase in the subunit exchange kinetics, we have not clearly identified if the small molecules really increase the kinetics. The research would benefit if we could do more subunit exchange experiment using different types of small molecules such as benzene, ethanol, and different types of lysolipids with bulk FRET assays to correlate the kinetic information with the cavity volume between the subunits. Such a characterization on kinetics will allow us to map out the energy landscape on how high the energy barrier is in the dimerization reaction scheme. Finally,

it would also be beneficial if we could conduct applying fluid-mosaic model to quantitatively analyze the structural properties of the membrane (15-19). It will open the doors to discover the reason for slow kinetics of WT CLC-ec1 in the order of several weeks which were previously observed (3, 11).

7.5 Functional Consequences of CLC-ec1 Dimerization

A recurring question in the study of CLC-ec1 dimerization is why CLCs have evolved to be dimer complexes despite the monomer being the minimal functional unit (20). While the earlier parts of this thesis research focus on the thermodynamic and kinetic analysis of CLC-ec1 as a model system, these advancements provide key methodologies that can be used to investigate this challenging question. With this, we hypothesized that the dimerization presents a mechanism for regulating the functional behavior of each subunit as dimerization is not required for function, and a prediction that different functional conditions will be linked to different dimerization behaviors. Our findings in Chapter 6, presented in **Figure 6-2, 6-3** report that dimerization is strongly impacted by pH but not by different functional states. To understand it further, it would be more beneficial if we move onto investigating if the channelized version of CLC (EAYS) also exhibit pH regulatory behavior by alternating pH from 4.5 to 7.5 using bulk FRET and single molecule photobleaching technique. These type of analysis on the kinetic and the thermodynamic stability of EAYS at different pHs will support the fundamentals of fast-gating behavior in the EAYS construct. We also found that the dimerization is strongly linked to pH environment, but we have not clarified the fundamental reasons why they are strongly related. Therefore, the research would also benefit from investigating the connection between N-terminal and pHs by truncating the N-terminal domain and conduct the dimerization study with the construct to investigate the relationship between pH and the N-terminal domain in CLC-ec1.

Lastly, other membrane protein complexes such as LeuT-fold transporters are known to have independent transport pathway in each subunit which the role of oligomerization is not apparent (21). Therefore, it would be interesting to investigate the relationship between oligomerization reactions and functional mechanisms of them using single molecule capture method (3, 11) and the bulk FRET assays introduced throughout the chapter. This will be useful information to characterize the reasons for oligomerization of membrane proteins within different membrane protein complexes.

7.6 Future Directions for the Study of Membrane Protein Assembly Thermodynamics and Kinetics in Membranes

We are still in an early stage to conclude that all CLCs exhibit strong dimer stability, or that all constructs behave in a similar way. While our studies demonstrate that CLC-ec1 is both thermodynamically and kinetically stable, it may be that other CLCs represent the extremes of this reaction, such as being irreversible dimers, like CLC-ec1 at pH 7.5, or even natively monomeric, like CLC-ec1 I201W/I422W. To investigate this further, evolutionary relationships of CLCs would be useful, as well as an analysis of the structures of the dimerization interfaces and residues that line these surfaces. While it is expected that a similar backbone fold will confer the same physical mechanisms of dimerization stability by the large change in heat capacity introduced by solvation defects, it can be that the sequence variation at this surface can modulate the overall stability or kinetics. In addition, the observation that eukaryotic CLCs have evolved cytosolic dimerization domains indirectly implies that the membrane embedded subunits may be more dynamic or less stable in the dimer form, thus presenting a need to evolve additional domains to keep the subunits together. Thus, study of the stability of eukaryotic CLC dimerization would be an interesting path of investigation that may be possible following this research. Beyond CLC, thermodynamics and

kinetics studies can also be carried out in other membrane proteins such as Fluc, KcsA by applying the single molecule subunit capture and bulk FRET methods (11) that we have introduced throughout the thesis to investigate the oligomerization which have not been discovered.

References

1. A. Accardi, C. Miller, Secondary active transport mediated by a prokaryotic homologue of CLC Cl⁻ channels. *Nature* **427**, 803-807 (2004).
2. T. J. Jentsch, Discovery of CLC transport proteins: cloning, structure, function and pathophysiology. *J Physiol* **593**, 4091-4109 (2015).
3. R. Chadda *et al.*, The dimerization equilibrium of a CLC Cl⁽⁻⁾/H⁽⁺⁾ antiporter in lipid bilayers. *Elife* **5** (2016).
4. T. J. Jentsch, CLC chloride channels and transporters: from genes to protein structure, pathology and physiology. *Crit Rev Biochem Mol Biol* **43**, 3-36 (2008).
5. J. M. Sturtevant, Heat capacity and entropy changes in processes involving proteins. *Proc Natl Acad Sci U S A* **74**, 2236-2240 (1977).
6. W. Kauzmann, Some factors in the interpretation of protein denaturation. *Adv Protein Chem* **14**, 1-63 (1959).
7. K. A. Dill, S. Bromberg, *Molecular driving forces : statistical thermodynamics in chemistry, physics, biology, and nanoscience* (Garland Science, New York, ed. 2nd, 2010).
8. Y. Yano, K. Matsuzaki, Measurement of thermodynamic parameters for hydrophobic mismatch 1: self-association of a transmembrane helix. *Biochemistry* **45**, 3370-3378 (2006).
9. Y. Yano, A. Yamamoto, M. Ogura, K. Matsuzaki, Thermodynamics of insertion and self-association of a transmembrane helix: a lipophobic interaction by phosphatidylethanolamine. *Biochemistry* **50**, 6806-6814 (2011).
10. R. Chadda *et al.*, Membrane transporter dimerization driven by differential lipid solvation energetics of dissociated and associated states. *Elife* **10** (2021).
11. R. Chadda *et al.*, A thermodynamic analysis of CLC transporter dimerization in lipid bilayers. *Proc Natl Acad Sci U S A* **120**, e2305100120 (2023).
12. C. L. Pan, Measuring Dissociation Rate Constants of Protein Complexes through Subunit Exchange: Experimental Design and Theoretical Modeling. *Plos One* **6** (2011).
13. D. Goulet, Modeling, Simulating, and Parameter Fitting of Biochemical Kinetic Experiments. *Siam Rev* **58**, 331-353 (2016).
14. R. E. Jefferson, T. M. Blois, J. U. Bowie, Membrane proteins can have high kinetic stability. *J Am Chem Soc* **135**, 15183-15190 (2013).

15. S. J. Singer, G. L. Nicolson, The fluid mosaic model of the structure of cell membranes. *Science* **175**, 720-731 (1972).
16. G. L. Nicolson, Update of the 1972 Singer-Nicolson Fluid-Mosaic Model of Membrane Structure. *Discoveries (Craiova)* **1**, e3 (2013).
17. G. L. Nicolson, The Fluid-Mosaic Model of Membrane Structure: still relevant to understanding the structure, function and dynamics of biological membranes after more than 40 years. *Biochim Biophys Acta* **1838**, 1451-1466 (2014).
18. G. L. Nicolson, G. Ferreira de Mattos, A Brief Introduction to Some Aspects of the Fluid-Mosaic Model of Cell Membrane Structure and Its Importance in Membrane Lipid Replacement. *Membranes (Basel)* **11** (2021).
19. G. L. Nicolson, G. Ferreira de Mattos, Fifty Years of the Fluid-Mosaic Model of Biomembrane Structure and Organization and Its Importance in Biomedicine with Particular Emphasis on Membrane Lipid Replacement. *Biomedicines* **10** (2022).
20. J. L. Robertson, L. Kolmakova-Partensky, C. Miller, Design, function and structure of a monomeric ClC transporter. *Nature* **468**, 844-847 (2010).
21. K. N. Kazmier (2013) Revealing the Mechanistic Diversity of the LeuT Fold: A Comparative Analysis of the Leucine Transporter and the Hydantoin Transporter using Electron Paramagnetic Resonance Spectroscopy.